Development of a Constitutive Model to Simulate Unbonded Flexible Riser Pipe Elements

A thesis submitted for the degree of Doctor of Philosophy

By

Ali Bahtui

Department of Mechanical Engineering
Brunel University

December 2008

Supervisor: Doctor Hamid Bahai
Co-supervisor: Doctor Giulio Alfano

Abstract

The principal objective of this investigation is to develop a constitutive model to simulate the hysteresis behaviour of unbonded flexible risers. A new constitutive model for flexible risers is proposed and a procedure for the identification of the related input parameters is developed using a multi-scale approach. The constitutive model is formulated in the framework of an Euler-Bernoulli beam model, with the addition of suitable pressure terms to the generalised stresses to account for the internal and external pressures, and therefore can be efficiently used for large-scale analyses. The developed non-linear relationship between generalised stresses and strains in the beam is based on the analogy between frictional slipping between different layers of a flexible riser and frictional slipping between micro-planes of a continuum medium in non-associative elasto-plasticity. Hence, a linear elastic relationship is used for the initial response in which no-slip occurs; an onset-slip function is introduced to define the 'no-slip' domain, i.e. the set of generalised stresses for which no slip occurs; a non-associative rule with linear kinematic hardening is used to model the full-slip phase. The results of several numerical simulations for a riser of small-length, obtained with a very detailed (small-scale) non-linear finite-element model, are used to identify the parameters of the constitutive law, bridging in this way the small scale of the detailed finite-element simulations with the large scale of the beam model. The effectiveness of the proposed method is validated by the satisfactory agreement between the results of various detailed finite-element simulations for a short riser, subject to internal and external uniform pressures and cyclic bending and tensile loadings, with those given by the proposed constitutive law. The merit of the present constitutive law lies in the capturing of many important aspects of risers structural response, including the energy dissipation due to frictional slip between layers and the hysteretic response. This privilege allows one to accurately study the cyclic behavior of unbonded flexible risers subject to axial tension, bending moment, internal and external pressures.

Acknowledgements

To my parents, Aghdas and Mohammad, with love...

Keywords

Unbonded flexible riser; Finite-element simulations; Cyclic loading; Stick-slip interaction; Constitutive modelling; Non-associative plasticity; Frictional slipping; Parameter identification;

List of all publications resulted from this work

Journals papers:

1. Bahtui A., Bahai H., Alfano G. (2008). 'A finite element analysis for unbonded flexible risers under torsion', *Journal of Offshore Mechanics and Arctic Engineering (OMAE)* **130**(4): 041301 (4 pages).

2. Bahtui A., Bahai H., Alfano G. (2008). 'Numerical and analytical modelling of unbonded flexible risers', *Journal of Offshore Mechanics and Arctic Engineering (OMAE)*, *In Press*.

3. Alfano G., Bahtui A., Bahai H. (2008). 'Numerical derivation of constitutive models for unbonded flexible risers', Submitted to *International Journal of Mechanical Sciences, Under review*.

4. Bahtui A., Alfano G., Bahai H., Hosseini-Kordkheili S.A. (2008). 'A multi-scale computational model for unbonded flexible risers', Under development, to be submitted to *Computers & Structures, An International Journal*.

5. Bahtui A., Bahai H., Alfano G. (2008). 'A finite element analysis for unbonded flexible risers under axial tension', Submitted to *Journal of Offshore Mechanics and Arctic Engineering (OMAE), Under review*.

Conferences:

1. Bahtui A., Bahai H., Alfano G. (2007). 'Numerical and analytical simulation of unbonded flexible risers subjected to combined modes of loading', *9th US National Congress on Computational Mechanics, Minisymposium: 095 - Session 1: Computational Methods for Large Structures and Materials*, San Francisco, CA July 23-26.

2. Bahtui A., Bahai H., Alfano G. (2008). 'A finite element analysis for unbonded flexible risers under axial tension', *Proceedings of OMAE2008 27th International Conference on Offshore Mechanics and Arctic Engineering*, Estoril, Portugal, June 15-20.

3. Bahtui A., Bahai H., Alfano G. (2008). 'Constitutive modelling of unbonded flexible risers under tension', *8th World Congress on Computational Mechanics (WCCM8 - ECCOMAS 2008)*, Venice, Italy, June 30 – July 5.

Bahtui A., Alfano G., Bahai H. (2009). 'A Multi-scale approach to the analysis of ultra deepwater unbonded flexible risers', Submitted to *Proceedings of OMAE2009 28th International Conference on Offshore Mechanics and Arctic Engineering*, Honolulu, Hawaii, June 2009.

Table of Contents

List of Figures

and Kebadze, 2001)

Chapter 6

List of Tables

1 Introduction

1.1 General introduction

The continuous development of unbonded flexible risers is a core factor supporting the evolution of the subsea oil industry to face the challenges associated with the increasing demand for deep-water applications. Developments in the capabilities of finite element analysis technology have been influential to the success of these new projects.

The location of vast parts of the oil and gas fields in deep waters presents clear challenges for the design and installation of extra-long risers. A number of design standards for extra-long risers fall beyond the scope of the current design codes, so specialised engineering assessments should be applied.

Deepwater and ultra deepwater riser fatigue failure due to vortex induced vibration (VIV) is currently considered by the oil industry to be a very significant unresolved problem. When the vortex shedding frequency coincides with a natural frequency of the riser the resulting response can have catastrophic repercussions. Risers are subjected to severe current in most deepwater development areas, resulting in accumulation of significant VIV short cycle fatigue induced damage. Both drilling and production risers, usually designed for long service lives, are affected by VIV. The main techniques used to model this behaviour are predominantly based on analytical or numerical models which utilise empirical force coefficient data taken from simplified cases and are therefore possess a significant degree of uncertainty in general application. VIV is essentially a coupled fluid-solid interaction phenomenon and as such should be treated and simulated as fully coupled. This, however, in view of the highly non-linear behaviour of a flexible riser and the very large size of the full 3-dimensional CFD required presents an enormous computational challenge which cannot be performed on any current computational platforms in a practical length of time.

1.2 Flexible riser

Marine risers are classified into two categories: drilling and production risers. A drilling riser is used for exploratory drilling and is made of steel which contains the drill string and drilling mud. A production riser consists of a cluster of flow-lines, which transfer the crude oil from seabed to sea-surface. Traditional production marine risers are vertical rigid steel structures, which are prevented from buckling by application of a tensile force to its top end. This makes these structures suitable for shallow water applications. Flexible risers, as modern production risers, withstand much greater vessel motions than rigid steel risers and do not require external tensile force at their extremes (O'Brien and McNamara, 1988).

Flexible riser was introduced to the marine market in the early 70's and was installed in the Enchova field offshore Brazil in 1978 (Machado and Dumay, 1980). Two generic types exist for flexible risers: unbonded flexible riser, without adhesive agents between the layers, and bonded flexible riser with the reinforcing bonded to an elastomeric matrix (Out *et al.*, 1995). The term 'flexible riser' refers to the capacity of a pipe to combine low bending stiffness with high axial tensile stiffness. However, unbonded flexible risers offer a better option which features both of these characteristics. Withstanding significant flexure together with maintaining the required axial strength and pressure integrity makes unbonded flexible risers a unique structure suitable for ultra deepwater applications (Kraincanic and Kebadze, 2001).

A flexible riser is comprised of several distinct layers. This modular assembly allows each layer to be made fit-for-purpose and independently adjusted to best meet a specific field development requirement. In these types of pipes although the layers are independent, they are designed to interact with one another. The pipe cross-section of a flexible riser is a combined construction of spirally wound steel layers and thermoplastic materials. The main components are leak-proof thermoplastic barriers and corrosion-resistant steel layers such as carcass and pressure armour layers. The helically wound steel wires at the helical armour layer give a high-pressure resistance and excellent bending characteristics to the whole system of assembly, which results in the flexibility and a superior dynamic behaviour.

The space between the internal sheath layer and the most outer layer is known as the annulus. The layers occupy approximately 90 percent of the annulus and the remaining 10 percent is gaps between layers, which facilitate lateral movements of the layers as the riser bends. Geometric non-linearity originated from the helical configuration of the tendons within a helical layer together with the material nonlinearity originated from the polymeric layers, non-linearity introduced by layer interaction and the changing contact conditions under load, makes the unbonded flexible riser to reveal highly non-linear mechanical properties with coupling effects between axial, torsional and flexural deformations (Witz 1996). Further details on the function and design of the layers are in Recommended Practice for flexible pipe (API RP 17B, 2002; API Spec 17J, 2002).

1.3 Problem statement

The growing economic importance of structural integrity of risers for deep waters and ultra deep waters for the oil and gas industry demands enhanced simulation techniques. A methodology is required to significantly reduce the computational time associated with running of the finite element detailed models of riser structure. Such a capability should have significant benefits for cost effective deep water flexible riser design practise.

1.4 Research objectives

The aim of the present project is to develop a constitutive model for unbonded flexible risers. The results from a detailed verified finite element model or experiment of the cross-section of unbonded flexible risers can then be replaced by this constitutive model, taking into account all the geometric nonlinearity, detailed frictional effects and hysteresis effects. This type of hysteretic constitutive model will be suitable for implementation into finite element codes to analyze the highly non-linear behaviour of long unbonded flexible riser structures.

1.5 Main contributions of the work

The present project aims to develop a constitutive model to describe a very detailed behaviour of the unbonded flexible risers including highly non-linear geometric feature of the flexible riser as well as the inter-layer contact and stick-slip effects. The constitutive model can then be implemented into a global nonlinear beam element finite element code to analyse the nonlinear coupled fluid-solid interaction response. This multi-scale approach significantly reduces the computational time usually associated with full finite element runs.

1.6 Layout of the thesis

The first chapter is an introduction and the identification of the research problem. It also gives a brief description of the objectives of the research. The second chapter contains a literature review in which previous studies and research on the flexible riser have been reviewed. An explanation of the problem and importance of the research as well as the motivation and the novel aspects of the research have also been presented in this chapter. In the third chapter, a finite element analysis of the behaviour of multi-layer unbonded flexible risers, subjected to various types of loading, is developed. The fourth chapter outlines an analytical solution of a riser subjected to several loading cases. This chapter clearly explains the fundamental principles involved in the problem.

In chapter five, the numerical model is verified and validated by the analytical model and limited published experimental results. Chapter six discusses the approach followed to develop a general constitutive model in which the constitutive law for the 3D beam model is formulated, the key issue of the identification of the parameters of the beam constitutive model is addressed, and numerical results are presented and discussed to validate the effectiveness of the proposed method. Conclusions and future work are discussed in Chapter seven, where other aspects to be investigated in future work are addressed, followed by a list of references, appendices, and publications by author.

2 Literature Survey and Motivation

2.1 Introduction

Preventing failure in deeper water risers is a new industrial challenge. As exploration for oil and gas move into deeper waters, rig maintenance and repair become more difficult and expensive. Therefore, a high degree of structural integrity has to be attained at the design stage.

The need for design tools and processes to improve riser installation and operation success rates becomes more acute as water depth increases. Rigorous analysis and testing of riser designs are crucial to ensure in-service performance failure prevention. The analysis and testing should simulate as closely as possible the real-life conditions under which the riser will function.

At the sea-surface, a riser structure is subjected to a high mean tension combined with cyclic loading, and at the seabed, it is subjected to severe external pressure, axial compression, bending and torsion. In the installation procedure however, the pipe is empty, and it experiences high combined axial compression and bending at the touchdown point (TDP) (Brack *et al.*, 2005).

A flexible riser comprises of several different layers. Starting from the most inner layer, these include a carcass, an internal pressure sheath made of polymeric material, an interlocked pressure armour layer, an anti-wear layer, two tensile armour layers and an outer sheath with each layer having a particular function (Kagoura *et al.*, 2003). All layers are free to slide with respect to each other. Figure 2.1 illustrates the various layers of a typical unbonded flexible riser. The external plastic sheath layer protects the riser from surrounding seawater intrusion, external damages during handling and corrosion. The internal plastic sheath layer ensures internal fluid integrity and is made from polymer.
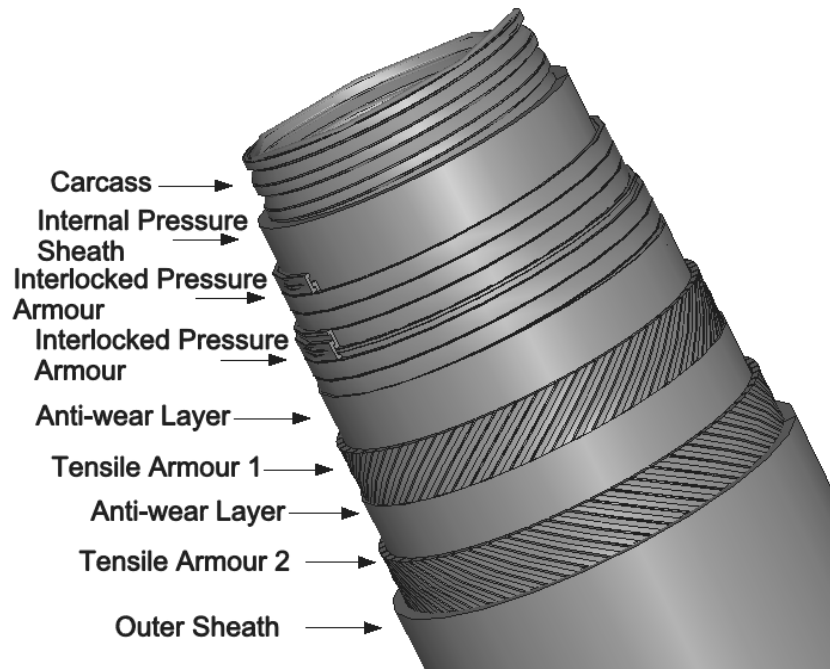
Figure 2.1: Layer structure of a typical unbonded flexible riser

Anti-frictional layers are non-metallic thermoplastic sheaths or tape wrappings, used between structural layers to decrease abrasion and wear (Kraincanic and Kebadze 2001). Wearing of these layers around the neutral axis can occur in bending fatigue analysis of unbonded flexible pipes (Tuohy *et al.*, 1999). This layer can be replaced by a solid lubricating layer which is sufficiently thick to prevent all the wear in the structure layers (Out *et al.*, 1995). The carcass layer is a metallic structure which mainly resists radial inward forces, providing partial resistance to collapse of the layers when the riser is subjected to various types of external loading. This layer is made up of an interlocked profiled strip in an almost circumferential lay (Witz, 1996).

The 'zeta'-shaped helical or interlocked pressure armour layers have reinforcement effects against internal and external pressure and support hoop loading. This layer provides support outside the fluid barrier layer by resisting ovalisation of the underlying structure such as carcass layer (Zhang *et al.*, 2003). The 'zeta'-shaped layer is not capable of withstanding either axial or bending loads significantly. This is because it is wound in a helix with a short pitch with a lay angle close to 90 degrees and with a gap between turns, of an interlocked metal profile wires (Leroy and Estrier, 2001). This layer can be complemented by a backup pressure layer which is a metallic layer, wound

at short pitch and provides additional resistance to the radial force in very high pressure risers (Feret and Bournazel, 1987).

Tensile armour layers are a pair of contra-wound wraps of even number of wires laid with a long pitch. These layers mostly withstand axial load, torsional and bending moments. They are not usually self-equilibrating structures. In the case of external tension, an internal torque is induced which tends to unwind the layer. Therefore variations in the axial direction lead to variation in the circumferential direction, transmitting a torque to the support (Lanteigne, 1985). Flexibility in bending of unbonded risers originates from the ability of the tendons of helical layers to slip with respect to each other. This leads to wear and ultimately to the fatigue of the tendons. The amount of slip is inversely proportional to the lay angle of the tendons (Out and Morgen, 1997).

The advantages of flexible risers with respect to rigid steel risers is the much lower bending stiffness of the former, leading to smaller radiuses of curvature with the same pressure capacity, due to the complex make up of flexible risers (API RP 17B, 2002; API Spec 17J, 2002), in turn resulting in increased ability of undergoing large deformations under loads induced by the sea current, vortex induced-vibrations, the motion of the floating-vessel and during installation.

One of the problems associated with the complex design of unbonded flexible risers is the difficulty in its analysis. To capture the many important aspects of their structural response, including the energy dissipation due to frictional slip between layers, the hysteretic response and the fatigue damage, efficient and accurate tools are required.

Current methods are generally divided into two categories: analytical formulations and finite-element models. The analytical models share many of the following simplifying assumptions, which significantly limit the range of applicability of the results: displacements and strains are small (Feret and Bournazel, 1987; Claydon *et al.*, 1992; Harte and McNamara, 1993); some coupling terms in total stiffness matrix are neglected (Harte and McNamara, 1993); the conventional elastic thin-walled theory can be assumed valid (McNamara and Harte, 1989; Claydon *et al.*, 1992); tendons are restricted from rotating about their local helical axis (Claydon *et al.*, 1992); strains

and/or stresses across the layer thickness are constant (Claydon *et al.*, 1992); thicknesses of layers remain constant during deformation (Claydon *et al.*, 1992); plane sections remain plane (Harte and McNamara, 1993); ovalisation effects are neglected (Harte and McNamara, 1993; Kraincanic and Kebadze, 2001); contact and/or frictional effects are ignored (Witz and Tan, 1992a&b; Harte and McNamara, 1993; McIver, 1995; Brack *et al.*, 2005; Tan *et al.*, 2005); no slip occurs between layers (Zhang *et al.*, 2003); tendons are constrained to slide only along their own axis (Kraincanic and Kebadze, 2001); tendons respond only axially, (bending and torsional stiffness neglected) (Claydon *et al.*, 1992; Harte and McNamara, 1993; Kraincanic and Kebadze, 2001); the interlayer contact pressure is constant (Feret and Bournazel, 1987; Kraincanic and Kebadze, 2001); the contribution of the plastic sheaths to the strength and stiffness of the riser can be neglected (Feret and Bournazel, 1987; McIver, 1995); layers remain constantly in contact (no bird-caging effect) (Feret and Bournazel, 1987; McNamara and Harte, 1989; Claydon *et al.*, 1992); the radial deformation is the same for all layers (Claydon *et al.*, 1992; Kraincanic and Kebadze, 2001; Bahtui *et al.*, 2008b); initial manufacturing residual stresses can be ignored (Brack *et al.*, 2005). Therefore all available analytical methods are restricted because of the complexity of modelling layers.

The downside of finite-element type of analysis is the high computational cost so that, to make the analysis feasible, the riser model length is restricted to only few meters or few layers in the best case scenario and even for such limited models intensive computational capabilities and solution time are required. This is the main reason that all numerical methods are restricted to very simple modelling cases.

There are two approaches to model a flexible riser: classical approach and multi-layer approach. In the classical approach an equivalent beam model is used to represent all layers by summing up the contributions of all the layers in the cross-sectional and material properties of the beam. The advantage of this approach, referred to as "Composite" riser modelling scheme, is in its computational efficiency. This method, in which the riser is modelled as one homogeneous structure is currently being used as an industry-standard dynamic analysis method in some of the software tools.

The main problem in these conventional modelling and analysis approaches is that it is not possible to capture the actual detailed three-dimensional behaviour of the unbonded flexible riser. Such behaviour is largely due to their nonlinear response which is caused by the existence of interaction between numerous helically-wound layers and contact between various layers.

The multi-layer modelling scheme approach was therefore provoked by the inadequacy of composite model results. An important application of the multi-layer approach is that it offers the possibility of conducting riser bending-curvature analysis. This is because the inner layer does not have the same bending-curvature characteristics as the outer layer, and only the multi-layer modelling approach, which incorporates the effect of the inter-layer contact, can simulate this influence.

The multi-layer modelling scheme also makes it feasible to calculate the amount of pressure preload required for the inner layer. Over preloading causes the internal layer to come into contact with the outer part at the most bent regions. On the other hand, not enough preload causes the inner layer compression leading to full cycle fatigue (Roger, 2000).

The amount of friction between layers of a typical unbonded flexible pipe depends on the interaction between its individual component layers. This analysis is only possible in the multi-layer modelling scheme. When the shear forces between layers are smaller than the frictional forces, the riser behaves as a solid rod and its response is linear. The response of these structures can be nonlinear when the shear forces overcome the interlayer frictional forces and sliding occurs between the layers (Kebadze and Kraincanic, 1999).

In the multi-layer modelling approach, although the loads (tension, shear and moment) in each layer are fully captured and the interaction between layers is considered, the disadvantages include the considerable modelling effort involved and the computational inefficiency. A main motivation for this work is to seek a novel approach to study the behaviour of unbonded flexible risers in more detail and with more efficiency.

2.2 Composite riser modelling scheme

Modelling the response of flexible risers is much more challenging than that of steel rigid risers. Flexible risers are subjected to severe currents and waves in most deepwater applications. The risers can undergo large displacements. The flexible riser problem is therefore essentially a fully three dimensional problem, and as such should be simulated as a three dimensional model. In view of its non-linear behaviour, this makes the task of modelling and analysis of the riser a very significant and computationally challenging effort. Due to the significant complexity of the problem, methods presented before the 90's were mostly based on the assumption of treating the riser as a homogenous material.

Among the first works on the composite riser modelling scheme was that of Knapp (1979). He derived an element stiffness matrix for cable elements subjected to tension and torsion by replacing the cross-section of a cable with a single composite element. His approach was quite general and included consideration of the geometric non-linearities, compressibility of the core, arbitrary cross section of the core, variation of lay angles and the number of wire layers. However, treating the cross-section of a cable as a single composite element potentially ignores any interaction between layers and neglects contact and hysteresis effects in his analysis. Similar assumptions have been made in the following papers reviewed in this section, all of which ignore the effects of friction between layers as a result of which the any energy dissipation due to contact between layers of unbonded flexible risers is captured.

A static analysis procedure for the numerical determination of nonlinear static equilibrium configurations of deep-ocean risers was performed by Felippa and Chung (1980). The riser was modelled by three-dimensional beam finite elements which included axial, bending, and torsional deformations. They extended their model by taking the deformations coupled through geometrically nonlinear effects (Felippa and Chung, 1981a). The resulting tangent-stiffness matrix included three contributions identified as linear, geometric (initial-stress) and initial-displacement stiffness matrices. For the solution, a combination of load-parameter incrementation, state updating of fluid properties and corrective Newton-Raphson iteration was used. The detailed

computerised analysis of their work is found in Felippa and Chung (1981b) in which they discussed the importance of drag force along the pipe, varying significantly along the depth. The authors are of the opinion that the sensitivity of the results to environment characterization necessitates a review of many modelling and analysis practices.

McNamara and Lane (1984) studied the two-dimensional response of the linear and nonlinear static and dynamic motions of offshore systems such as risers and single-leg mooring towers. Their proposed method was based on the finite element approach using convected coordinates for arbitrary large rotations and includes terms due to loads such as buoyancy, gravity, random waves, currents, ship motions and Morison's equation. The same authors extended their work to the three-dimensional frequency domain computational dynamic analysis of deep-water multi-line flexible risers (McNamara and Lane, 1992).

O'Brien *et al.* (1988) presented a three-dimensional finite element modelling of marine risers, pipelines and offshore loading towers based on the separation of the rigid body motions and deformations of elements under conditions of finite rotations. This paper includes all nonlinear effects including geometry changes, bending-axial and bending-torsional coupling and follower forces and pressures. The authors developed their model by dividing the riser into a series of catenaries where the buoyancy modules were described as inverted catenaries (O'Brien and McNamara, 1988). They obtained economical and accurate solution based on a single-step implicit time integration operator with a variable increment size. Both works assumed an equivalent single layer representing all layers of the riser.

A two-dimensional static and dynamic analysis of flexible risers and pipelines in the offshore environment subjected to wave loading and vessel movements was presented by McNamara *et al.* (1998). They developed a hybrid beam element formulation where the axial force was combined with the corresponding axial displacements via a Lagrangian constraint. The hybrid beam element was capable of applying to offshore components varying from mooring lines or cables to pipelines with finite bending stiffnesses. However, they failed to consider contact and frictional effects between layer components of the riser.

Hoffman *et al.* (1991) reviewed the design technique of deep and shallow water marine bonded riser systems as well as their dynamic analytical and numerical analysis and the non-linearities arising from hydrodynamic loading and dynamic boundary conditions. This paper contains design methodology criteria, parameters and procedures of flexible riser systems. They categorised the designing of this structure into three stages: Determining an acceptable system layout, assessing the global dynamic response, and performing detailed static and dynamic analysis of local areas.

Ong and Pellegrino (2003) studied the nonlinear dynamic behaviour of mooring cables in the frequency domain. They ignored the effects of friction and impact between the cable and the seabed. Their proposed method models the time-varying boundary condition at the touchdown by replacing the section of cable interacting with the seabed with a system of coupled linear springs. They decomposed the seabed interaction into axial stretching of laid riser and the catenary action at the touchdown using a linear stress-strain relationship. Catenary action is the liftoff-and-touchdown behaviour of the pipe lying on the seabed.

Zhang *et al.* (2003) discussed analytical tools for improving the performance of unbonded flexible pipe. This work uses an equivalent linear bending stiffness which is derived from experimental data to calculate the maximum bending angle range. It contains reports on irregular wave fatigue analysis, collapse, axial compression and bird-caging for riser systems. The authors are of the opinion that the combined bending, axial compression and torsion could lead to the tendon being separate from the cylinder in a helix layer, and may lead to out of plane buckling. However the assumption of equivalent linear bending stiffness neglects all the interactions between layer components of an unbonded flexible riser and makes it to behave as a bonded riser.

Willden and Graham (2005) reported results from two strip theory CFD investigations of the Vortex-Induced Vibrations of model riser pipes of which the first one is concerned with the vibrations of a vertical riser pipe that was subjected to a stepped current profile, and the second one is concerned with the simultaneous in-plane and out-of-plane vibrations of a model steel catenary riser that was subjected to a uniform current profile. Their method was based on computing the fluid flow in multiple two-

dimensional planes that are positioned at intervals along the length of a body. It was found that six to seven simulation planes are required per half-wavelength of pipe vibration in order to obtain convergence. This work is based on modelling of bonded risers and ignores the effects of friction between layers and does not capture any energy dissipation due to contact between layers.

2.3 Multi-layer modelling scheme

Unbonded flexible risers are being increasingly used in the oil industry. However, their behaviour, particularly in deep water applications, is not yet well understood. This is largely due to their complex structure which makes their response extremely difficult to analyze. Prediction of the cyclic behaviour of a flexible riser is of particular importance to ensure their structural integrity during service (Out *et al.* 1995). The interest of the engineers in this subject has been renewed recently due to the increased use of flexible risers in deep water applications. Practical reports indicated the applicability of larger diameter (greater than 10") flexible risers in waters as deep as 1000 m (Serta and Brack, 1990).

In the past three decades several simplified analytical riser models, mainly of helical armour layer type, have been developed. Electrical engineers were first in analysing helix layers. McConnel and Zemke (1982) presented a simplified mathematical model to predict the coupled axial - torsion properties of ACSR electrical conductors. The general conclusion from their work is that the axial-torsional behaviour is highly coupled and axial motion causes torsional motion and vice versa. They validated their analytical results by experimental data and demonstrated reasonable agreement.

Lanteigne (1985) took into consideration the effect of the coupling parameters, tension-bending, and torsion-bending by analyzing the response of helically armoured cables subjected to tension, torsion and bending. This work contains the derivation of the stiffness matrix of a straight cable for small and large curvatures as well as the investigation of the influence of internal radial forces and curvature on the effective flexural rigidity. It has been stipulated that in the absence of external compression on

the conductors, the flexural rigidity decreases as the curvature increases. Furthermore, when the conductor is perturbed by one or many strand failures, the coupling parameters, tension bending and torsion bending which are generally zero, must be taken into account. Finally, sliding of the first two internal layers of the conductor could not occur upon bending, because the radial compressive force component induced was such that tensile forces developing could not overcome the resulting frictional forces.

Out and Morgen (1997) presented the slippage of helical armour layers on a bent unbonded flexible riser. They studied the amount of slip and the change of the curvature of the individual tendons. During the investigation of the slippage they discovered that the amount of slip is expected to be an upper bound for the slip of the helical armour layers of an unbonded flexible pipe in practice. The general conclusion was that in a fatigue analysis, both changes of the normal and bi-normal curvatures should be considered.

One of the recent works on helix layers is that of Tan *et al.* (2005) in which their higher order geometrical effects has been investigated taking into consideration the effect of the tendon cross-section characteristics. In this paper a rather accurate analytical strain energy model has been developed, although frictional effects were ignored. This work also discusses a brief structural coupling between bending and axial-torsional behaviour of the pipe. Comparing their analytical and numerical results shows that numerical results are conservative in nature allowing for confidence in use of finite element model for practical designs. This conservative nature of the numerical model originates from the stronger constraint condition adopted by the model, authors claimed.

The forgoing works involved analysing a single helix layer without the need to consider frictional contact behaviour. Accurate simulation of the various constituent layers of the flexible riser is very important as a typical flexible riser is made up of a number of discrete layers each of a different type and with a particular function. Among the first papers on the detailed mechanical behaviour of unbonded flexible risers were those of Oliveira *et al.* (1985), Feret *et al.* (1986), Feret and Bournazel (1987) and Out (1989). These works contain the first proposed methods for evaluating the service life and fatigue design of unbonded flexible risers. These methods are based on a cumulative damage rule that accounts for the hysteretic nature of bending only. The frictional

contact analysis in these works is restricted to helical armour layers at most and is very limited.

Later, Claydon *et al.* (1992) studied the prediction of the dynamic service life of an unbonded flexible riser under cyclic loading conditions. They took the interlayer contact pressures into account and also considered stress recovery, slip between layers and riser interlayer wear and fatigue. Their work contains individual analysis for each layer, summation of these individual layer stiffnesses as the total bending stiffness and presents a theoretical basis for each stage of service life prediction. However, frictional contact analysis in this work is based on several assumptions and only for helix layers and for bending moments loading only.

Witz and Tan presented two consecutive reports on the behaviour of marine flexible pipes of which the first one concentrated on the axial-torsional structural behaviour (Witz and Tan, 1992a) and the second one covers the flexural structural behaviour of these structures (Witz and Tan, 1992b). The first general conclusion of their first work is that an inappropriate choice of tendon lay-angle in helix layers can lead to bird-caging at relatively small deformations and has a significant influence on the axial –torsional load-displacement relationship. "Bird-caging" is a failure mode in which the tensile armour tendons buckle radially and layer separation occurs. This usually happens in case of compressive axial loading and also can occur if the torsion is applied in the opposite direction of the most external tensile armour layer. Secondly, the boundary conditions at the terminations have a noticeable effect on the tensile stiffness. Their incorrect report in this work is possibly to conclude that the axial-torsional load-displacement relationships are highly linear. Witz and Tan (1992b) extended their work to the rotary bending test of marine cables and umbilicals. They assumed an arbitrary curvature distribution along the length of the marine cable in their analytical model. They reported a hysteretic bending moment-curvature relationship for generic flexible structures. By taking into account the terminal boundary conditions and a finite sample length, they found that the frictional restrictions which keep armours constraint non-uniformly can be overcome, allowing the tendons to slide axially only. Furthermore, bending of rectangular tendons in the normal and bi-normal directions is prevented by geometrical shape and can not be overcome unless the structure is destroyed. They reported the failure of the armour wires at the middle of the specimen, where maximum

bending curvature exists. The authors are of the opinion that surface defects have a significant effect on the fatigue life of these components. Both works studied frictionless interaction between layers through calculating interlayer pressures which fails to capture energy dissipation due to friction.

Harte and McNamara (1993) developed an analytical model composed of individual isotropic and orthotropic layers each of which has a unique stiffness. The total stiffness matrix for the whole model has been calculated by the summation of all stiffnesses. Their work, however, did not include the contact and friction between layers. By assuming a unique radial displacement for all layers, they implied that the riser is bonded and strains are in the linear domain.

Witz (1996) discussed a case study analysis of flexible risers, comparing results from the works carried out at ten different institutions which included stress analysis of marine cables in rotary bending test (Witz and Tan, 1995). It was shown that if layer interaction is considered, current methods agree with the experimental data for the axial-torsional structural response. However this conclusion excludes the flexural structural response. He supported the argument that internal pressure does not significantly affect the full slip bending stiffness. It was concluded that in the case of axisymmetric loading, suitable methods exist for predicting the structural response of a flexible pipe including interaction effects between the component layers. Furthermore, models which do not consider this interaction may give erroneous results for some axisymmetric load cases. He suggested that more research is needed in this area to establish the structural behaviour of flexible pipe under coupling loading.

Kebadze and Kraincanic (1999) studied the nonlinear bending behaviour of offshore flexible pipes. The effect of terminations was neglected and the Coulomb friction model was used for frictional behaviour. The static and dynamic frictional coefficients were taken to be equal. It has been stipulated that since sliding of helical strips is accompanied by fretting and wear, it may be necessary to predict not only the cumulative value of the interlayer slip, but also how slip progresses as a function of applied loads on the flexible pipe. They assumed that armour layers can slide only along their own axis. This work neglects the bending and torsional stiffness of individual helical strips which implies that tendons carry only axial loadings. This assumption is

based on the previous work of same second author (Raoof and Kraincanic, 1994). Nevertheless, they only considered the bending stiffness corresponding to bending radius greater than the contact radius. Flexural analysis is restricted to determining the upper and lower bounds of the bending stiffness and the critical curvature at which the change from the upper (no-slip) limit to the lower (full slip) limit takes place. Critical curvature is when slip initiates on the neutral axis of a bent pipe, or rather when the interlayer friction overcomes. Authors reported the initiation of interlayer slippage in tendons at the neutral axis of the pipe cross-section. Furthermore, even for the maximum curvature applied on a pipe, parts of tendons at the extreme fibre positions do not slide. It was found that maximum stress in tendons is proportional to the magnitude of bending curvature and does not depend on the level of interlayer friction. On the other hand, the bending stiffness of a pipe is proportional to the bending curvature, level of interlayer friction (Kebadze and Kraincanic, 1999) and interlayer contact pressures (Kraincanic and Kebadze, 2001). They concluded that a curvature variation from zero to a given value doubles the slip compared to a constant curvature of the given value. Furthermore, the flexible pipe response to axisymmetric loads is nearly linear and can be modelled reliably.

The same authors discussed the slip initiation and progression in helical armouring layers of unbonded flexible pipes and its effect on pipe bending behaviour (Kraincanic and Kebadze, 2001). In this work, in addition to the previous mentioned assumptions, they also assumed the followings: interlayer contact pressure is constant everywhere in the interface; bending occurs far from terminations; friction between the armouring tendons within a helical armour layer is not considered because of gaps between the tendons. They derived the minimum and maximum critical bending curvature as a function of the interlayer friction coefficient and the interlayer contact pressure using a Coulomb friction model. Their approach is attractive in decomposing the curvature domain by assuming a gradual transition and progression of stiffness between the 'no-slip' and the 'full-slip' stiffness. This assumption prevents the bending stiffness of dropping drastically to zero when the bending curvature reaches the minimum critical bending curvature which is an improvement on their previous work. However, their simplified method considers the slippage between component layers in the bending analysis only and it is not capable of analysing the coupling between bending, tension and torsion. They mentioned that helical layers need to be supported by surrounding

cylindrical layers to have significant structural strength and integrity. Meanwhile, the non-linearity of the response associated with the sliding of individual helical elements between the surrounding layers was considered. Therefore, the influence of the surrounding layers in terms of interlayer friction is inevitable. The first general conclusion is that the neutral axis has the largest forces trying to slide the tendons. Therefore, if the tendon is only restrained by the friction, the interlayer slippage initiates at the neutral axis. Should the helical layer be fixed mechanically at the neutral axis, like terminations, the stress concentration leads to break at those points. Secondly, in the maximum curvature situations in the regions far from terminations, tendons do not slide at the extreme fibre positions. Thirdly, interlayer pressures always exist in actual pipes because of manufacturing process. Therefore they suggested that the initial manufacturing interlayer pressures are important and should be given alongside the pipe construction data. Furthermore, the bending stiffness of flexible pipe is highly dependent on the magnitude of the interlayer friction coefficient. Fourthly, the flexible pipe stiffness is more sensitive to the external pressure than to the internal one. This work preceded that of Kebadze (2000) in which an analytical model of an unbonded flexible riser had been proposed.

All analytical models proposed so far have some sort of limitation on their scope of applicability due to the simplifying assumptions on which they have been based. Neglecting frictional effects is among the hypotheses commonly made. The interlayer frictional effects are the underlying cause of highly nonlinear behaviour of unbonded flexible risers and this has indeed been one of the main motivations of considerable research efforts into the development of finite element models for risers.

Numerical solutions have also been difficult to achieve due to the very significant computational requirements associated with solving such large models. Contact algorithms, in particular, introduce a high degree of nonlinearity into the finite element problem which in turn increases the solution time drastically. The helical armour layers are particularly difficult to mesh due to their special shape and, as a result, this usually leads to having to include a coarse mesh with elements whose scaled-Jacobians exceed acceptable limits (Knupp, 2000).

Brack *et al.* (2005) reviewed the works from researchers on the flexible riser resistance against combined axial compression, bending, and torsion in ultra-deep water depths. They reported that in order to prevent bird-caging phenomenon, high resistance tapes should be helically applied over the most external tensile armour layer. Meanwhile, special care should be taken to prevent the extra increase of the pipe axial stiffness. Furthermore, an adequate design of tensile armour layer and a correct assessment of required resistance of the tapes is necessary when the real axial compression is associated with cyclic bending. This is due to the tendon buckling which may occur on the cylindrical surface where the tendons have been applied on (even without any significant radial deformation). Their study shows that the majority of the models which predict bending response of the flexible pipe structures intended to simulate only the riser top region, which is under high tension loads. Therefore, there are not many papers which deal with the behaviour of the riser bottom region, where bending combined with compression tend to occur. They evaluated the influence of the tendon restriction to axial rotation and concluded that the tendon restriction to axial rotation is function of the tendon width, torsion inertia and of the contact pressure from the high resistance tapes. A helix layer with high lay angle exposes high radial deformation when subjected to axial compression forces, for the same weight per unit length, Brack *et al.* reported. For higher angles, structure resistance to tension is lower. As a result, a thicker high resistance tape layer is required to prevent bird-caging. This work shows that most of current finite element models, including this work, neglect the effects of physical non-linearity, residual stresses due to pipe manufacturing and friction between layers.

2.4 Requirement of a constitutive model

The development in the use of unbonded flexible risers for floating production systems has advanced dramatically over the past decade. Significant insights have been obtained into the stress analysis of riser cross-sections by analytical modelling of each individual layer taking into account the slippage of only helix layers under bending moments. These researches, despite suffering from fundamental simplifications and ignoring of important inter-layer frictional effects in all stages of analysis, have produced new analytical and numerical models in the form of packages for the prediction of riser behaviour.

Hibbitt *et al.* (1979) presented highly nonlinear analysis of marine pipelines, involving both geometric nonlinearity (due of the large rotations) and frictional effects caused by the pipeline lying directly on the seabed. The motions, caused by moving the already laid down pipelines into a correct position, typically involve very large translations and rotations. The authors are of the opinion that the usual stiffness formulation is not practicable due to the slender characteristics of the pipelines. Their method is based on numerical models for the components of the system (pipeline, friction, drag chains, towing cable) which lead to the efficient solution of typical problems. Due to the strong path dependency of the system, a nonlinear incremental scheme has been used.

Nielsen *et al.* (1990) presented the capability to predict the service life of dynamic flexible risers which was conducted by three organizations. This paper contains a review of static and dynamic analyses of the riser, each stage performed by one organization. It is a practical application of the hysteresis model proposed by Witz and Tan (1989) to analysis fatigue. The model is based on a slip onset criterion for bending loading only. The work of Nielsen *et al.* further estimates the service life of dynamic flexible risers based on results obtained from Flexriser 4 program, which is a package originally developed for the Chevron Spain Montanozo project.

Relative slippage between helix and other layers leads to the modelling of the stiffness of unbonded flexible risers by a bi-linear curve, Bech *et al.* reported (1992). They used this model to analysis the structural damping of this structure. Damping measures were obtained for tension, torsion and bending deformations. It has been stipulated that the obtained equivalent damping ratio is high in bending (10 to 30%) and can significantly influence the dynamic response.

Saevik (1993) utilised the kinematic restraints present when the tendons of a helix layer slides only in the curvilinear plane of the supporting pipe to develop an eight degree of freedom curved beam element. His approach used the Green stain tensor to obtain strain and stress measures in the nonlinear finite element formulation based on an updated Lagrange formulation for arbitrarily large displacements and rotations but with small strains. The interaction between pipe and tendons was handled by a combination of

hyperelastic (bonded pipes where the tendon is surrounded by an elastomer) and elastoplastic (unbonded pipes to simulate friction) springs in the nodal points.

McIver in 1995 studied the mathematical basis of a model used to model the detailed behaviour of the individual components of bonded and unbonded flexible pipe sections including frictional effects. However the analysis was based on non-slip full-slip assumption. Four commonly used wire sections were modelled while considering layer separation effects. A post contact analysis was performed neglecting contact of wires within a layer. Tension, torque, shear forces, bending moments, wall pressure and temperature differentials were considered in the analysis. The formulation is limited to linear behaviour between bending moment and curvature. Temperature was assumed to be uniform within each layer. McIver developed effective (average) material properties for the compound section, which leads to neglecting the actual riser structural effects. Nevertheless, this work neglects initial stress condition, its geometrical stiffening effect, the effect of end terminations, layer contact in bending, initial interlayer gaps and hysteresis effects. It is concluded in this paper that strong coupling exists amongst most degrees-of-freedom and that due to the powerful effect exerted by layer separation under loading, stresses built in during manufacture should be considered in any flexible pipe model. The author is of the opinion that flexible riser behaves differently if installed from point A to point B rather than from point B to point A (McIver, 1995).

In 1995 Out *et al.* studied the integrity of flexible pipe. In their study, they searched for an inspection strategy by using a certain technique to look at the structure and assessing its suitability. This work discusses the type of defects and degradation in all phases of the pipe's life. The design of flexible riser systems for mechanical deterioration is not fully proven and the governing failure modes are quantitatively uncertain. It has been stipulated that acoustic emission is suitable for the inspection of flexible pipe for wear damage. For the inspection of flexible pipe for fractured outer tensile armours radiography, magnetic strayflux and eddy current are the best methods. Finally, eddy current and acoustic emission were considered suitable for the inspection of flexible pipes for fatigue cracking of the pressure reinforcing (Out *et al.*, 1995).

A comprehensive overview of status of analysis techniques for flexible riser design as well as a historical overview of the development of hydrodynamic analysis techniques were reported in 1995 by Patel and Seyed. This work discusses the models which are being exploited in the optimization of pipe construction and highlights key issues addressed during these developments including the effects of internal and external hydrostatic pressures. This work concludes by highlighting the potential gaps in this filed of study which is the effects of structural damping, tangential hydrodynamic drag loads, and seabed interaction effects, the effects of vortex shedding and out of plane oscillations of mid-water buoys. It also expresses concern about the lack of sufficiently wide ranging and openly available model testing and full-scale data on flexible risers (Patel and Seyed, 1995).

Atadan *et al.* studied dynamic three-dimensional response of risers in the presence of ocean waves and ocean currents undergoing large deflections and rotations. They included shear effects based on nonlinear elastic theory in their formulation. It is concluded that the length of the riser is the most important parameter which affects the deflections of the marine-riser (Atadan *et al.*, 1997).

Yazdchi and Crisfield used a simple two-dimensional lower-order beam element formulation for static nonlinear analysis of riser structures including the effects of buoyancy, steady-state current loading and riser top-tension. They assumed linearly elastic material property for the riser by employing a constant modulus of elasticity. They studied the static behaviour of flexible pipelines and marine risers, using the types of finite elements that had been developed for conventional non-linear analysis (Yazdchi and Crisfield, 2002a). Same authors continued their research by using a beam finite element formulation based on Reissner–Simo beam theory for the static and dynamic non-linear analysis of three-dimensional flexible pipes and riser systems in present of hydrostatic and hydrodynamic forces. Employing a linearly elastic material property, their work concentrates on the non-linearities due to the fluid loading and the associated large deformations and considers hydrodynamic forces due to effects such as wave, drag and current action (Yazdchi and Crisfield, 2002b).

Recent developments on the fatigue analysis of unbonded flexible risers reveal the necessity of a comprehensive global dynamic analysis together with the detailed

hysteresis damping of the riser loading response and the three-dimensional local stress analysis. Smith *et al.* (2007) presented an application based on a fatigue reassessment of a riser system and claimed that the advanced fatigue methods produce longer fatigue lives than the current state-of-practice methods, despite the fact that their method was based on an elastoplastic model of riser bending response.

Lacarbonara and Pacitti presented a geometrically exact formulation for dynamic analysis of cables with linearly elastic material behaviours subjected to axial stretching and flexural curvature. The formulation was based on nonlinearly viscoelastic constitutive laws for the tension and bending moment with an additional constitutive nonlinearity accounting for the no-compression condition (Lacarbonara and Pacitti, 2008).

Some works in the literature however consider a bi-linear bending stiffness. These works take into account the energy dissipation originated from frictional contact between layers in bending moment analysis (Bech *et al.*, 1992; Smith *et al.*, 2007). However the bi-linear bending stiffness proposed by these papers does not depend on internal and external pressures. This generates significantly inaccurate results when studying the response of a long riser floating in ultra-deep water depth. Moreover the study has been performed only on the hysteresis effects in bending analysis whereby hysteresis effects for axial strain or any coupling with radial displacement are ignored. On the other hand the bi-linear model in these works is based on two different stiffnesses, one when stick and one when slip occur between layers. This type of models are restricted and are not capable of taking into account kinematic hardening, stabilization, variable stick or slip stiffness dependency due to pressure difference.

Hysteresis is intrinsically linked to the frictional resistance of unbonded flexible riser after its compounding layers become in contact by tensile load, torque, bending moment, pressure or any combination of these loadings. Hysteresis damping effect occurs as energy is lost after every loading cycle. Friction originates structural damping in global dynamic motion and local stress analysis of the riser and makes its response hysteresis which is less widely understood and is often neglected for simplicity of producing a conservative analysis.

As a result, new packages predicating the service life of unbonded flexible riser demands comprehensive detailed cross-sectional models which take into consideration of the fine nonlinear hysteresis behaviour of geometric and material effects; a constitutive model which accurately simulate the fine detailed hysteresis stiffness of an unbonded flexible riser. This can be performed by a robust and active constitutive model which include variables such as internal and external pressures, and which is capable of being implemented into existing finite element packages and perform efficient fatigue or VIV computational calculations

2.5 Motivation and the novel research approach

From the above discussion and the previous studies, it is important to note that the detailed behaviour of unbonded flexible riser has to date not been accurately analysed and a new approach to modelling their behaviour could help to mitigate their failure in ultra-deep waters. This approach should go beyond the 'Composite' riser and multi-layer modelling scheme to encompass three-dimensional extra-long lengths and to account for detailed cross-sectional contacts. It improves confidence levels and helps avoiding over engineering of dynamic unbonded flexible risers.

Sophisticated numerical tools such as ABAQUS software are capable of modelling complex geometries and component interaction within a very short length riser. These types of software demand computational power that can make them impractical for modelling an entire length of dynamic riser and are not practical for day-to-day engineering analysis and design.

The quest for larger models while maintaining greater accuracy has stimulated the activity to develop a novel constitutive model for unbonded flexible risers. This model aims at combining the accuracy of a detailed finite element model of a short part of riser, with the low computational cost of a three-dimensional Euler-Bernoulli beam element, in the framework of a novel, multi-scale approach capable of addressing large scale problems.

3 Numerical Modelling of Unbonded Flexible Risers

3.1 Introduction

The work outlined in this chapter presents a very detailed finite element model of an unbonded flexible riser. The finite element method is a powerful numerical technique for the simulation and analysis of a variety of problems encountered in engineering. The use of finite element method to support research and product development and the availability of faster and cheaper hardware has created the opportunity to solve larger and more detailed models. There are generally two different numerical schemes which can be adopted in the finite element procedure: implicit and explicit time integration algorithms.

Implicit algorithm requires iterative solutions for each time increment (time step). Explicit algorithm, avoiding iterations and convergence problems, is generally used for highly nonlinear problems with many degrees of freedom, for which iterations are very expensive and convergence problems are frequent. For stability reasons, explicit methods use smaller time steps than implicit ones.

The explicit dynamics procedure can be an effective tool for solving an unbonded flexible short-length riser model, because the cost per increment of an implicit method is far greater than that of an explicit method. In this methodology, the turnaround time is largely determined by the number of elements and the smallest element dimension. This method requires a small time increment size that depends solely on the highest natural frequencies of the model and is independent of the type and duration of loading.

The most striking feature of the explicit method is the lack of a global tangent stiffness matrix, which is required with implicit methods. Since the state of the model is advanced explicitly, iterations and tolerances are not required.

3.2 Finite element packages

There are many finite element software packages, both free and proprietary. To make the analysis more secure, the Abaqus FEA software is used to conduct the analyses. The Abaqus solver has been enhanced to include expanded feature coverage, reduced memory usage and improved performance. The improved performance is particularly noticeable in large models with over a million degrees of freedom. Abaqus has reduced simulation times, and improved the efficiency and accuracy of pipeline design.

The unbonded flexible riser problem is well-suited to Abaqus/Explicit. The Abaqus/Explicit can readily analyze problems involving complex contact interaction between many independent bodies. It is also very efficient in solving highly nonlinear classes of problems that are essentially static. Quasi-static process simulation problems involving complex contact generally fall within this class.

Another finite element package which can be used potentially to analyze complex problems involving interaction, such as risers, is LS-DYNA. This software is basically a general-purpose, nonlinear finite element analysis software used to analyze the nonlinear dynamic response of three-dimensional inelastic structures. Its fully automated contact analysis capability and error-checking features have enabled users worldwide to solve successfully many complex crash and forming problems. Livermore Software Technology Corporation (LSTC) develops sophisticated tools for modelling and simulating the large deformation behaviour of structures. These tools include LS-DYNA for analysis, LS-POST for post-processing which are interfaced with leading CAD, FEA, and FEM systems.

3.3 Geometry of the riser

Flexible risers consist of different layers (Figure 3.1), each one designed for a specific task. Main components are the helical armour layers and a set of sealing and/or anti-
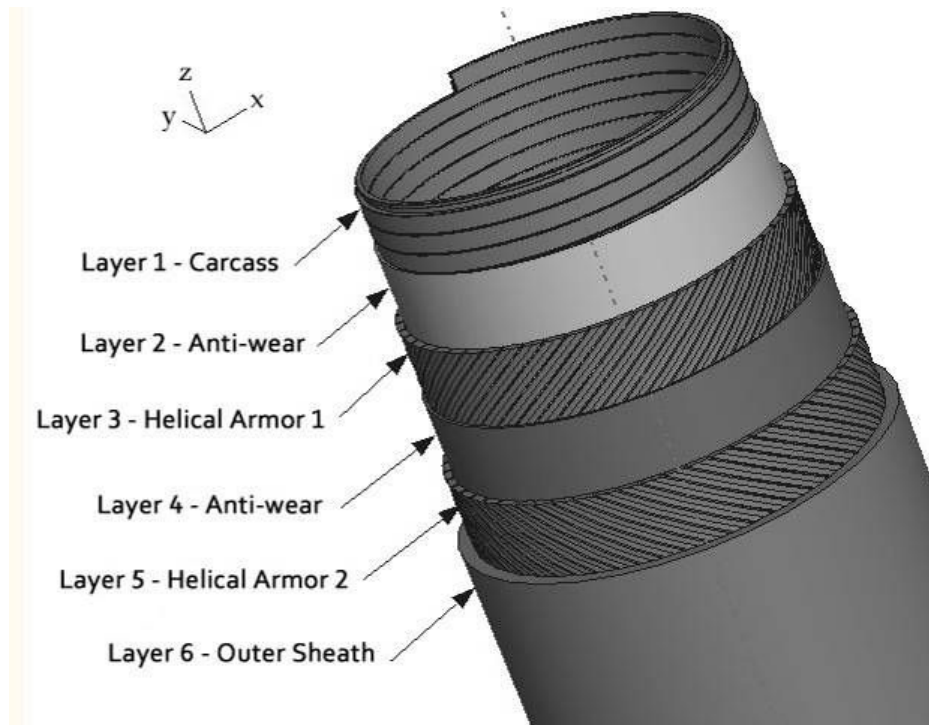
Figure 3.1: Schematic of a typical six-layer unbonded flexible riser.

wear polymer layers, while additional components which are typically present include a metallic internal 'carcass' and a pressure armour layer (API, 2002). The geometry of an

Table 3.1: Flexible pipe geometrical data.

Layer	Type	r_i (mm)	r_o (mm)	r (mm)	t (mm)	α (degrees)
1	Carcass	85.54	90.54	88.04	5	88.44
2	Anti-wear Layer	90.76	97.46	94.11	6.7	90
3	Helical Armour 1	99.43	103.42	101.43	3.99	36.54
4	Anti-wear Layer	103.55	104.95	104.25	1.4	90
5	Helical Armour 2	105.17	109.17	107.17	4	-35.59
6	Outer Sheath	109.4	116.3	112.85	6.9	90

Definitions:

Type   - Layer description

r_i/ r_o - Radius to layer inner/ outer surface

r   - Layer mean radius

t   - Layer thickness

actual flexible pipe was chosen from manufacturer as shown in Table 3.1. More detailed views of helical armours and carcass layer are in Figures 3.2 and 3.3, respectively.

Section X-X

α - Tendon angle relative to pipe axis
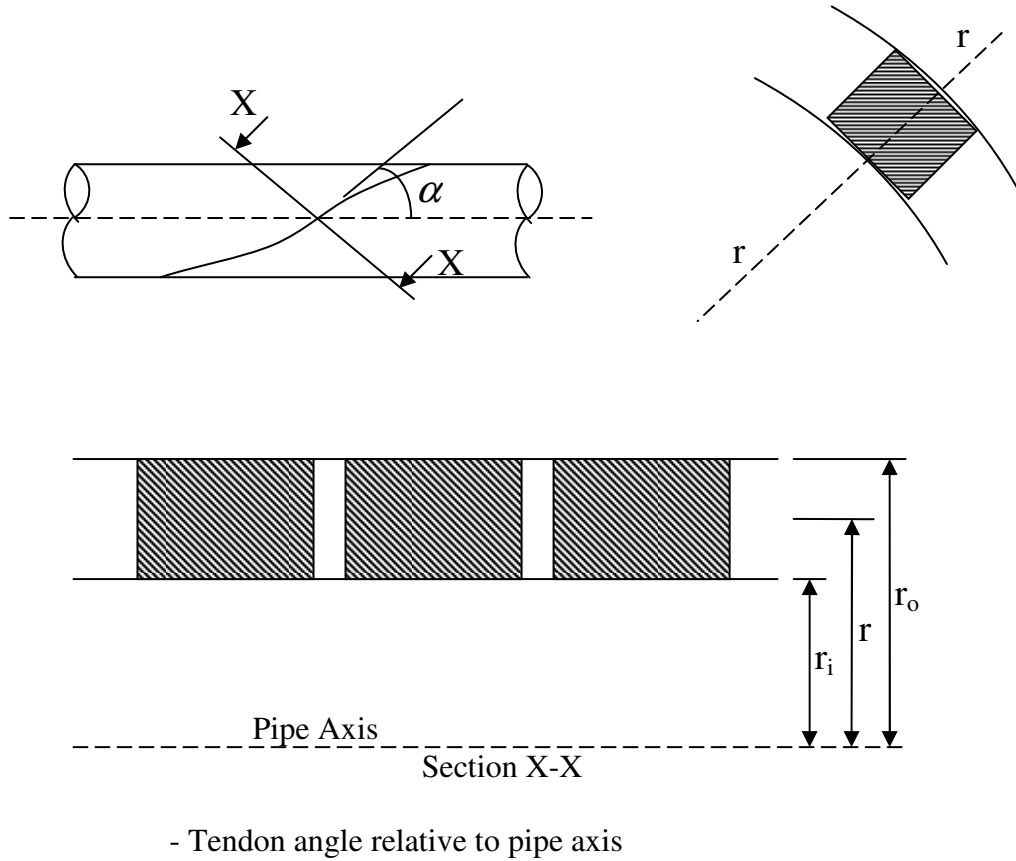
Figure 3.2: Detailed geometry of riser.

Figure 3.3: Carcass layer profile.

3.4 Element formulation

The elements used in the model are of 8-noded linear brick type (Figure 3.4) with reduced integration and hourglass control for the sheath, anti-wear and the helical armour layers and 4-node doubly curved thin shell type with reduced integration and hourglass control for the carcass layer. The integration along the shell thickness is accomplished using the Simpson's integration technique. The number of section points through the thickness of the shell is three, integrated during all iterations of the analysis.
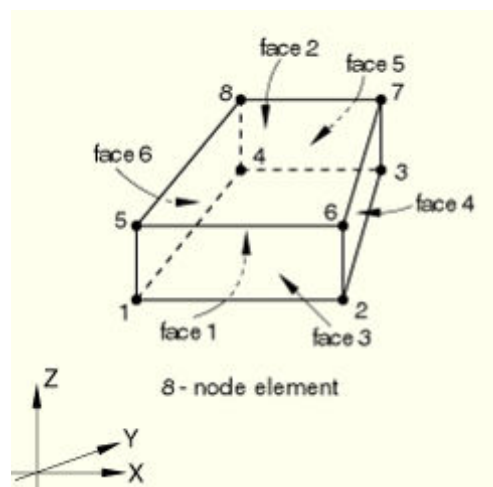
Figure 3.4: An 8-noded linear brick type element.

3.5 Material properties

All layers except the carcass layer were assumed to have isotropic type of properties. The material data for the riser analysis is listed in Table 3.2. Modelling a three-dimensional carcass layer in very detail leads to excessive computational solution time. The carcass layer is thus replaced by an equivalent material and geometric orthotropic layer.

The material property of the equivalent orthotropic layer was derived by comparing results from the actual carcass layer and results from the embedded orthotropic sheath

Table 3.2: Material data for the riser.

Layer	Type	E (N/mm^2)	ν	σ_y (N/mm^2)	ρ (kg/m^3)
1	Carcass	$E_1 = 1.50E+5$ $E_2 = 1.24E+4$	0.3	250	7860
2	Anti-wear Layer	3.50E+2	0.4	21	1030
3	Helical Armour 1	2.10E+5	0.3	740	7860
4	Anti-wear Layer	3.50E+2	0.4	21	1030
5	Helical Armour 2	2.10E+5	0.3	740	7860
6	Outer Sheath	3.50E+2	0.4	21	1030

layer. The orthotropic material properties are then evaluated using Equation (3.1) for structural stability (Lempriere, 1968).

$$E_1, E_2, E_3, G_{12}, G_{13}, G_{23} \succ 0,$$

$$|v_{12}| \prec \left(\frac{E_1}{E_2}\right)^{\frac{1}{2}}, \qquad |v_{21}| \prec \left(\frac{E_2}{E_1}\right)^{\frac{1}{2}},$$

$$|v_{13}| \prec \left(\frac{E_1}{E_3}\right)^{\frac{1}{2}}, \qquad |v_{31}| \prec \left(\frac{E_3}{E_1}\right)^{\frac{1}{2}}, \tag{3.1}$$

$$|v_{23}| \prec \left(\frac{E_2}{E_3}\right)^{\frac{1}{2}}, \qquad |v_{32}| \prec \left(\frac{E_3}{E_2}\right)^{\frac{1}{2}},$$

$$1 - v_{12}v_{21} - v_{23}v_{32} - v_{13}v_{31} - 2v_{21}v_{32}v_{31} \succ 0.$$

To rewrite the last term in the above equation, the relation between the major Poisson's ratio and the minor Poisson's ratio

$$\frac{v_{ij}}{E_i} = \frac{v_{ji}}{E_j} \tag{3.2}$$

have to be substitute, which results in

$$1 - v_{12}^2 \frac{E_2}{E_1} - v_{13}^2 \frac{E_3}{E_1} - v_{23}^2 \frac{E_3}{E_2} - 2v_{12}v_{13}v_{23} \frac{E_3^2}{E_1^2} \succ 0. \tag{3.3}$$

3.6 Modelling and mesh

A detailed three-dimensional finite element model is developed under a global cylindrical coordinate system with its origin located at the centre of riser bottom end. Layers were modelled individually and then assembled together. The two helical armour layers are wounded in opposite directions and have different radii, resulting in a non axi-symmetric geometry and therefore a full three dimensional model had to be developed in order to capture all the fine details of the behaviour of this structure. The tendons of the helical armour layers have been modelled separately as 3D beams, each having a rectangular cross-section, revolved around the riser axis in the circumferential direction with a constant pitch. Figure 3.5 shows the initial un-deformed finite element mesh for the entire model of the six-layer riser. Different meshing schemes were used for various layers.

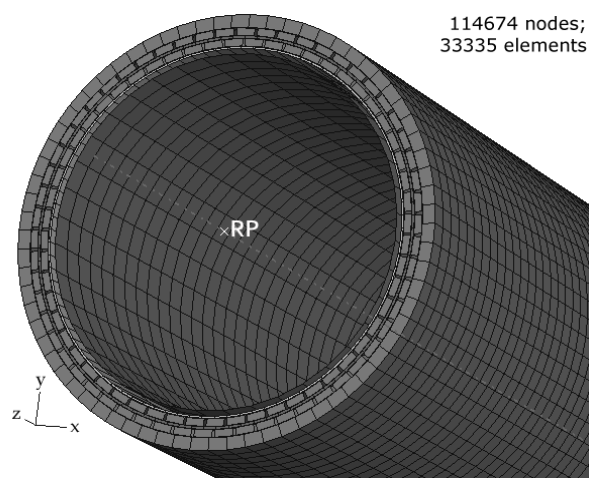Figure 3.5: Meshed version of six-layer unbonded flexible riser.

Using few elements in the circumferential direction for different layers may lead to initial layer penetration between layers in the radial direction. "ABAQUS/Explicit determines which slave nodes in the predicted configuration penetrate the master surfaces. The depth of each slave node's penetration, the mass associated with it, and the

time increment are used to calculate the resisting force required to oppose penetration. ABAQUS/Explicit uses these distributed forces and masses to calculate an acceleration correction for the master surface nodes." (Abaqus, 2007). This makes those detected nodes to move very significantly in one increment which renders the analysis to become completely unstable during the first initial increments.

Therefore a minimum number of elements is chosen in the circumferential direction which also prevent initial layer penetration between layers in the radial direction. This avoids initial radial acceleration as a result of the layer penetration detection by contact algorithm between layers. Meanwhile, mesh convergence was fully studied by comparing results for different number of elements for the whole riser.

3.7 Interaction between layers

Three-dimensional contact interaction is introduced between all layers, so that the layers are allowed to slide with respect to each other during all stages of loading. The contact interaction is also allowed for between each tendon of a helical armour layer. Contact is simulated, using a penalty contact method based on Coulomb friction model together with the general contact algorithm of Abaqus/Explicit (Abaqus, 2007). Abaqus contact algorithm uses sophisticated tracking procedures to ensure that proper contact conditions are enforced efficiently and also is well compatible with three-dimensional surfaces. The general contact algorithm generates contact forces to resist node-into-surface and edge-into-edge contact penetrations. The primary mechanism for enforcing contact is node-to-surface contact. The general contact algorithm also considers edge-to-edge contact, which is very effective in enforcing contact that cannot be detected as penetrations of nodes into faces. The coefficient of friction between polymer sheath layers, steel helical armour layers and carcass layer is taken as 0.1, as given in experimental results (Saevik and Berge, 1995).

3.8 Dynamic quasi-static analysis

A static analysis is required to study the behaviour of a riser and obtain its load-displacement curves. Since a global set of equations must be solved in each increment, the cost per increment of a static implicit method is far greater than that of an explicit method. The explicit dynamics procedure is ideally suited for the analysis of quasi-static processes. The advantage of the explicit method is that it allows the solution to proceed without iterations and without requiring tangent stiffness matrices to be formed. It also simplifies the treatment of complicated contact conditions. One advantage of the explicit procedure over the implicit procedure is the greater ease with which it resolves complicated contact problems. In addition, as model is very large, the explicit procedure requires less system resources than the implicit procedure (Abaqus, 2007). The explicit method is computationally efficient because it uses only 400MB memory to run rather than the implicit method which requires more than 40GB of memory for a six-layer riser model, which is currently not feasible on most platforms.

Due to the complexity of the detailed three-dimensional model and the large number of contact surfaces, an explicit quasi-static type of analysis is a natural choice to simulate the flexible riser problem. For the simulation to be quasi-static, the loading rates must be such that the kinetic energy remains small compared to the internal energy throughout the analysis. Each load is applied with a low enough loading rate to allow the structure to settle into a steady state, avoiding any significant vibration. This has been verified by comparing the results of various analyses done with different loading rates. Therefore the time-history in the explicit analysis does not influence the result. The time increment used depends on modulus of elasticity, density, and element size. For this analysis the time increment was set to a value of $\Delta t = 5 \times 10^{-7}$ seconds. This implied a computationally intensive solution procedure, so that a parallel cluster composed of 16 processors was used.

3.9 Load cases and boundary conditions

Loads - The load cases considered are tension, torsion, and bending. These will be referred to as cases 1, 2 and 3, respectively. All the load cases include an initial pressure load step which accounts for the internal fluid pressure and the external hydrostatic pressure, as outlined in Table 3.3. In the tension and torsion load cases the riser is initially subjected to an internal pressure loading of 3MPa but no external pressure load is applied. The bending load case, however, includes a 14MPa internal pressure and a 12MPa external pressure. Internal pressure is applied on the inner surface of the innermost layer after the carcass, and the external pressure is applied on the outer surface of the outermost layer.

Table 3.3: Load Cases – Types.

Load Case	Load type applied to riser
1	Initial pressure + Tension along Z direction
2	Initial pressure + Torsion around Z direction
3	Initial pressure + Bending around X direction

All three load cases include three steps: an initial pressure loading (installation phase), an external loading, and an unloading step. All loads are applied as a linear function of time in each step. The tension load is represented by an axial load of 500kN and the torsion load is a 30kNm torque applied to the riser. In the bending load case, a 8kNm couple is applied. These are outlined in Table 3.4.

Table 3.4: Load Cases – Steps and Values.

Load Case	Loads applied to riser		
	Loading	Linear Loading	Linear Unloading
1	Int. Pressure = 3MPa;	Axial Force = 500kN	Axial Force = 500kN
2	Int. Pressure = 3MPa;	Torque = 30kNm	Torque = 30kNm
3	Int. Pressure = 14MPa; Ext. Pressure = 12MPa;	Bending Moment = 8kNm	Bending Moment = 8kNm

Loading points and boundary conditions in finite element analysis – All the nodes at each of the two cross sections at both ends of the riser are rigidly connected to two reference points which are positioned at the centre of the sections. All boundary conditions for both ends are applied to these two reference points only. All loads (such as tension, torsion, and bending) are applied to the references point at the top end of the riser only. Figure 3.5 shows the top reference point as RP.

The reference point connected to the bottom end of the riser is completely constrained in all translational and rotational directions during the analysis. The reference point which is connected to the top end of the riser model is completely free during the pressure loading step, and for the other loading steps has the following constraints:

- torsional loading and unloading: free in all degrees of freedom
- axial & bending loading and unloading: fixed in the rotational direction about the longitudinal axis of the riser

3.10 Simulation

The analysis is carried out as a geometrically non-linear problem. This non-linearity occurs due to the presence of contact surfaces as well as large rigid body displacement taking place in the tendons of the helical armour layer. Elements are therefore distorted from their original shapes as the deformation increases. Elements, used in the mesh, are chosen to be well compatible with large-displacement effects.

Hourglassing is monitored carefully by keeping the ratio of hourglass energy to internal energy well below 5%. All elements are of acceptable shape with respect to aspect ratio, scaled-Jacobian, and warpage measures. Although the finite element analysis takes into account the effects of large deformations and rotations, these nonlinear effects should be ignored when the validating the results against the analytical formulation explained in Chapter 4. Therefore, the magnitude of all the loads applied in various cases is kept relatively low to ensure that the resulting strains are kept within elastic limits. This makes finite element results to be comparable with analytical ones. This

constraint was imposed on the solution because the analytical results are based on elasticity theory.

3.11 Solution

Using the numerical models described above, a 1.7 meter long flexible riser made up of the carcass layer, three polymer sheath layers and two steel helical armour layers of equal and opposite lay angles is considered. This length equals approximately twice the length of one pitch in the helical armour layer, as suggested by the manufacturer. The proposed 1.7m length of the riser is long enough to eliminate the effect of boundary conditions at both ends on the results at middle length section. All layers exist in full length. Connection between layers is through both ends as well as contact between their internal and external 3D surfaces.

4 Analytical Modelling of Unbonded Flexible Risers

4.1 Introduction

The work outlined in this chapter presents an analytical approach to the analysis of the unbonded flexible riser. In this approach, each layer of the riser is analysed separately and its stiffness influence is added to the overall riser behaviour. The main contribution of this chapter is a switch algorithm which is incorporated to prevent layer separation. As discussed further, this algorithm switches Equation (4.35) by Equation (4.41) when layer separation occurs.

Figure 4.1 shows the axial displacement u_z, together with the axial rotation ϕ, the rotations about the normal and bi-normal directions ψ_x and ψ_y, and the radial displacement u_r.

It is assumed that the layers are allowed to move in radial direction independently. This implies that layer separation and bird-caging effect (Bahtui *et al.*, 2008d) are allowed. The hypothesis of small displacements and strains is made.
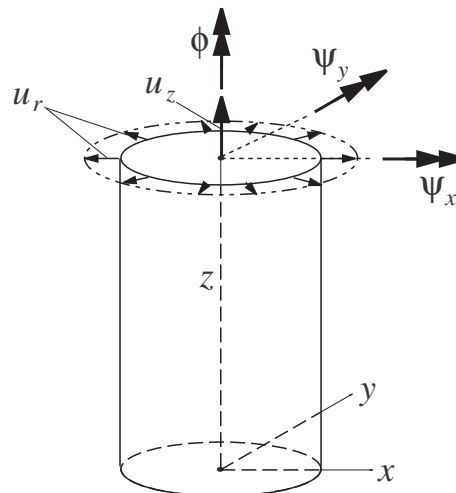

Figure 4.1: Sign conventions of a layer.

4.2 Definitions

Next two sections are dedicated to two fundamental definitions which will be used further in the analytical solution.

4.2.1 Internal energy

Energy is defined as the capacity to do work. In solid deformable elastic bodies under loads, the work done by external loads is stored as recoverable internal energy. The internal energy stored in the body under deformation in 1-2-3 orthogonal coordinate system is then defined as (Garg *et al.*, 1973)

$$U = \frac{1}{2}\int_V (\sigma_1\varepsilon_1 + \sigma_2\varepsilon_2 + \sigma_3\varepsilon_3 + \tau_{23}\gamma_{23} + \tau_{31}\gamma_{31} + \tau_{12}\gamma_{12})dV \;. \tag{4.1}$$

Using appropriate Hooke's Law, this equation can be written containing stress components only and the result is called the complementary energy U^σ. Rewriting this equation in terms of strain components, the result is called the strain energy U^ε. These two energies, for a linear Hookean material, are equal

$$U^\sigma = U^\varepsilon \;. \tag{4.2}$$

With plane-stress assumption, σ_3, τ_{23}, and τ_{13} are set to zero in equation (4.1). Looking at this equation, we find

$$U = \frac{1}{2}\int_V (\sigma_1\varepsilon_1 + \sigma_2\varepsilon_2 + \tau_{12}\gamma_{12})dV \;. \tag{4.3}$$

4.2.2 Hooke's law for isotropic and orthotropic materials

The most general strain-stress relationship for a three-dimensional body in 1-2-3 orthogonal coordinate system in terms of compliances is given as follows

$$
\begin{Bmatrix} \varepsilon_1 \\ \varepsilon_2 \\ \varepsilon_3 \\ \gamma_{23} \\ \gamma_{13} \\ \gamma_{12} \end{Bmatrix} = \begin{bmatrix} S_{11} & S_{12} & S_{13} & 0 & 0 & 0 \\ S_{12} & S_{22} & S_{23} & 0 & 0 & 0 \\ S_{13} & S_{23} & S_{33} & 0 & 0 & 0 \\ 0 & 0 & 0 & S_{44} & 0 & 0 \\ 0 & 0 & 0 & 0 & S_{55} & 0 \\ 0 & 0 & 0 & 0 & 0 & S_{66} \end{bmatrix} \begin{Bmatrix} \sigma_1 \\ \sigma_2 \\ \sigma_3 \\ \tau_{23} \\ \tau_{13} \\ \tau_{12} \end{Bmatrix}.
\tag{4.4}
$$

In the above equation $S_{ij}\,(i,j=1,2,3,...,6)$ are compliances and are

$$
\begin{aligned}
S_{11} &= \frac{1}{E_1}, & S_{44} &= \frac{1}{G_{23}}, & S_{12} &= -\frac{\nu_{12}}{E_1} \\
S_{22} &= \frac{1}{E_2}, & S_{55} &= \frac{1}{G_{13}}, & S_{13} &= -\frac{\nu_{13}}{E_1} \\
S_{33} &= \frac{1}{E_3}, & S_{66} &= \frac{1}{G_{12}}, & S_{23} &= -\frac{\nu_{23}}{E_2}
\end{aligned}
\tag{4.5}
$$

where $E_i\,(i=1,2,3)$ are values for elasticity modulus in three directions, $G_{ij}\,(i,j=1,2,3)$ are values for shear modulus, and $\nu_{ij}\,(i,j=1,2,3)$ are Poisson ratios. The inverse relation becomes

$$\begin{Bmatrix} \sigma_1 \\ \sigma_2 \\ \sigma_3 \\ \tau_{23} \\ \tau_{13} \\ \tau_{12} \end{Bmatrix} = \begin{bmatrix} C_{11} & C_{12} & C_{13} & 0 & 0 & 0 \\ C_{12} & C_{22} & C_{23} & 0 & 0 & 0 \\ C_{13} & C_{23} & C_{33} & 0 & 0 & 0 \\ 0 & 0 & 0 & C_{44} & 0 & 0 \\ 0 & 0 & 0 & 0 & C_{55} & 0 \\ 0 & 0 & 0 & 0 & 0 & C_{66} \end{bmatrix} \begin{Bmatrix} \varepsilon_1 \\ \varepsilon_2 \\ \varepsilon_3 \\ \gamma_{23} \\ \gamma_{13} \\ \gamma_{12} \end{Bmatrix} \tag{4.6}$$

where C_{ij} $(i, j = 1,2,3,...,6)$ are values for component of stiffness matrix and are given by

$$C_{11} = \frac{S_{22}S_{33} - S_{23}S_{23}}{S}, \qquad C_{12} = \frac{S_{13}S_{23} - S_{12}S_{33}}{S}$$

$$C_{22} = \frac{S_{33}S_{11} - S_{13}S_{13}}{S}, \qquad C_{13} = \frac{S_{12}S_{23} - S_{13}S_{22}}{S}$$

$$C_{33} = \frac{S_{11}S_{22} - S_{12}S_{12}}{S}, \qquad C_{23} = \frac{S_{12}S_{13} - S_{23}S_{11}}{S} \tag{4.7}$$

$$C_{44} = \frac{1}{S_{44}}, \qquad C_{55} = \frac{1}{S_{55}}, \qquad C_{66} = \frac{1}{S_{66}}$$

$$S = S_{11}S_{22}S_{33} - S_{11}S_{23}S_{23} - S_{22}S_{13}S_{13} - S_{33}S_{12}S_{12} + 2S_{12}S_{23}S_{13}$$

For plane-stress case, where σ_3, τ_{23}, and τ_{13} are zero, equation (4.4) becomes

$$\begin{Bmatrix} \varepsilon_1 \\ \varepsilon_2 \\ \gamma_{12} \end{Bmatrix} = \begin{bmatrix} S_{11} & S_{12} & 0 \\ S_{12} & S_{22} & 0 \\ 0 & 0 & S_{66} \end{bmatrix} \begin{Bmatrix} \sigma_1 \\ \sigma_2 \\ \tau_{12} \end{Bmatrix} \tag{4.8}$$

And equation (4.6) becomes

$$\begin{Bmatrix} \sigma_1 \\ \sigma_2 \\ \tau_{12} \end{Bmatrix} = \begin{bmatrix} Q_{11} & Q_{12} & 0 \\ Q_{12} & Q_{22} & 0 \\ 0 & 0 & Q_{66} \end{bmatrix} \begin{Bmatrix} \varepsilon_1 \\ \varepsilon_2 \\ \gamma_{12} \end{Bmatrix}. \tag{4.9}$$

The Q_{ij} $(i, j = 1,2,6)$ are called the reduced stiffnesses and from equation (4.6) we have

$$Q_{11} = C_{11} - \frac{C_{13}^2}{C_{33}}$$

$$Q_{12} = C_{12} - \frac{C_{13}C_{23}}{C_{33}}$$

$$Q_{22} = C_{22} - \frac{C_{23}^2}{C_{33}}$$

$$Q_{66} = C_{66}$$

(4.10)

The compliance components in the above equation in terms of the engineering constants is (Hyer, 1998)

$$Q_{11} = \frac{E_1}{1 - \nu_{12}\nu_{21}}$$

$$Q_{12} = \frac{\nu_{12}E_2}{1 - \nu_{12}\nu_{21}} = \frac{\nu_{21}E_1}{1 - \nu_{12}\nu_{21}}$$

$$Q_{22} = \frac{E_2}{1 - \nu_{12}\nu_{21}}$$

$$Q_{66} = G_{12}$$

(4.11)

For an isotropic material the reduced stiffnesses become

$$Q_{11} = Q_{22} = \frac{E}{1 - \nu^2}$$

$$Q_{12} = \frac{\nu E}{1 - \nu^2}$$

$$Q_{66} = G = \frac{E}{2(1 + \nu)}$$

(4.12)

4.3 Modelling isotropic layers

Anti-wear layers and sheath layers can be modelled as an isotropic layer in plane-stress. Strains and equilibrium equations for only one isotropic layer are presented here. For more than one isotropic layer, the number of equilibrium equations will be multiplied

by the number of layers. A uniform strain state is assumed along the length of the pipe, so that the strains of isotropic layers are related to the displacements by the following equations

$$\varepsilon_1 = \frac{\Delta u_z}{L} + y\frac{\Delta\psi_x}{L} - x\frac{\Delta\psi_y}{L}$$

$$\varepsilon_2 = \frac{u_r}{R}$$

$$\gamma_{12} = R\frac{\Delta\phi}{L}$$

(4.13)

where L is total length of the riser, R is the radius of the middle surface and subscripts 1 and 2 indicate the longitudinal (parallel to z) and circumferential directions, respectively. The reference coordinate system x, y, z is shown in Figure 4.1. Furthermore, $\Delta u_z, \Delta\psi_x, \Delta\psi_y$ and $\Delta\phi$ indicate the change of u_z, ψ_x, ψ_y and ϕ over the length L.

Using the principle of virtual work, which implies equating the variation of the external work to the variation of the internal energy, the equilibrium equations are derived. Using equation (4.3), the strain energy U is

$$U = \frac{E}{2(1-v^2)}\iiint\left[\varepsilon_1^2 + \varepsilon_2^2 + 2v\varepsilon_1\varepsilon_2 + \frac{1-v}{2}\gamma_{12}^2\right]dV$$

(4.14)

Let

$$k = \frac{E}{(1-v^2)}$$

(4.15)

Substituting the above equation into equation of strain energy gives

$$U = \frac{1}{2}\int_V\left[k\varepsilon_1^2 + 2vk\varepsilon_1\varepsilon_2 + k\varepsilon_2^2 + G\gamma_{12}^2\right]dV$$

(4.16)

Taking its first variation gives

$$dU = \frac{1}{2} \int_V \left\{ 2k \left(\frac{\Delta u_z}{L} + y \frac{\Delta \psi_x}{L} - x \frac{\Delta \psi_y}{L} \right) \left(\frac{\delta \Delta u_z}{L} + y \frac{\delta \Delta \psi_x}{L} - x \frac{\delta \Delta \psi_y}{L} \right) \right.$$

$$+ 2 \frac{k}{R^2} \delta u_r \cdot u_r + 2\nu k \frac{u_r}{R} \left(\frac{\delta \Delta u_z}{L} + y \frac{\delta \Delta \psi_x}{L} - x \frac{\delta \Delta \psi_y}{L} \right)$$

(4.17)

$$+ 2\nu k \left(\frac{\Delta u_z}{L} + y \frac{\Delta \psi_x}{L} - x \frac{\Delta \psi_y}{L} \right) \frac{\delta u_r}{R} + 2 \frac{GR^2}{L^2} \Delta \phi \cdot \delta \Delta \phi \right\} dV$$

The potential of the external loads W which is the work done by all external loads under the specified incremental deformation is

$$W = N \Delta u_z + T \Delta \phi + M_x \Delta \psi_x + M_y \Delta \psi_y + \Delta p (2 \frac{u_r}{R} + \frac{\Delta u_z}{L}) \pi R^2 L$$

(4.18)

where N, T, M_x and M_y are the axial force, the axial torque, the moment about the normal direction, the moment about the bi-normal direction, respectively. Δp is the radial pressure differential across the layer, that is the difference between the internal pressure p^{in} and the external pressure p^{out}, that is $\Delta p = p^{in} - p^{out}$. Taking the first variation of external work gives

$$dW = N \delta \Delta u_z + T \delta \Delta \phi + M_x \delta \Delta \psi_x + M_y \delta \Delta \psi_y + \Delta p (2 \frac{\delta u_r}{R} + \frac{\delta \Delta u_z}{L}) \pi R^2 L$$

(4.19)

By equating external work to internal work and taking a first variation

$$dU = dW$$

(4.20)

The stationarity of the total potential energy provides the equilibrium equations for the isotropic layer, which in matrix form are given by

$$\begin{bmatrix} AE & 0 & 0 & 0 & \nu AE \\ 0 & EI_z\dfrac{1}{2}(1-\nu) & 0 & 0 & 0 \\ 0 & 0 & EI_x & 0 & 0 \\ 0 & 0 & 0 & EI_y & 0 \\ \nu AE & 0 & 0 & 0 & AE \end{bmatrix} \begin{Bmatrix} \dfrac{\Delta u_z}{L} \\ \dfrac{\Delta\phi}{L} \\ \dfrac{\Delta\psi_x}{L} \\ \dfrac{\Delta\psi_y}{L} \\ \dfrac{u_r}{R} \end{Bmatrix} = (1-\nu^2)\begin{Bmatrix} N+\pi R^2\Delta p \\ T \\ M_x \\ M_y \\ 2\pi R^2\Delta p \end{Bmatrix} \qquad (4.21)$$

where I_x and I_y are the second moment of inertia about axes x and y, I_z is the polar moment of inertia and A is the area of the cross section of the layer.

4.4 Modelling Carcass layer

Flexible risers are structures used under water and are therefore subjected to an external hydrostatic pressure especially in the installation phase. The internal interlocked helical layer, known as the carcass, is used primarily to take up the external pressure. A riser without the carcass layer can carry only a minimal amount of external pressure, since both the plastic tubes and the helical tendons have very low stiffnesses in the radial direction. Even without any hydrostatic pressure applied, the axisymmetric loading would cause an unrealistically large stretch, which occurs due to low stiffness of the riser (without the carcass layer) in the radial direction.

The structure of the carcass layer causes the stiffness in axial direction to be totally different comparing to the circumferential one, so that an orthotropic model is a reasonable choice. A linear elastic plane-stress orthotropic material model is chosen for the analytical formulation, which is governed by the following constitutive equation:

$$\begin{Bmatrix} \varepsilon_1 \\ \varepsilon_2 \\ \gamma_{12} \end{Bmatrix} = \begin{bmatrix} \dfrac{1}{E_z} & \dfrac{-\nu_{\theta z}}{E_\theta} & 0 \\ \dfrac{-\nu_{z\theta}}{E_z} & \dfrac{1}{E_\theta} & 0 \\ 0 & 0 & \dfrac{1}{G_{z\theta}} \end{bmatrix} \begin{Bmatrix} \sigma_1 \\ \sigma_2 \\ \sigma_{12} \end{Bmatrix} \qquad (4.22)$$

It is worth noting that the plane-stress assumption leads to a relation involving only strains and stresses in the 1 (or z) and 2 (or θ) directions, which are axial and circumferential directions respectively in a cylindrical coordinate system. The elasticity modulus in the circumferential direction is equal to that of a steel material. Because the carcass layer does not sustain much axial stress and hence the axial stress is not of much interest to the riser manufacturers, the elasticity modulus in the axial direction is chosen to be as small as possible compared to the circumferential direction. Values for material properties are checked to hold all material stability conditions, Equation (3.1), for an orthotropic layer. Substituting Equation (4.9) into the strain energy equation gives

$$U = \frac{1}{2}\int_V \left[Q_{11}\varepsilon_1^2 + 2Q_{12}\varepsilon_1\varepsilon_2 + Q_{22}\varepsilon_2^2 + Q_{66}\gamma_{12}^2 \right] dV \tag{4.23}$$

Substituting Equation (4.13) and taking first variation gives,

$$
\begin{aligned}
dU = \frac{1}{2}\int_V & \left\{ 2Q_{11}\left(\frac{\Delta u}{L} + y\frac{\Delta\psi_x}{L} - x\frac{\Delta\psi_y}{L} \right)\left(\frac{\delta\Delta u}{L} + y\frac{\delta\Delta\psi_x}{L} - x\frac{\delta\Delta\psi_y}{L} \right) \right. \\
& + 2Q_{22}\frac{1}{R^2}\delta u_r \cdot u_r + 2Q_{12}\frac{u_r}{R}\left(\frac{\delta\Delta u}{L} + y\frac{\delta\Delta\psi_x}{L} - x\frac{\delta\Delta\psi_y}{L} \right) \\
& \left. + 2Q_{12}\left(\frac{\Delta u}{L} + y\frac{\Delta\psi_x}{L} - x\frac{\Delta\psi_y}{L} \right)\frac{\delta u_r}{R} + 2Q_{66}\frac{R^2}{L^2}\Delta\phi \cdot \delta\Delta\phi \right\} dV
\end{aligned}
\tag{4.24}
$$

Substituting Equation (4.24) into the principle of virtual works and using the same formulation as in Equation (4.19) results in the following equilibrium equations in matrix form

$$
\begin{bmatrix}
AQ_{11} & 0 & 0 & 0 & AQ_{12} \\
0 & Q_{66}I_z & 0 & 0 & 0 \\
0 & 0 & Q_{11}I_x & 0 & 0 \\
0 & 0 & 0 & Q_{11}I_y & 0 \\
AQ_{12} & 0 & 0 & 0 & AQ_{22}
\end{bmatrix}
\begin{Bmatrix}
\frac{\Delta u_z}{L} \\
\frac{\Delta\phi}{L} \\
\frac{\Delta\psi_x}{L} \\
\frac{\Delta\psi_y}{L} \\
\frac{u_r}{R}
\end{Bmatrix}
=
\begin{Bmatrix}
N + \pi R^2\Delta p \\
T \\
M_x \\
M_y \\
2\pi R^2\Delta p
\end{Bmatrix}
\tag{4.25}
$$

4.5 Modelling helical armour layers

The equilibrium equations for the helical armour layer are derived in a manner similar to that outlined for the isotropic layer. The total linear strain for a tendon of a helical armour layer in the direction of tendon's axis is given by (Lanteigne, 1985; Bahtui *et al.*, 2008d):

$$
\varepsilon = \frac{\Delta u_z}{L}\cos^2\alpha + \frac{\Delta u_r}{R}\sin^2\alpha + R\frac{\Delta\phi}{L}\sin\alpha\cos\alpha
$$
$$
+ R\sin\theta\frac{\Delta\psi_x}{L}\cos^2\alpha + R\cos\theta\frac{\Delta\psi_y}{L}\cos^2\alpha
$$

(4.26)

where all quantities as well as those in Equations (4.27) and (4.28) are related to the helical armour layer, α is the lay angle of the tendon, and θ is the angular position of the tendon on the cross-section, as shown in Figure 4.2. With the assumption of linearly of elastic tendons and ignoring all stresses except the axial stress in the tendon, the elastic energy for the helical armour layer is the summation of this value for all tendons in that layer (Lanteigne, 1985)
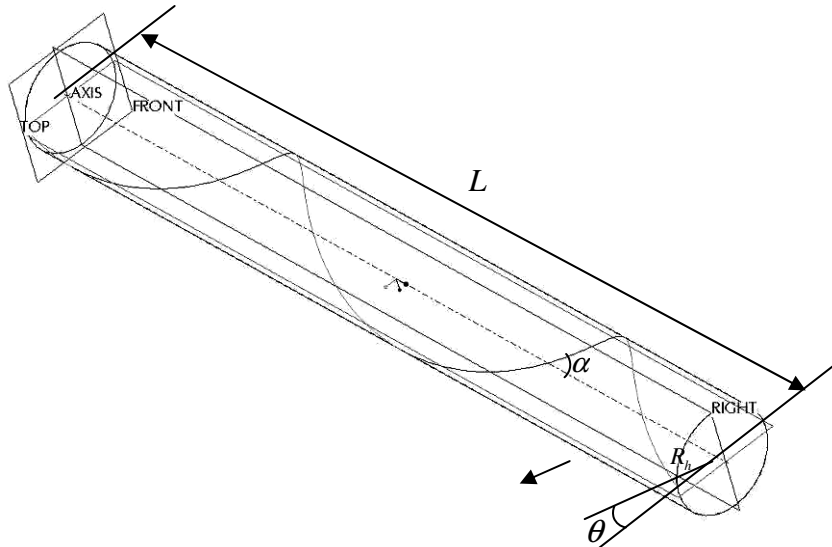

Figure 4.2: Geometry of a helix.

$$U = \frac{1}{2}\sum_{i=1}^{n} EA^i \int_L \left(\varepsilon^i\right)^2 \frac{dz}{\cos\alpha} \tag{4.27}$$

where n is the number of tendons in a layer, A^i is the cross-sectional area of the i_{th} tendon, and z is the axial direction. Following the principle of virtual works, used in Section 4.3, the equilibrium equations for the helical armour layer in matrix form are as follows:

$$\begin{bmatrix} \kappa_{11} & \kappa_{12} & 0 & 0 & \kappa_{15} \\ \kappa_{21} & \kappa_{22} & 0 & 0 & \kappa_{25} \\ 0 & 0 & \kappa_{33} & 0 & 0 \\ 0 & 0 & 0 & \kappa_{44} & 0 \\ \kappa_{51} & \kappa_{52} & 0 & 0 & \kappa_{55} \end{bmatrix} \begin{Bmatrix} \frac{\Delta u_z}{L} \\ \frac{\Delta\phi}{L} \\ \frac{\Delta\psi_x}{L} \\ \frac{\Delta\psi_y}{L} \\ \frac{u_r}{R} \end{Bmatrix} = \begin{Bmatrix} N + \pi R^2 \Delta p \\ T \\ M_x \\ M_y \\ 2\pi R^2 \Delta p \end{Bmatrix} \tag{4.28}$$

where the constants κ_{ij} $(i, j = 1,...,5)$ have the following expressions:

$$\kappa_{11} = nEA^i \cos^3\alpha$$
$$\kappa_{12} = nEA^i R \sin\alpha \cos^2\alpha$$
$$\kappa_{15} = nEA^i \sin^2\alpha \cos\alpha$$
$$\kappa_{22} = nEA^i R^2 \sin^2\alpha \cos\alpha$$
$$\kappa_{25} = nEA^i R \sin^3\alpha$$

$$\kappa_{33} = \frac{1}{L} nEA^i R^3 \cos^4\alpha \frac{\pi}{\tan\alpha}$$
$$\kappa_{44} = \frac{1}{L} nEA^i R^3 \cos^4\alpha \frac{\pi}{\tan\alpha}$$
$$\kappa_{55} = nEA^i \frac{\sin^4\alpha}{\cos\alpha}$$

$$\tag{4.29}$$

The matrix in Equation (4.28) is symmetric.

4.6 Bending stiffness analysis of helical armour layers in the slip phase

Friction is accounted for during bending loading and ignored in pressure, tension and torsion loading steps. That is because the latter types of loadings do not generate considerable energy dissipation due to friction. Contact (and slip) is assumed to occur between internal and external surfaces of different layers. Contact between tendons of each helical armour layer is ignored in the analytical model.

In order to include friction into the analysis for the case of the bending load, we follow an earlier work by Kraincanic and Kebadze (2001) and introduce the concept of critical bending curvatures, so that the bending process is divided into three phases: no-slip, partial slip and full slip. Accordingly, two critical values as minimum and maximum critical curvatures are defined. Curvatures smaller than the minimum critical curvature imply no slip. Curvatures between the minimum and maximum values imply that some tendons in the helical armour layer have already started to slip and some other tendons have not slipped yet (partial slip). Curvatures larger than maximum critical curvature imply full slip. The procedure to evaluate the maximum and minimum critical values is discussed in Kraincanic and Kebadze (2001) in detail, and therefore it is not reported here for the sake of brevity.

4.7 Total riser stiffness

The overall stiffness of the whole model is found by summing the stiffness contributions of the isotropic layers, the carcass layer and those of the helical armour layers. A unique length L is used for all layers, so that axial and torsional displacements as well as bending curvatures are the same for all layers. To include layer separation, layers are allowed to have different radial displacements, and all radial displacements are incorporated in the matrix of unknowns. Each layer has a different and unique initial radius R.

Consider a special case where the unbonded flexible riser of six-layers in Figure 3.1 is going to be modelled. By summing Equations (4.21), (4.25), and (4.28) together, the equilibrium equations for the whole riser are then written in the matrix form as follows

$$
\begin{bmatrix}
K_{11} & K_{12} & 0 & 0 & K_{15} & K_{16} & K_{17} & K_{18} & K_{19} & K_{1\,10} \\
K_{21} & K_{22} & 0 & 0 & 0 & 0 & K_{27} & 0 & K_{29} & 0 \\
0 & 0 & K_{33} & 0 & 0 & 0 & 0 & 0 & 0 & 0 \\
0 & 0 & 0 & K_{44} & 0 & 0 & 0 & 0 & 0 & 0 \\
K_{51} & 0 & 0 & 0 & K_{55} & 0 & 0 & 0 & 0 & 0 \\
K_{61} & 0 & 0 & 0 & 0 & K_{66} & 0 & 0 & 0 & 0 \\
K_{71} & K_{72} & 0 & 0 & 0 & 0 & K_{77} & 0 & 0 & 0 \\
K_{81} & 0 & 0 & 0 & 0 & 0 & 0 & K_{88} & 0 & 0 \\
K_{91} & K_{92} & 0 & 0 & 0 & 0 & 0 & 0 & K_{99} & 0 \\
K_{10\,1} & 0 & 0 & 0 & 0 & 0 & 0 & 0 & 0 & K_{10\,10}
\end{bmatrix}
\begin{bmatrix}
\frac{\Delta u_z}{L} \\
\frac{\Delta \phi}{L} \\
\frac{\Delta \psi_x}{L} \\
\frac{\Delta \psi_y}{L} \\
\frac{u_r|_1}{R_1} \\
\frac{u_r|_2}{R_2} \\
\frac{u_r|_3}{R_3} \\
\frac{u_r|_4}{R_4} \\
\frac{u_r|_5}{R_5} \\
\frac{u_r|_6}{R_6}
\end{bmatrix}
=
\begin{bmatrix}
N_T \\
T_T \\
M_{xT} \\
M_{yT} \\
2\pi R_1^2 \Delta p_1 \\
2\pi R_2^2 \Delta p_2 \\
2\pi R_3^2 \Delta p_3 \\
2\pi R_4^2 \Delta p_4 \\
2\pi R_5^2 \Delta p_5 \\
2\pi R_6^2 \Delta p_6
\end{bmatrix}
\qquad (4.30)
$$

where the $i(i=1,\ldots,6)$ subscript indicates components in the i_{th} layer and layers are numbered as in Figure 3.1. The coefficients K_{33} and K_{44} depend on the bending curvatures and vary during the bending process (Kraincanic and Kebadze 2001). The values $K_{ij}(i,j=1,\ldots,10)$ of the total stiffness matrix and of the force vectors N_T, T_T, M_{xT} and M_{yT} are calculated from Equation (4.30). The expressions of the coefficients of the total stiffness matrix are given by

$$
\begin{aligned}
K_{11} &= \frac{E_2 A_2}{1-\nu_2^2} + \frac{E_4 A_4}{1-\nu_4^2} + \frac{E_6 A_6}{1-\nu_6^2} + n_3 E_3 A_3 \cos^3 \alpha_3 + n_5 E_5 A_5 \cos^3 \alpha_5 + A_1 Q_{11} \\
K_{12} &= n_3 E_3 A_3 R_3 \sin \alpha_3 \cos^2 \alpha_3 + n_5 E_5 A_5 R_5 \sin \alpha_5 \cos^2 \alpha_5 \\
K_{15} &= \frac{\nu_2 E_2 A_2}{(1-\nu_2^2)R_2^2}, \qquad K_{16} = \frac{\nu_6 E_6 A_6}{(1-\nu_6^2)R_6^2} \\
K_{17} &= n_3 E_3 \frac{A_3}{R_3^2} \cos \alpha_3 \sin^2 \alpha_3, \qquad\qquad K_{18} = \frac{\nu_4 E_4 A_4}{(1-\nu_4^2)R_4^2} \\
K_{19} &= n_5 E_5 \frac{A_5}{R_5^2} \cos \alpha_5 \sin^2 \alpha_5, \qquad\qquad K_{110} = A_1 Q_{12}
\end{aligned}
\qquad (4.31)
$$

49

$$K_{22} = \frac{E_2 I_{z2}}{2(1+v_2)} + \frac{E_4 I_{z4}}{2(1+v_4)} + \frac{E_6 I_{z6}}{2(1+v_6)} + n_3 E_3 A_3 R_3^2 \sin^2 \alpha_3 \cos \alpha_3$$

$$+ n_5 E_5 A_5 R_5^2 \sin^2 \alpha_5 \cos \alpha_5 + Q_{66} I_{z1}$$

$$K_{27} = n_3 E_3 \frac{A_3}{R_3} \sin^3 \alpha_3, \qquad K_{29} = n_5 E_5 \frac{A_5}{R_5} \sin^3 \alpha_5$$

$$K_{33} = \frac{E_2 I_{x2}}{1-v_2^2} + \frac{E_4 I_{x4}}{1-v_4^2} + \frac{E_6 I_{x6}}{1-v_6^2} + \frac{1}{L} n_3 E_3 A_3 R_3^3 \pi \frac{\cos^5 \alpha_3}{\sin \alpha_3}$$

$$+ \frac{1}{L} n_5 E_5 A_5 R_5^3 \pi \frac{\cos^5 \alpha_5}{\sin \alpha_5} + Q_{11} I_{x1}$$

$$K_{44} = \frac{E_2 I_{y2}}{1-v_2^2} + \frac{E_4 I_{y4}}{1-v_4^2} + \frac{E_6 I_{y6}}{1-v_6^2} + \frac{1}{L} n_3 E_3 A_3 R_3^3 \pi \frac{\cos^5 \alpha_3}{\sin \alpha_3}$$

$$+ \frac{1}{L} n_5 E_5 A_5 R_5^3 \pi \frac{\cos^5 \alpha_5}{\sin \alpha_5} + Q_{11} I_{y1}$$

$$K_{55} = \frac{E_2 A_2}{(1-v_2^2) R_2^3}, \qquad K_{66} = \frac{E_6 A_6}{(1-v_6^2) R_6^3}$$

$$K_{77} = n_3 E_3 A_3 \frac{\sin^4 \alpha_3}{R_3^3 \cos \alpha_3}, \qquad K_{88} = \frac{E_4 A_4}{(1-v_4^2) R_4^3}$$

$$K_{99} = n_5 E_5 A_5 \frac{\sin^4 \alpha_5}{R_5^3 \cos \alpha_5}, \qquad K_{1010} = A_1 Q_{22}$$

$$N_T = \sum_{i=1}^{5} N_i + \pi \sum_{i=1}^{5} p_i R_i^2 = \sum_{i=1}^{5} N_i + \pi \left(R_2^2 P_{in} - R_6^2 P_{out} \right)$$

$$T_T = \sum_{i=1}^{5} T_i, \qquad M_{xT} = \sum_{i=1}^{5} M_{xi}, \qquad M_{yT} = \sum_{i=1}^{5} M_{yi}$$

where the subscripts refer to the different layers as in Table 3.1.

To solve Equation (4.30), the interlayer contact pressures $\Delta p_1, ..., \Delta p_6$ within the load matrix should be known. These values depend on the unknown displacement vector in Equation (4.30) and therefore an iterative scheme has to be used.

At each iteration, the interlayer contact pressures applied to each layer should be calculated to act as an input for the next iteration. These values for the helical armour layers, Δp_3 and Δp_5, are derived by Lanteigne (1985):

$$\Delta p = nA\varepsilon \frac{\sin^2 \alpha}{2\pi R^2 \cos \alpha} \tag{4.32}$$

Although the carcass layer is the innermost layer, the internal pressure is, in practice, applied to the outer layer after the carcass layer, whereby $\Delta p_1 = 0$. To calculate the three interlayer contact pressures $\Delta p_2, \Delta p_4$ and Δp_6, some equations are needed. One equation comes from the pressure equilibrium equations

$$
\begin{aligned}
p_i^{out} &= p_{i+1}^{in}, \quad i = 1,...,5 \\
p_i^{out} &= p_i^{in} - \Delta p_i, \quad i = 1,...,6
\end{aligned}
\tag{4.33}
$$

which yields

$$
\Delta p_2 + \Delta p_4 + \Delta p_6 = P_{in} - P_{out} - \Delta p_3 - \Delta p_5
\tag{4.34}
$$

where P_{in} and P_{out} are the internal and external input pressures, respectively.

The remaining equations come from the continuity of radial displacements. Therefore the following compatibility relationships for all layers would need to be satisfied:

$$
\Delta r_i^{out} = \Delta r_{i+1}^{in}, \quad i = 2,...,5
\tag{4.35}
$$

where Δr^{out} and Δr^{in} are the change in the outer and the inner radiuses R^{out} and R^{in} at each layer. Assuming the helical armour layers to move rigidly in the radial direction
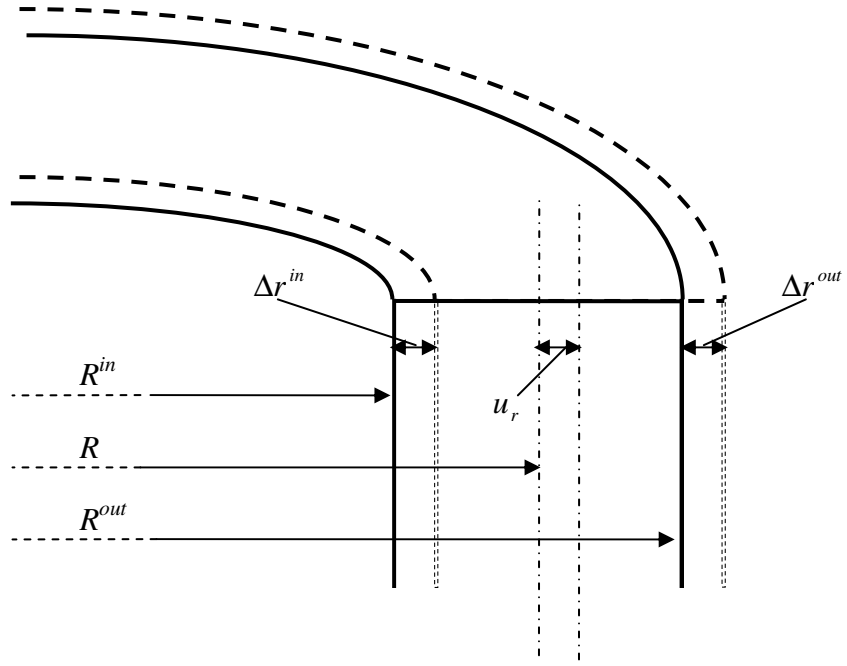
Figure 4.3: Side view of a single layer before and after deflection.

($\Delta r_3^{in} = \Delta r_3^{out}$ and $\Delta r_5^{in} = \Delta r_5^{out}$) results in Equations (4.35) to reduce to two equations

$$\Delta r_i^{out} = \Delta r_{i+2}^{in}, \quad i = 2,4. \tag{4.36}$$

The changes in the thicknesses for the isotropic layers are:

$$\Delta t_i = \Delta r_i^{out} - \Delta r_i^{in}, \quad i = 2,4,6. \tag{4.37}$$

where t_i is the thickness of layer i. Δt can also be calculated from the theory of strength of materials for an isotropic hollow cylinder:

$$\Delta t_i = \Delta p_i \frac{R_i^2}{t_i} \frac{2-v_i}{2E_i} - \frac{v_i N_i R_i}{A_i E_i}, \quad i = 2,4,6. \tag{4.38}$$

On the other hand the following equation holds in the radial direction for each layer (Figure 4.3):

$$R_i + u_r\big|_i = \frac{R^{in} + \Delta r^{in} + R^{out} + \Delta r^{out}}{2}, \quad i = 2,...,6. \tag{4.39}$$

Substituting the compatibility Equations (4.36) and Equations (4.37-38) into the Equations (4.39) results in the following five equations

$$2R_i + 2u_r\big|_i = R_i^{in} + 2\Delta r_i^{in} + R_i^{out} + \Delta p_i \frac{R_i^2}{t_i} \frac{2-v_i}{2E_i} - \frac{v_i N_i R_i}{A_i E_i}, \quad i = 2,4,6$$

$$2R_i + 2u_r\big|_i = R_i^{in} + 2\Delta r_{i-1}^{in} + R_i^{out} + 2\Delta p_{i-1} \frac{R_{i-1}^2}{t_{i-1}} \frac{2-v_{i-1}}{2E_{i-1}} - 2\frac{v_{i-1} N_{i-1} R_{i-1}}{A_{i-1} E_{i-1}}, \quad i = 3,5. \tag{4.40}$$

Equations (4.40) together with the pressure equilibrium equation (4.34) provide six sufficient equations which then are used to find all six unknowns at each iteration, which are three pressure imbalances $\Delta p_2, \Delta p_4$ and Δp_6 and three values for $\Delta r_2^{in}, \Delta r_4^{in}$ and Δr_6^{in}.

In case of layer separation, Equations (4.35) should be overwritten using a switch algorithm which will be discussed in Section 4.8 in detail. Convergence is achieved when the pressure equilibrium and the compatibility equations are all satisfied.

## 4.8 Layer separation and penetration

The amount of gap between layers, when separation occurs, can be derived using the interlayer pressures and the compatibility equations. If two layers are in contact and separation has not occurred, the value for the interlayer pressure is greater or equal to zero. Otherwise, in the case of layer separation, the value for the interlayer pressure would become negative. In this case we should re-write the compatibility equations (4.35) as

$$\Delta r_i^{out} = \Delta r_{i+1}^{in} + \eta_i, \quad i = 2,...,5 \tag{4.41}$$

where η_i is the amount of the positive gap between layers i and $i+1$. The solution procedure starts by setting the values for all η_i variables zero and subsequently finding the interlayer pressures between all layers. If the interlayer pressure value for each layer i is positive, which means layer separation has not occurred, η_i is zero. In this case Equations (4.35) should be used. Otherwise, if the interlayer pressure is negative, which is physically impossible, the value for those negative interlayer pressures should be replaced by zero and the compatibility equations (4.35) should switch to Equations (4.41) for those layers. Using this scheme ensures that the values for η_i are always positive, which means layer penetration will not occur.

An iterative solution scheme is used to prevent layer penetration. The analytical formulation is coded in MATLAB (2006). The switch algorithm with the algorithmic steps is shown in Table 4.1.

Table 4.1: Schematic flow-chart of the analytical computation.
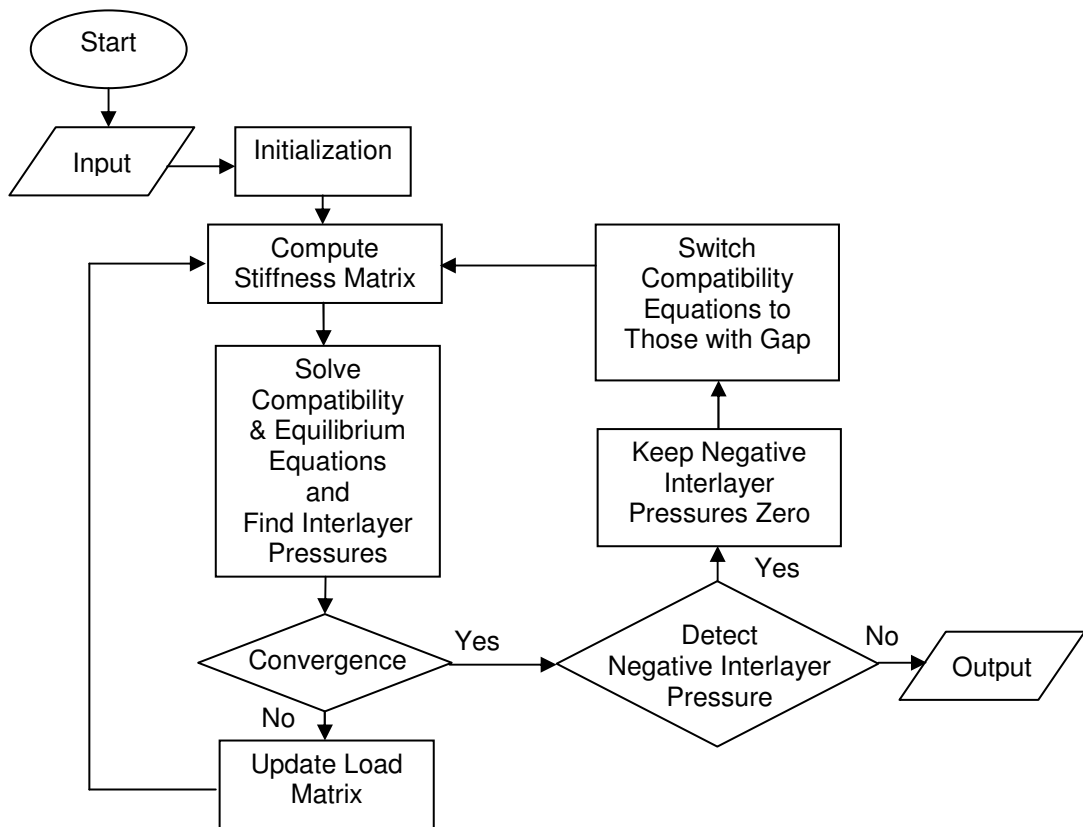
5 Validation and Verification of the Numerical and the Analytical Modelling

5.1 Introduction

There are no published experimental results in the literature with sufficient input data which would allow a comparison with the work outlined in this thesis. To demonstrate the accuracy, stability and computational suitability of the method, three case studies have been carried out using analytical and numerical models, described in Chapters 4 and 3, and comparisons were made between the results computed using each method.

Unbonded flexible riser is usually a three–dimensional phenomenon that cannot be reduced to a two-dimensional symmetric problem. Comparison is made between the results from analytical work and the fully three-dimensional numerical analysis for various load cases which include axial, torsional, and bending loads. In each case, an internal and/or external pressure loading is applied initially, followed by the application of an external loading and unloading event. A fully explicit solution scheme is adopted and the total energy during the loading and unloading events is monitored carefully to ensure that a smooth converged solution is achieved.

Results for the six-layer unbonded flexible riser are illustrated in the form of stress contour plots (Figures 5.1, 5.3, 5.4, 5.6, 5.7 and 5.11) and are compared between analytical and numerical solutions (Figures 5.2, 5.5 and 5.8). The load cases used in these case studies are typical modes of loading to which the riser is subjected to. The results shown in Figures 5.2, 5.5 and 5.8 include the results from the last two steps i.e. the external loading and the unloading steps. The pressure step causes an initial bulging out in the radial direction and shortening in the axial direction of the riser. Additionally an initial rotation of the layers also takes place due to the helical effects in the geometry of the riser. These effects are shown in Figures 5.2 and 5.5 as initial displacement and rotation, respectively.

5.2 Case 1: Pressure and tension loads

Result for the axial-stress contour plot for the first problem, the riser subjected to tension, is shown in Figure 5.1 (Bahtui *et al.*, 2008a). Hoop and radial stress results were well below the axial stresses. The magnitude of hoop stress for the riser is below 51MPa and result for the radial stress is below 35MPa. Therefore axial-stress contour plot was selected because it shows higher value of the stresses. As the stresses were concentrated mostly at the helical armour layer, other layers were hidden in the figure in order to present a better view of the maximum stress distribution. Figure 5.1 shows that axial stresses in the inner tensile armour layer are almost 1.2 times greater than those in the outer tensile armour layer because of the difference in their radii.

Figure 5.2 shows the axial displacement of the riser. It is seen in this figure that the finite element results are in good agreement with those obtained from the analytical model. The solid line which corresponds to the analytical model exhibits a linear relationship. This is due to the fact that the analytical formulation does not include the frictional effects.
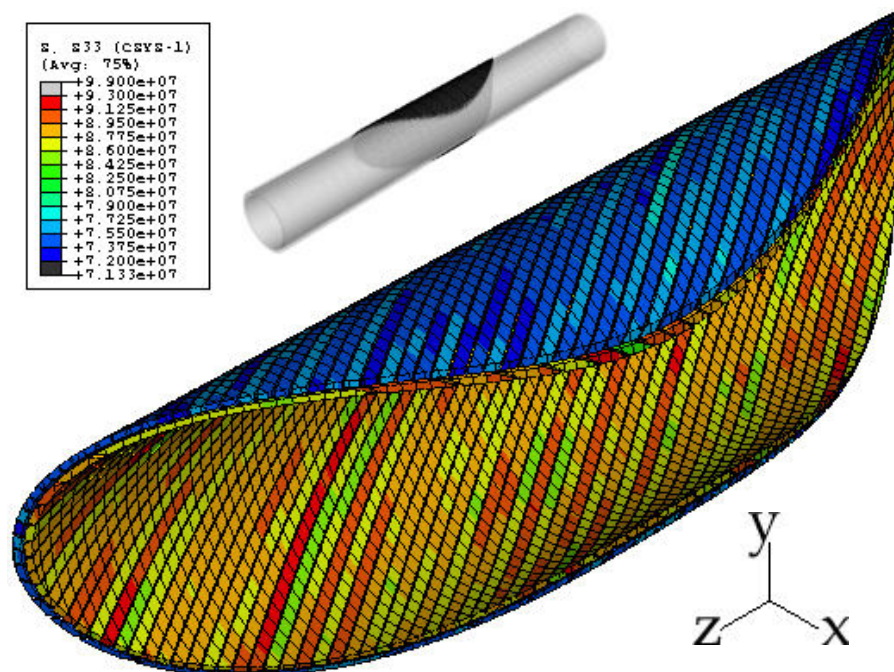

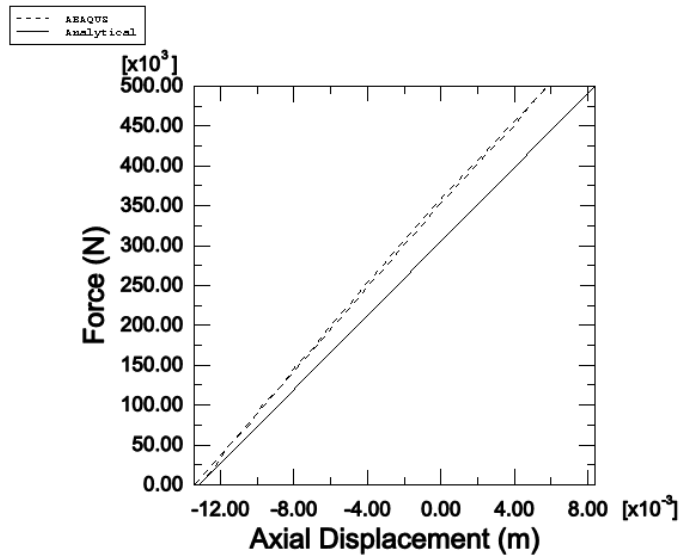Figure 5.1: Axial-stress contour plot for a cross section at the middle of the riser under tensile loading (Pa).

Figure 5.2: Axial force vs. displacement at the top reference point.

The ABAQUS result is however more realistic since the numerical model takes into account various details of the physical riser which are not possible to include in the analytical model.
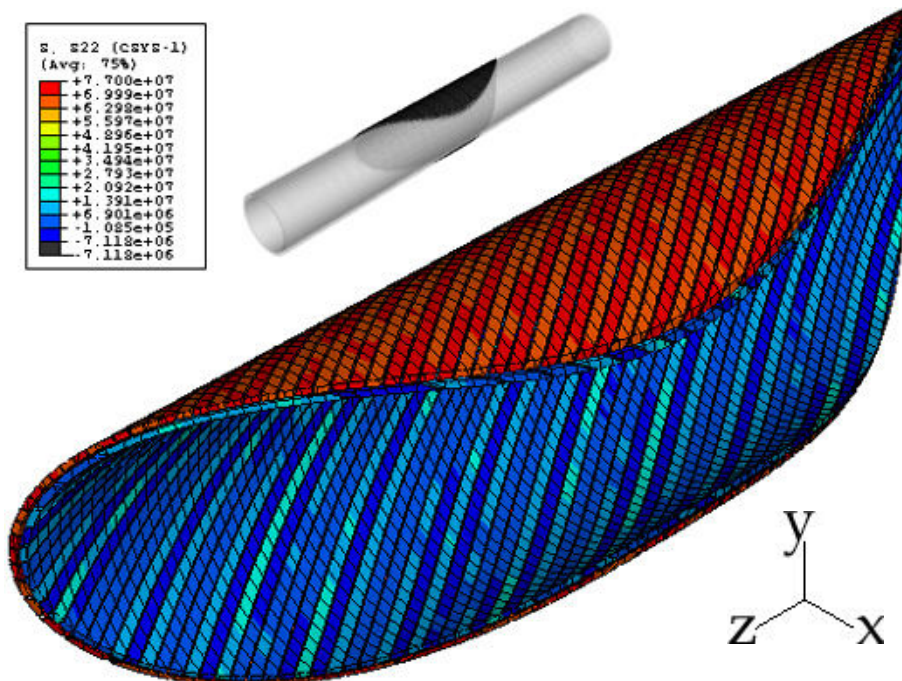

Figure 5.3: Hoop-stress contour plot for a cross section at the middle of the riser under torsional loading (Pa).
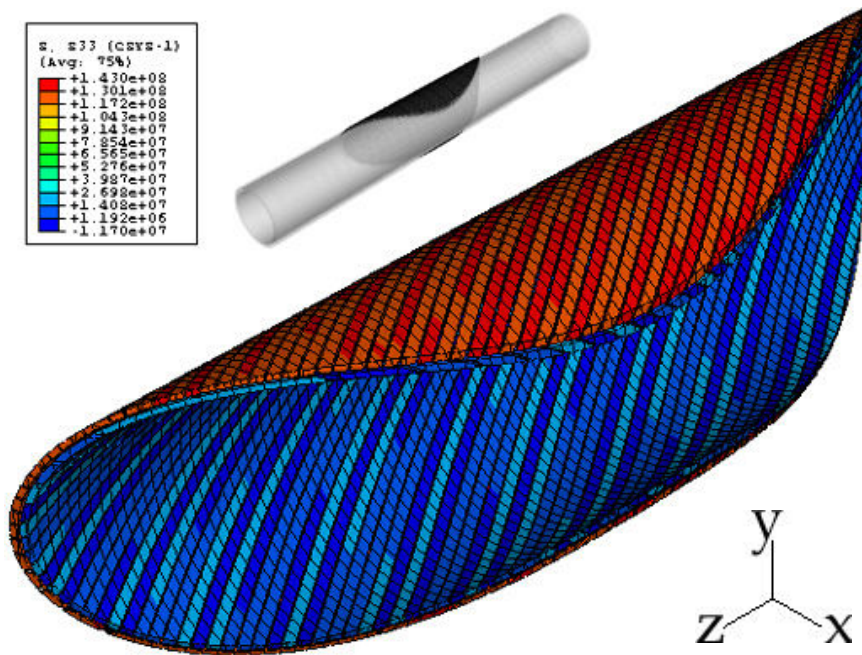
Figure 5.4: Axial-stress contour plot for a cross section at the middle of the riser under torsional loading (Pa).

5.3 Case 2: Pressure and torsion loads

Figure 5.3 and 5.4 show contour plots of the hoop-stress and axial-stress component for the riser subjected to linear torsional loading. Helix layers expose high hoop stress compared to other layers. In order to gain a better view of maximum stress distribution, other layers have been hidden in these figures. Stress values are tensile in the outer helical layer and compressive in the inner one. The torsional load is applied in the direction which causes tightening of helical armour layers causing the anti-wear layer to go into compression. A torsional load in the opposite direction will cause bird-caging effect. Axial stress is not significantly higher than hoop stress. This is due to helical geometry of helix armour layers which convert torsional load to axial strain and decrease the magnitude of axial stress. Figure 5.5 shows a plot of rotation versus the applied torque. The initial counter-clockwise offset in rotation is due to the initial rotation which was induced in the pressure step.
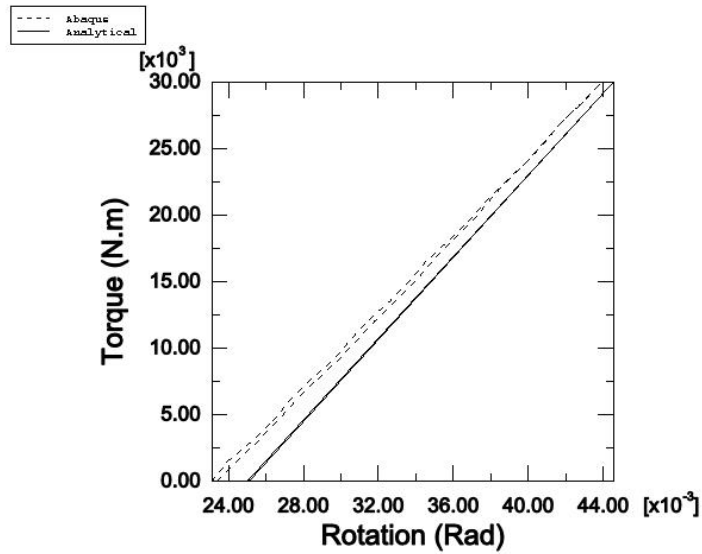
Figure 5.5: Torque vs. axial rotation at the top reference point.

5.4 Case 3: Pressure and bending loads

Figures 5.6 and 5.7 correspond to the case of bending load and show contour for the radial and axial component of the stress. Radial stress changes periodically along the length of the riser between tensile to compressive values. Figure 5.7, however, shows the stresses for the outer (a) and inner (b) helical armour layers separately. Both helical armour layers have higher axial stresses at the upper layer's half than that of the lower part. The inner helical armour layer has higher stresses because it has smaller cross-sectional second moment of inertia comparing to the outer helical armour layer.

Figure 5.8 illustrates the variation of the bending moment against curvature. Results shown are highly nonlinear because of the significant frictional sliding. The solid line corresponds to the analytical results which are the results from the first loading-unloading cycle. The loading phase in the analytical results consists of three sections: curvatures smaller than the minimum critical curvature (OA), curvatures between the minimum and the maximum critical curvatures (AB), and curvature greater than the maximum critical curvature (BC). This is not the case for the unloading phase, which only consists of curvatures greater than the maximum critical curvature. The numerical

results are much more realistic due to the fact that the numerical model gradually takes into account the effect of friction, as the curvature increases.

Abaqus results show the hysteresis effect in the unbonded type of flexible riser which exists in all load cases, but are particularly significant in the bending case, as shown in Figure 5.8, where the loading and unloading paths are well distinct. Results in this figure follow a hysteresis pattern which already has been published in the literature (Kraincanic and Kebadze, 2001) as experimental results and is presented here in Figure 5.9. Figure 5.9 shows theoretical prediction and experimental measurements of the bending moment-curvature for a 2.5 inch flexible pipe under 300 bar internal pressure.
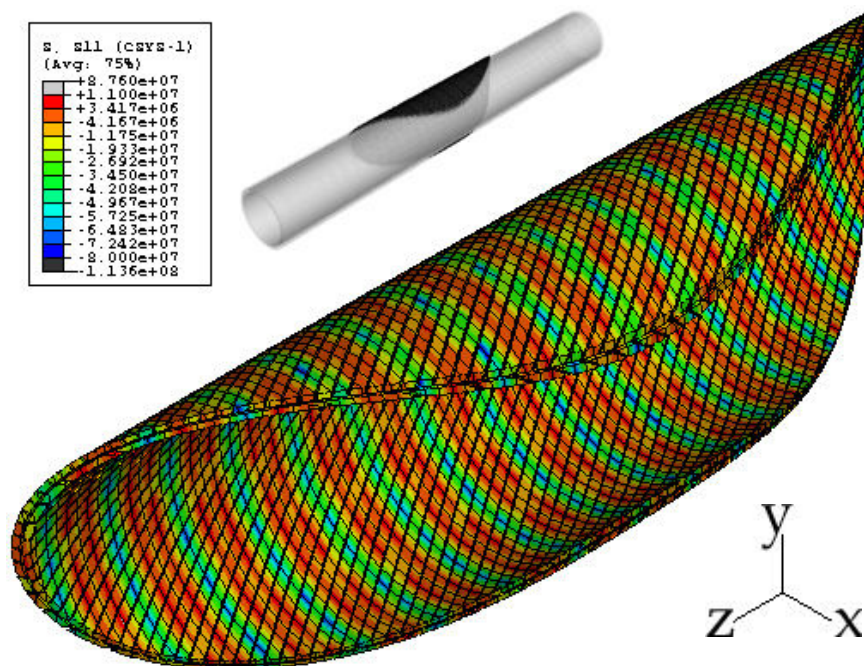

Figure 5.6: Radial-stress contour plot for a cross section at the middle of the riser under bending loading (Pa).
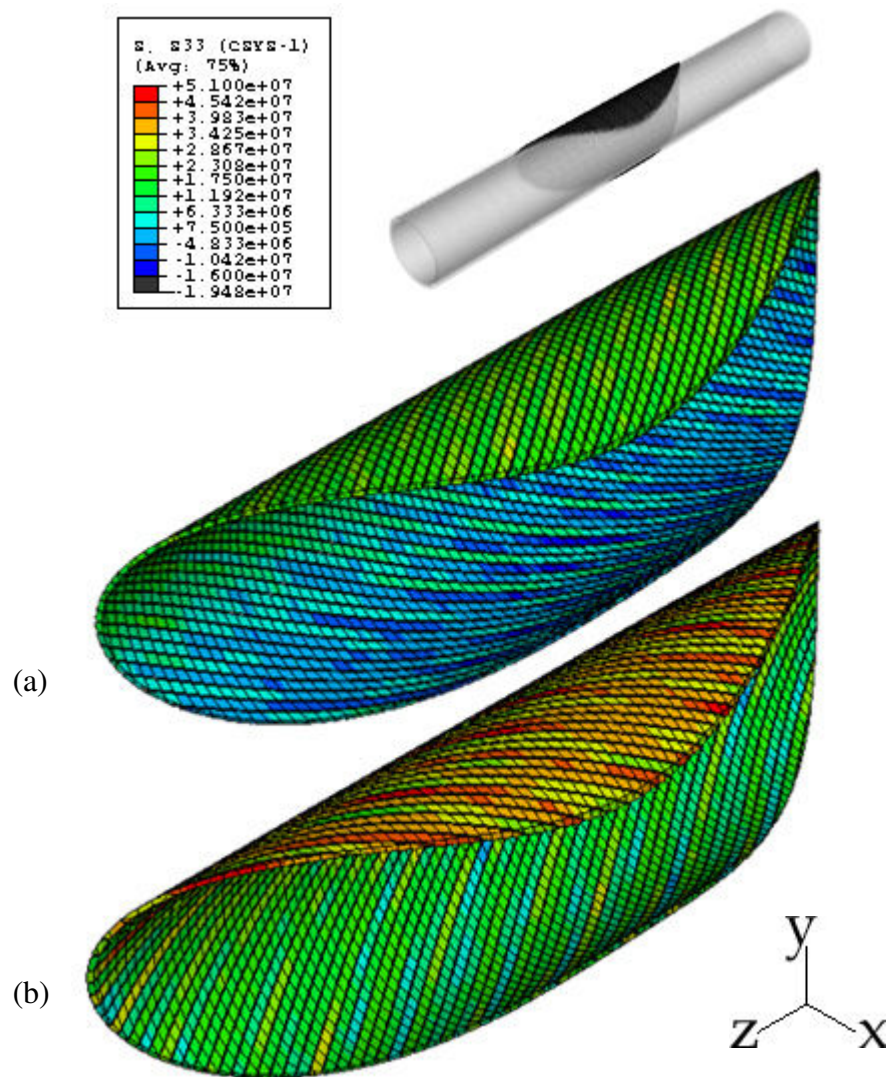
Figure 5.7: Axial-stress contour plot for a cross section at the middle of the riser under bending loading (Pa); (a): outer helix layer; (b): inner helix layer.
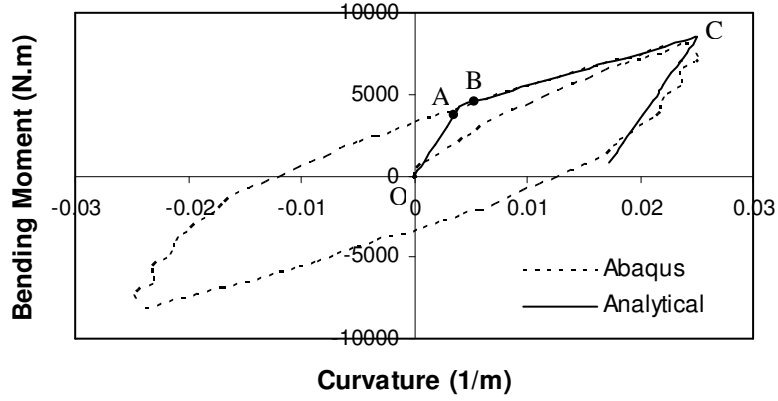
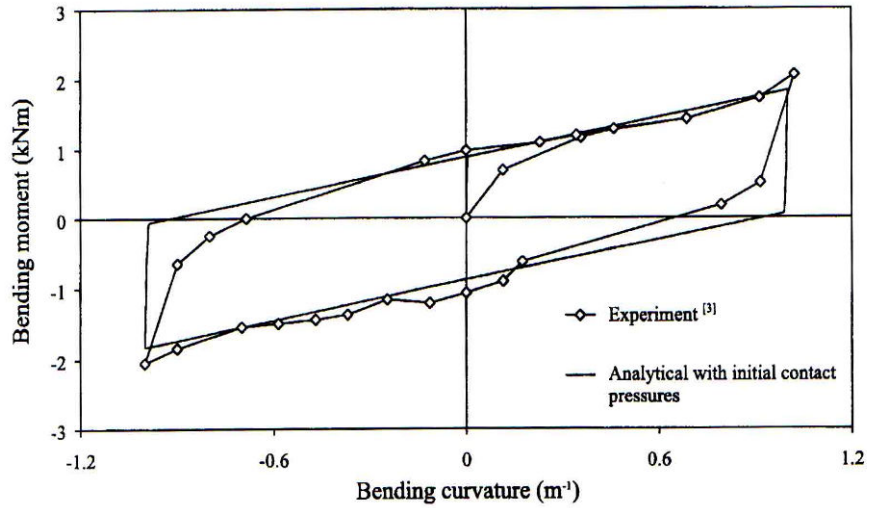Figure 5.8: Bending moment vs. curvature.

Figure 5.9: Theoretical prediction and experimental measurements of the bending moment-curvature reported in Reference (Kraincanic and Kebadze, 2001).

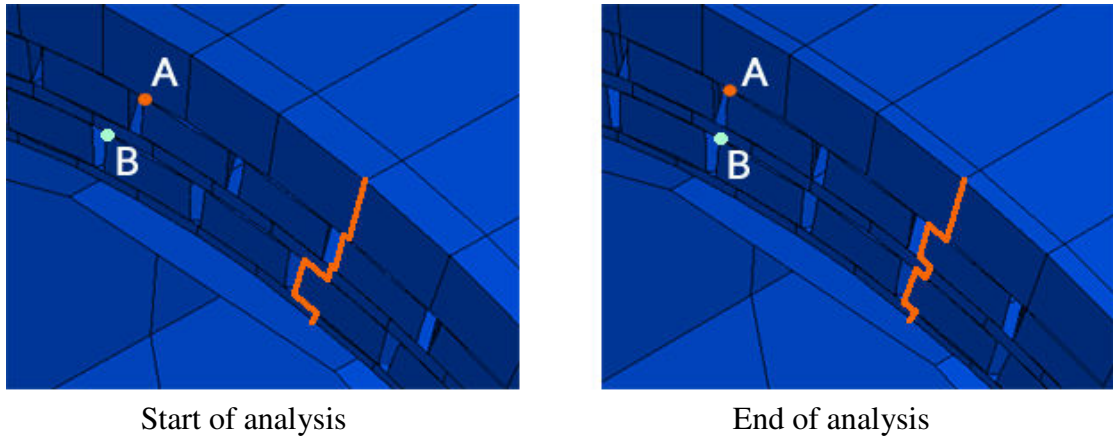Start of analysis   End of analysis

Figure 5.10: Slipping between adjacent layers.

Figure 5.10 illustrates the amount of slippage which occurs between all layers. It can be seen that, the distance between two selected points A and B in the left-hand side figure is more than that in the right-hand side figure. The two line paths in both figures, which pass through edges of elements, also show that rotations for the two helical armour layers are in opposite directions. This indicates the significant amount of frictional slippage occurring between all layers, which in turn results in significant amount of
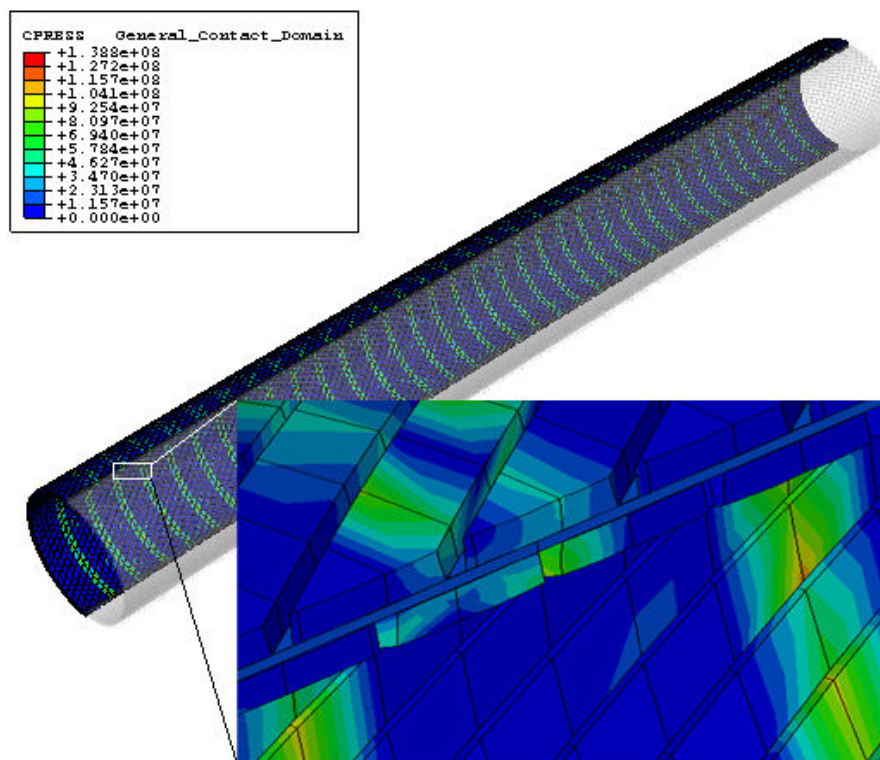

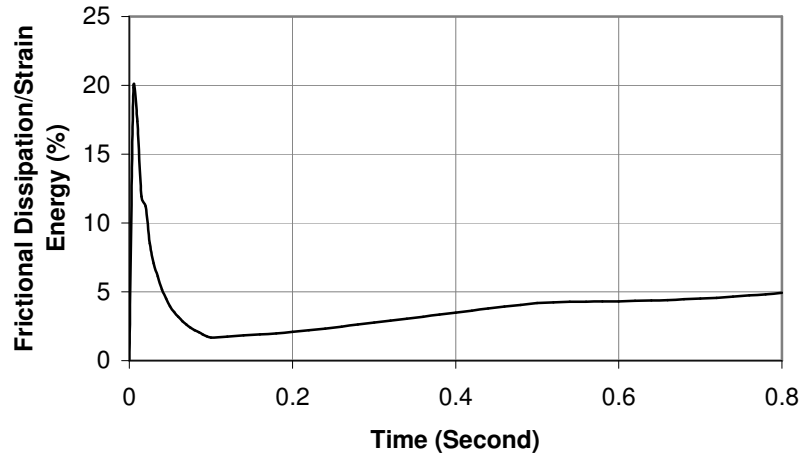Figure 5.11: Maximum contact pressure contour plot (Pa).

Figure 5.12: Percentage of energy dissipation to the strain energy.

energy dissipation. Figure 5.11 shows the contour plot for the maximum contact pressure between two helical armour layers and the tube layer, which is calculated as the magnitude of the net contact normal force per unit area.

Figure 5.12 shows the percentage of frictional energy dissipation to strain energy for Case 3. The results shown in this figure include the results from all steps i.e. the initial pressure, external loading and the unloading steps. The curve starts with a short impulse which is due to the impact caused by the initial pressure loading step. As the pressure increases, the gaps between layers close and a stable contact between layers establishes. As seen, the amount of energy dissipation is increasing gradually and smoothly afterward which is due to frictional slippage between all adjacent layers.

5.5 Cyclic loading analysis

In order to gain a better understanding of the energy dissipation phenomenon which occurs due to the existence of slippage between various layers in unbonded flexible risers, the riser's behaviour under cyclic loading is analysed. The same model, presented in Chapter 3, excluding carcass layer was utilised to investigate the cyclic axial and torsional loading. Then, the original six-layer model, which includes carcass layer, was utilised to investigate the cyclic bending moment (Bahtui *et al.*, 2007).

Figures 5.13 and 5.15 represent two common cyclic load cases, one for axial force and another for torsional load, which consist of four loading and unloading steps, preceded by only one pressure loading step at the beginning. In this example, a 23MPa internal pressure as well as a 3MPa external pressure was applied. All boundary conditions are the same as those in the pervious section. Other details of the riser are also the same as those in the pervious section. Figure 5.14 shows the axial displacement as a function of axial input force. An offset at the beginning is due to the pressure loading step. Results for the second and subsequent cycles are consistent with each other but are different from the first cycle.
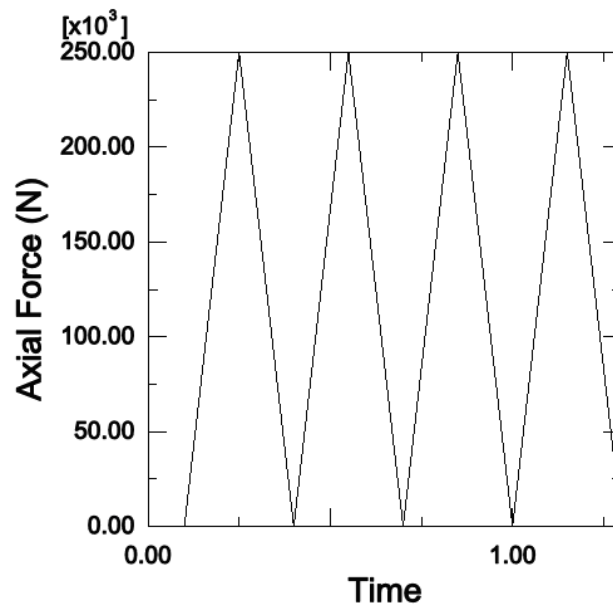

Figure 5.13: Axial force vs. time, for the case of cyclic loading.
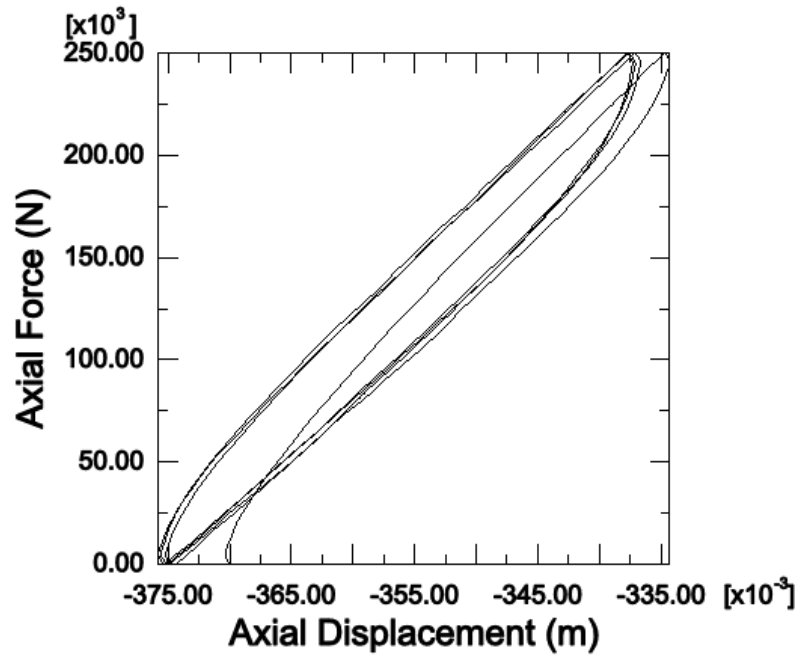
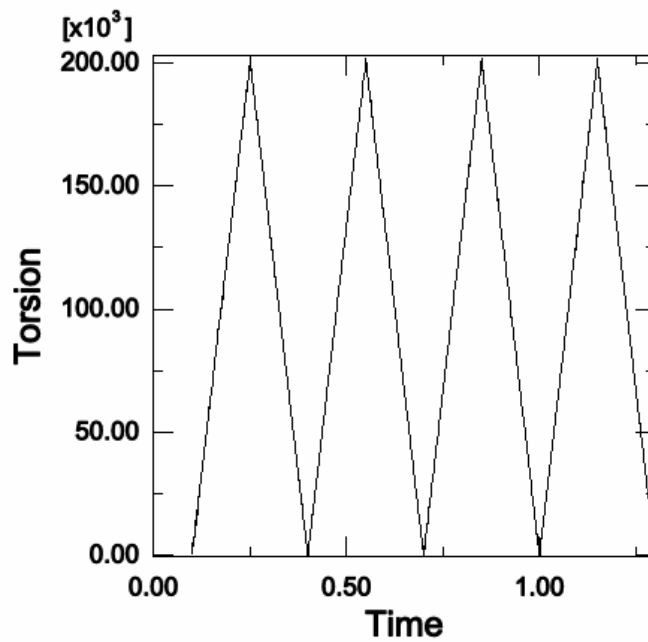Figure 5.14: Axial force vs. axial displacement, for the cyclic loading case.

Figure 5.15: Torsion vs. time, for the case of cyclic loading.
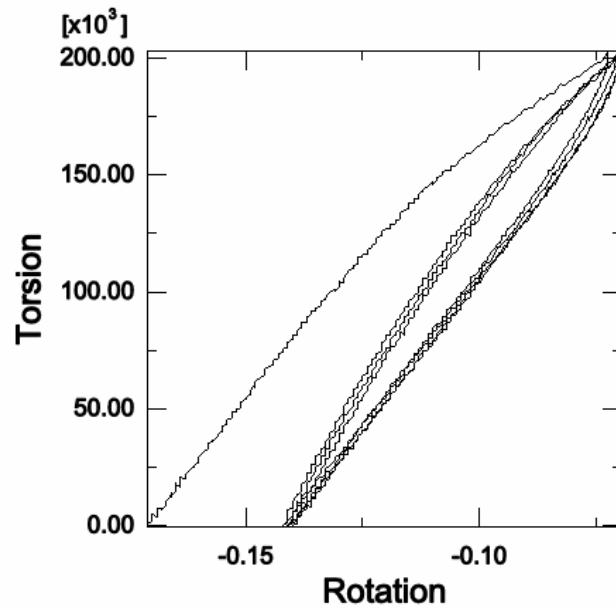
Figure 5.16: Torsion vs. rotation, for the cyclic loading case.
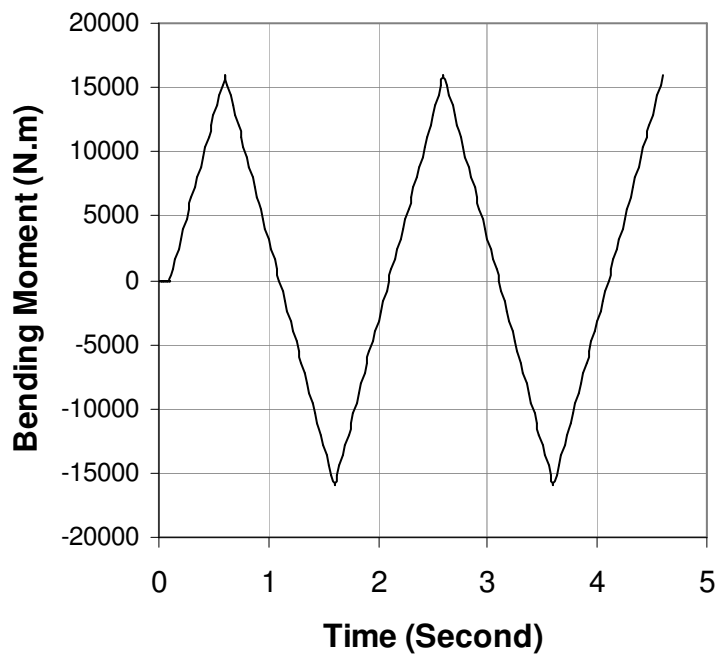
Figure 5.17: Bending moment vs. time, for the case of cyclic loading.

Figure 5.16 shows the rotation as a function of torsional input force (Figure 5.15). The different paths between loading and unloading curves show the hysteresis effect. The first cycle includes the displacement due to inter-layer gap closure resulting in a different curve compared to those for the subsequent cycles.

The same model, introduced in the last chapter, including the carcass layer was subjected to 16 kNm cyclic bending moment resulting in the curves shown in Figure 5.17. The loading consists of four and half loading and unloading steps, preceded by only one pressure loading step at the beginning. In this example, a 30MPa internal pressure as well as a 23.4MPa external pressure was applied. As seen, the model, including the carcass layer sustains much higher external pressures. All boundary conditions are the same as the pervious example. Result for the curvature is shown in Figure 5.18 where significant hysteresis effects can be seen.
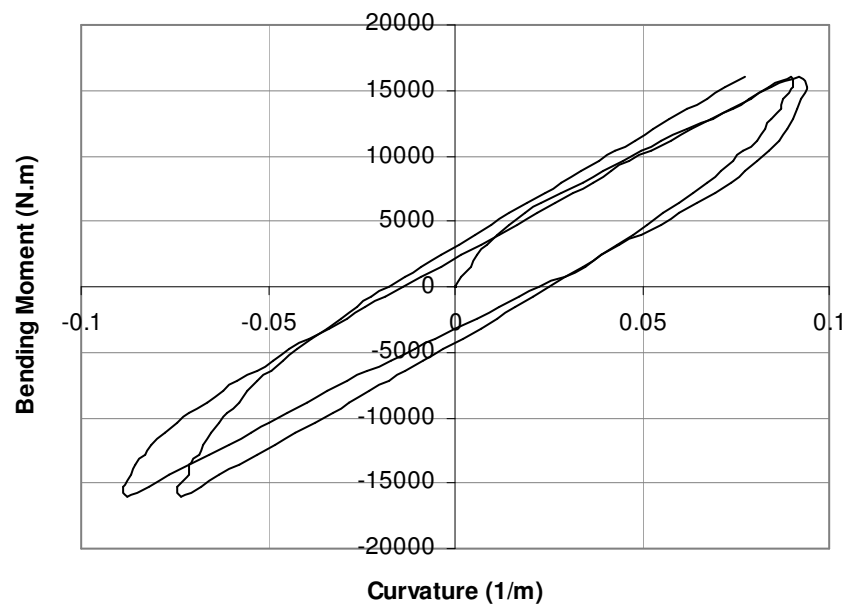
Figure 5.18: Bending moment vs. curvature, for the cyclic loading case.

5.6 Energy dissipation

Figure 5.19 shows the percentage of frictional energy dissipation to strain energy for bending moment cyclic loading analysis in Section 5.5. The results shown in this figure include the results from all steps i.e. the initial pressure, external loading and the unloading steps. The curve starts with a jump which is due to the impact caused by the initial pressure loading step. As the pressure increases, the gaps between layers close and a stable contact between layers is established. As seen, the amount of energy dissipation is subsequently increasing smoothly indicating the occurrence of frictional slippage between all adjacent layers.
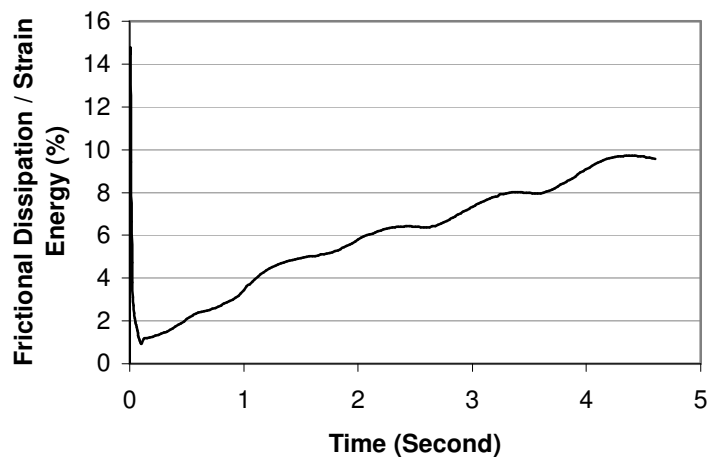
Figure 5.19: Percentage of energy dissipation to the strain energy.

The investigation of cyclic tensile (Figure 5.14), torsional (Figure 5.16) and bending (Figure 5.18) loading reveals the hysteresis effects of unbonded flexible risers. The cyclic behaviour of riser structures is due to slip-stick behaviour in the riser. The area between loading and unloading curves in force-displacement figure is the amount of energy dissipated due to this phenomenon.

6 Numerical Derivation of Constitutive Models

6.1 Introduction

The work outlined in this chapter introduces an 'equivalent elasto-plastic' constitutive law for the beam cross-section to relate axial strain, torsion and bending curvatures to their conjugate stress resultants. Such relationships can be used to model the small-scale frictional slip occurring between the layers, when a combination of values of the stress resultants and internal and external pressures exceed a given threshold, at the macroscopic level of the cross section. To this end, an 'equivalent yield function' is defined, which depends on the current values of the stress resultants, on a set of internal history variables, but also on the values of the external and internal pressures acting on or within the pipe. This last functional relationship simulates the effect that the pressure values have on the inter-layer normal stress, which in turn affects the inter-layer frictional sliding and the overall dissipation. The zero level set of the yield function represents the boundary of a 'no-slip domain', that is the onset of slipping (Alfano *et al.*, 2008; Bahtui *et al.*, 2008c).

In formulating this model a linear kinematic hardening law has been employed. For the case of monotonic loading, the assumptions of linear hardening and of linear elastic behaviour within the 'no-slip domain' result in a bilinear response, which can provide sufficient approximation of the structural response in many cases of interest. This simplified model entails that the single cross section of the riser can be either in a state in which 'no slip' is found, or in a state in which 'full slip' occurs.

The bridging between the beam model, suitable for large-scale analysis of the entire riser, and the small-scale detailed finite element model relies on the identification of the parameters of the beam model which is achieved through a combination of reasonable engineering assumptions and careful curve fitting, using the small-scale detailed finite element model as a virtual testing rig. It is worth observing that the numerical data, on which the constitutive model is calibrated, can also directly originate from experiments if such results are available. However accurate experimental testing of flexible risers

which correctly reproduces the in-service conditions is difficult and very expensive, whereas the availability of a detailed finite element model to minimize the number of required experiments is very important, and its use within the proposed multi-scale method capable of analyzing both short and long risers is expected to have a significant impact on the feasibility, accuracy and economy of the overall design and analysis of flexible pipes.

6.2   Formulation of the constitutive model

In this section the constitutive law of a flexible riser for an Euler-Bernoulli 3D beam model is formulated. It is assumed that locally the pipe develops along a straight line, so that an infinitesimal element of pipe can be represented as in Figure 6.1. A local right-handed Cartesian system is introduced with the origin and the x and y axes located at the cross section and the z axis coincident with the centroid axis.

6.2.1 Generalised stresses and strains

The stress resultants, shown in Figure 6.1, are the axial force N, the torque T, and the bending moments around axes x and y, denoted by M_x and M_y, respectively.
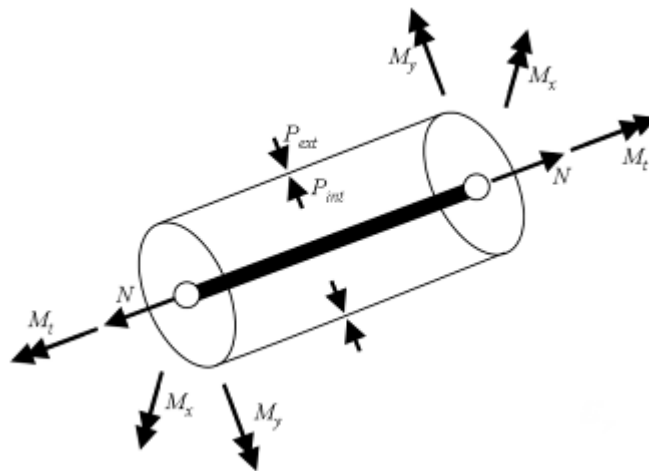
Figure 6.1: Stress resultants.

In addition, the internal and external pressures need to be considered in the model. Referring to the cross-sectional view of the riser in Figure 6.2, the average radial strain ε_r is given by

$$\varepsilon_r = -\frac{t - t_{in}}{t_{in}} \qquad (6.1)$$

where t_{in} and t denote the initial and the current thicknesses of the whole riser, respectively. Notice that the negative sign is added for convenience in the above equation so that the work done by the pressure parameter P_ε, which is introduced later in Equation (6.5), for a positive ε_r is positive.
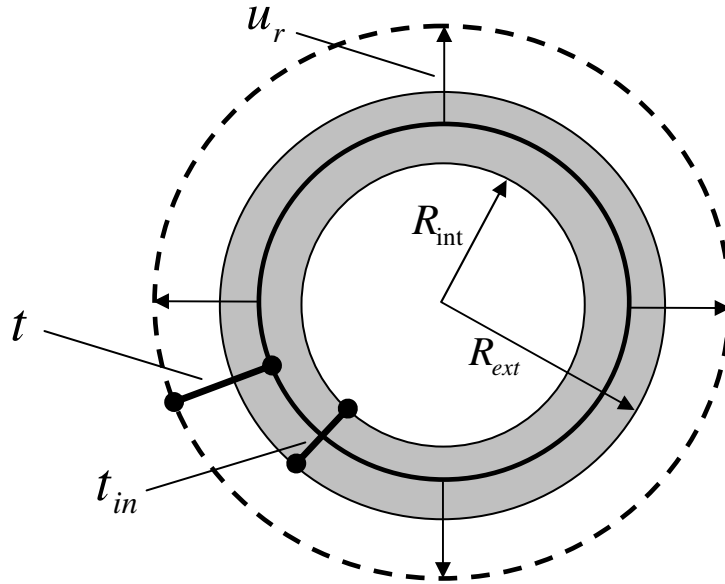
Figure 6.2: Cross view of the riser section.

The radial displacement of the average radius, the radial displacement of the internal layer and the radial displacement of the external layer, indicated with u_r, u_{int} and u_{ext}, respectively, are related to the radial strain and to the current thickness as follows:

$$u_{\text{int}} = u_r + \varepsilon_r \frac{t}{2}$$

$$u_{ext} = u_r - \varepsilon_r \frac{t}{2}$$

(6.2)

The work W done by the pressure per unit of length of the riser is then

$$W = P_{\text{int}} u_{\text{int}} 2\pi R_{\text{int}} - P_{ext} u_{ext} 2\pi R_{ext}$$

(6.3)

where R_{int} and R_{ext} are the internal and external radii, while P_{int} and P_{ext} represent the internal and external applied pressures.

By substituting Equation (6.2) into Equation (6.3) we have:

$$W = P_u u_r + P_\varepsilon \varepsilon_r$$

(6.4)

where P_u and P_ε are the conjugate actions working for u_r and ε_r, defined by:

$$P_u = 2\pi(P_{\text{int}} R_{\text{int}} - P_{ext} R_{ext})$$

$$P_\varepsilon = \pi t (P_{\text{int}} R_{\text{int}} + P_{ext} R_{ext})$$

(6.5)

Increasing values of P_ε result in increasing compressive normal stresses between layers in the radial direction and, therefore, in increasing frictional stresses. Instead, the value of P_u controls the radial displacement and does not affect the radial stresses or the amount of friction.

Hence, in the proposed model N, M_t, M_x, M_y, P_u and P_ε are the generalised stresses. The corresponding work-conjugate generalised strains are $\varepsilon_z, \phi, \chi_x, \chi_y, u_r, \varepsilon_r$, where $\varepsilon_z, \chi_x, \chi_y$ and ϕ are the axial strain, the curvatures about the x and y directions and the torsional curvature, which are in turn related to the axial displacement u_z and the torsional rotation ψ by the following relationships:

$$\varepsilon_z = \frac{du_z}{dz}; \quad \chi_x = -\frac{d^2 u_y}{dz^2}; \quad \chi_y = \frac{d^2 u_x}{dz^2}; \quad \phi = \frac{d\psi}{dz}. \tag{6.6}$$

A compact notation is conveniently introduced denoting by $\underline{\sigma}$ and $\underline{\varepsilon}$ the generalised stresses and strains:

$$\underline{\sigma} = \begin{bmatrix} N \\ M_t \\ M_x \\ M_y \\ P_u \\ P_\varepsilon \end{bmatrix} \qquad \underline{\varepsilon} = \begin{bmatrix} \varepsilon_z \\ \phi \\ \chi_x \\ \chi_y \\ u_r \\ \varepsilon_r \end{bmatrix} \tag{6.7}$$

6.2.2 Constitutive law

As discussed in Section 6.1, the constitutive law for the beam model is based on the observation that the local (small-scale) frictional slip between the different layers results in a macroscopic (large-scale) relationship between generalised stresses and strains which has many analogies with the laws of elasto-plasticity.

Figure 6.3 shows the response of the flexible riser shown in Figure 3.1 under cyclic loading, evaluated using a detailed three-dimensional finite element analysis which accurately models the interaction between all layers. For the qualitative analysis in this section, presented to justify the assumptions of the proposed constitutive model, it is sufficient to state that the values of the applied loading (internal and external pressures included) are within a meaningful range typical of practical cases. For the first monotonic increase of the curvature, the bending moment increases with an almost linear stiffness between points (a) and (b). Then the stiffness rapidly decreases between points (b) and (c) to a value which remains approximately constant up to point (d). Upon unloading, the flexural stiffness is initially very close to the initial
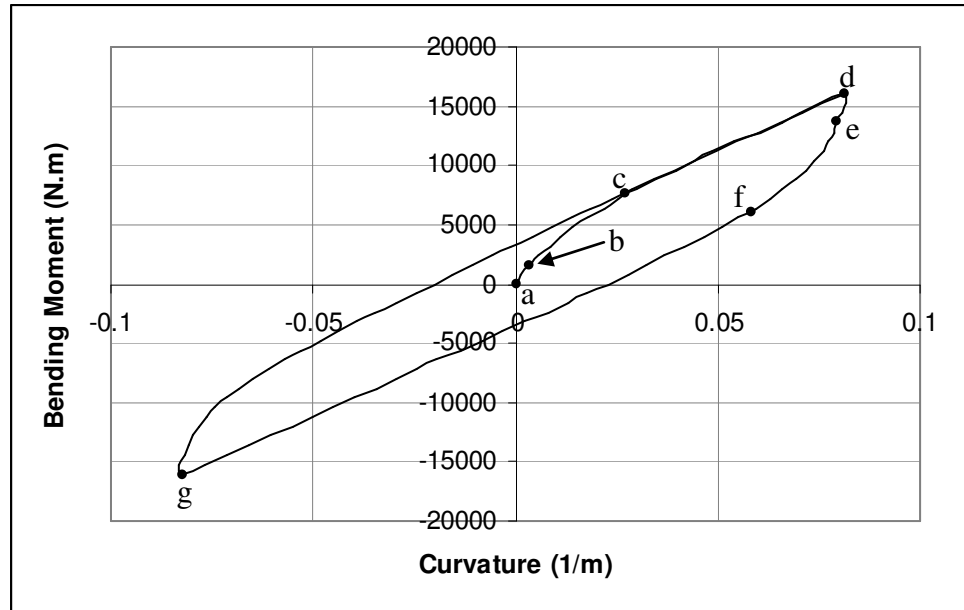
Figure 6.3: Plot of the bending moment against the corresponding curvature
for the unbonded flexible riser of Figure 3.1 during cyclic
loading; the response is evaluated with a detailed finite-element
simulation.

stiffness, between points (d) and (e), and then it rapidly decreases between points (e)
and (f) to a value which is constant between points (f) and (g) and approximately equal
to that between points (c) and (d). Replacing the rounded parts between points (b) and
(c) and between points (e) and (f) with two sharp elbows, a bilinear curve response is
obtained with very good approximation. Such a bilinear curve represents the same type
of response as that obtained using an elasto-plastic model with linear kinematic
hardening, which is the model proposed here.

In analogy with the elasto-plastic case, the generalised strains are additively
decomposed into an elastic-like, i.e. 'no-slip', part $\underline{\varepsilon}_e$, and a plastic-like, i.e. 'full-slip',
part $\underline{\varepsilon}_s$.

$$\underline{\varepsilon} = \underline{\varepsilon}_e + \underline{\varepsilon}_s \qquad (6.8)$$

The generalised stress is obtained from the no-slip components of the generalised strains via a linear-elastic relationship:

$$\underline{\sigma} = \hat{D}\,\underline{\varepsilon}_e \tag{6.9}$$

where $\hat{D}$ indicates the stiffness during the no-slip phase. The full-slip strains evolve in accordance with a law which is analogous to the plastic flow rule of elasto-plasticity, and which can be expressed as follows:

$$\dot{\underline{\varepsilon}}_s = \dot{\lambda}\frac{\partial g}{\partial \underline{\sigma}} \quad , \tag{6.10}$$

where g represents a suitable defined real-valued 'slip potential'. The multiplier $\dot{\lambda}$ evolves in accordance with the Khun-Tucker conditions:

$$\dot{\lambda} \geq 0 \qquad f(\underline{\sigma} - \underline{\beta}) \leq 0 \qquad \dot{\lambda}\,f(\underline{\sigma} - \underline{\beta}) = 0 \tag{6.11}$$

where $\underline{\beta}$ represents the 'back-stress' associated with kinematic hardening.

The real-valued function f represents the equivalent of the yield function in elasto-plasticity and will be indicated as 'slip-onset' function in view of its mechanical meaning in the current context. When the stress resultant $\underline{\sigma}$ is such that $f(\underline{\sigma} - \underline{\beta}) < 0$, then no slip occurs, i.e. the stress resultants are inside the 'no-slip' domain. Instead, when $f(\underline{\sigma} - \underline{\beta}) = 0$, slip can occur because it is possible to have $\dot{\lambda} > 0$.

Notice that it is not possible to have $f(\underline{\sigma} - \underline{\beta}) > 0$. However, the back-stress follows the evolution of the full-slip component $\underline{\varepsilon}_s$ in accordance with a hardening relationship which, in this case, is assumed to be linear:

$$\underline{\beta} = \hat{H}\,\underline{\varepsilon}_s \tag{6.12}$$

where $\hat{H}$ is a matrix of hardening coefficients. Therefore, although the value of the slip-onset function remains constantly zero during the frictional slipping phase, the value of the stress components increase because of the hardening, in accordance with the expected response shown in Figure 6.3.

The slip-onset function f and the potential g have to incorporate the dependency of the response of the flexible pipe cross section on the current state of internal stress. In particular, the values of the pressure component P_ε has a great influence on the normal interaction between layers and then on the onset of friction.

It should be noted that the slip potential g and the slip-onset function f are different because of the frictional nature of the constitutive law. The mechanical meaning of this assumption will be discussed later in more detail.

6.2.3 Finite-step equations

From a computational point of view, the time domain needs to be subdivided into a number of finite steps. Adopting a fully implicit backward-Euler time-integration scheme, the equations to solve in each step are as follows:

$$
\begin{cases}
\underline{\sigma} = \hat{D}\left(\underline{\varepsilon} - \underline{\varepsilon}_s\right) \\
\underline{\varepsilon}_s - \underline{\varepsilon}_{s0} = \Delta\lambda \dfrac{\partial g}{\partial \underline{\sigma}} \\
\underline{\beta} = H\,\underline{\varepsilon}_s \\
\Delta\lambda \geq 0 \quad f\!\left(\underline{\sigma} - \underline{\beta}\right) \leq 0 \quad \Delta\lambda\, f\!\left(\underline{\sigma} - \underline{\beta}\right) = 0
\end{cases}
\tag{6.13}
$$

In a conventional displacement-based finite-element analysis the constitutive law is 'strain driven', whereby the generalised strain $\underline{\varepsilon}$ at the end of the step and the history variables at the beginning of the step, that is $\underline{\varepsilon}_{s0}$ in this case, are given, and the remaining variables at the end of the step, that is the stress $\underline{\sigma}$, the back-stress $\underline{\beta}$ and the full-slip generalised strain $\underline{\varepsilon}_s$ have to be computed. The solution is found iteratively,

using the same well-established return-map algorithms used in elasto-plasticity in which the Newton-Raphson method, presented in Appendix A, is used to solve the non-linear Equation (6.13).

The above equations provide a general formulation which is the basis for the current and future developments of this research work. As will be discussed later in more detail, the main difficulty lies in the identification of the coefficients of the stiffness and hardening matrices $\hat{D}$ and $\hat{H}$, and of both the expression and the related coefficients of functions f and g. Addressing the most general case is not convenient in this phase of the research work in which the main aim is to demonstrate the validity and the potential of the proposed method. Hence, in the following sections some reasonable assumptions will be made to study some cases of significant interest.

6.3 Specialization to the case of cyclic flexural loading

In this section, the very important case of cyclic flexural loading will be considered. To simplify the treatment and better focus on the factors which have a major influence on the structural response, the assumption is made that the axial force N and the torque M_t are constant throughout the deformation process. Hence, their influence on the determination of functions f and g can be incorporated within the coefficients and then ignored. Furthermore, a pure elastic relationship can be assumed between N and M_t and the conjugated variables ε_z and ϕ, so that the hypothesis made that N and M_t are constant allows us to completely ignore these terms.

A further simplifying assumption made is that $P_u = 0$. This seems reasonable in this phase of the work because the main influence on the response of the flexible pipe at the onset of and during frictional slipping is given by the other term P_ε. The latter simplification further reduces the number of degrees of freedom of the model and, because of Equation (6.5)$_1$, it results in the following relationship to be satisfied by the pressure values applied to the (small-scale) detailed finite element model:

$$P_{int} R_{int} = P_{ext} R_{ext} \qquad (6.14)$$

Symmetry of the cross section rules out coupling terms in the elastic relationship between the remaining components of the generalised stresses and strains, and also results in the same flexural response about the x and y axes, whereby the initial stiffness is represented by a diagonal matrix:

$$\begin{bmatrix} M_x \\ M_y \\ P_{\mathcal{E}} \end{bmatrix} = \begin{bmatrix} D_{11} & 0 & 0 \\ 0 & D_{11} & 0 \\ 0 & 0 & D_{33} \end{bmatrix} \begin{bmatrix} \chi_x \\ \chi_y \\ \varepsilon_r \end{bmatrix} \qquad (6.15)$$

The components of the back-stress vector $\underline{\beta}$ which correspond to the generalised-stress components M_x, M_y and $P_{\mathcal{E}}$ are denoted by β_x, β_y and $\beta_{\mathcal{E}}$, so that the argument of the onset-slip function is given by:

$$\underline{\sigma} - \underline{\beta} = \begin{bmatrix} M_x - \beta_x \\ M_y - \beta_y \\ P_{\mathcal{E}} - \beta_{\mathcal{E}} \end{bmatrix} \qquad (6.16)$$

To determine functions f and g and the coefficients of the kinematic hardening matrix, many results of several numerical simulations made with the detailed finite element model have been reviewed and the following expression has been found to be sufficiently valid:

$$f(\underline{\sigma} - \underline{\beta}) = b\left[(M_x - \beta_x)^2 + (M_y - \beta_y)^2\right] - (P_{\mathcal{E}} - \beta_{\mathcal{E}}) - a \qquad (6.17)$$

where a and b are material parameters to be identified, and again symmetry of the cross section has been exploited.

The slip potential g has to account for the finding that frictional slipping in bending is not accompanied by any significant relative opening between layers. At the small-scale level this means that no significant dilatancy is observed in the frictional slipping

between layers. A suitable expression for the potential g which meets this requirement is as follows:

$$g\left(\underline{\sigma} - \underline{\beta}\right) = b\left[\left(M_x - \beta_x\right)^2 + \left(M_y - \beta_y\right)^2\right]$$

(6.18)

which results in the following slip rule:

$$\underline{\dot{\varepsilon}}_s = \dot{\lambda}\frac{\partial g}{\partial \underline{\sigma}} \quad \Rightarrow \quad \begin{bmatrix} \dot{\chi}_{sx} \\ \dot{\chi}_{sy} \\ \dot{\varepsilon}_{sr} \end{bmatrix} = \dot{\lambda}\begin{bmatrix} \dfrac{\partial g}{\partial M_x} \\ \dfrac{\partial g}{\partial M_y} \\ \dfrac{\partial g}{\partial P_\varepsilon} \end{bmatrix} = \dot{\lambda}\begin{bmatrix} 2bM_x \\ 2bM_y \\ 0 \end{bmatrix}$$

(6.19)

where $\dot{\chi}_{sx}$, $\dot{\chi}_{sy}$ and $\dot{\varepsilon}_{sr}$ denote the full-slip components of the bending curvatures about the x and y axes and of the radial strain. Overlapping the generalised stresses and strains spaces, Figure 6.4 describes the above equation and shows that the inequality between functions f and g results in the full-slip strain rate $\dot{\underline{\varepsilon}}_s$ being not normal to the slip-onset surface, i.e. not parallel to the normal $\underline{n}$. This is in analogy with the non-associative plasticity models used for many materials exhibiting internal friction for which the normality rule is not satisfied.
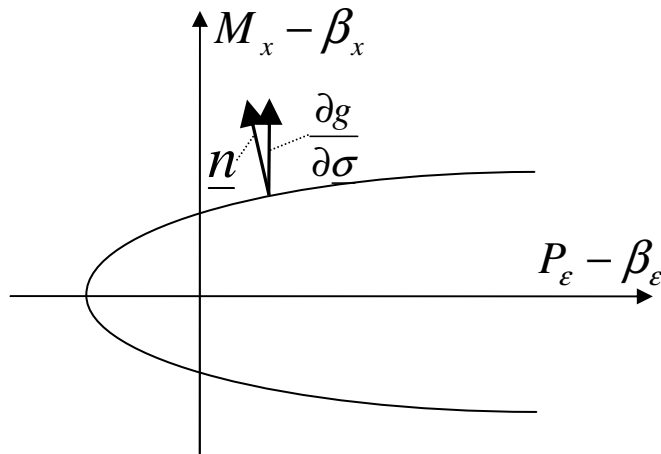

Figure 6.4: Non-associative behaviour of the proposed model.

The following proportional hardening law is used:

$$\underline{\beta} = \hat{H}\,\underline{\varepsilon}_s = h\,\underline{\varepsilon}_s \qquad \Rightarrow \qquad \begin{bmatrix} \beta_x \\ \beta_y \\ \beta_\varepsilon \end{bmatrix} = h \begin{bmatrix} \chi_{sx} \\ \chi_{sy} \\ \varepsilon_{sr} \end{bmatrix} \qquad (6.20)$$

It is worth observing that because of the slip law in Equation (6.19), the radial full-slip strain ε_{sr} results to be constantly zero, so that β_ε also becomes zero and the above equation further changes to:

$$\begin{bmatrix} \beta_x \\ \beta_y \\ \beta_\varepsilon \end{bmatrix} = \begin{bmatrix} h\,\chi_{sx} \\ h\,\chi_{sy} \\ 0 \end{bmatrix} \qquad (6.21)$$

It should be noted that when the model is symmetric about the x and y axes, a simple plane model can be used to study the structural response and to identify the model parameters as will be shown in Sections 6.3.1 to 6.3.3. The above equations were, nonetheless, derived in their full three dimensional sense in order to demonstrate its applicability for the general case when all the moments and curvatures about both axes are present.

6.3.1   Finite element simulation

Several finite element simulations for a typical 1.7m long unbonded flexible riser have been conducted using the finite element code ABAQUS. The model includes a complex make up of seven-layers of internal and external plastic sheaths, helical armours, carcass and anti-wear layers and is described in the cross-sectional view of Figure 6.5. It has been created by adding one additional layer to the model considered in Chapter 3 and replacing thin shell type element by linear brick type element for carcass layer. Figure 6.6 shows the finite element mesh of the riser and indicates the number of nodes and elements used. All boundary conditions are the same as those in Section 3.9. Other details of the riser are also the same as those in Chapter 3.

For the identification of the parameters, it was sufficient to consider the planar case in which moments are applied about the *x* axis in Figure 6.5. Accordingly, the only non-zero flexural curvature is also about the same axis.

The analysis starts with an initial 'pressure load step' which accounts for the internal fluid pressure and the external hydrostatic pressure. Four different input pressures are analysed and referred to as cases 1, 2, 3, and 4, respectively. The values of the applied internal and external pressures are given in Table 6.1 and satisfy Equation (6.14).
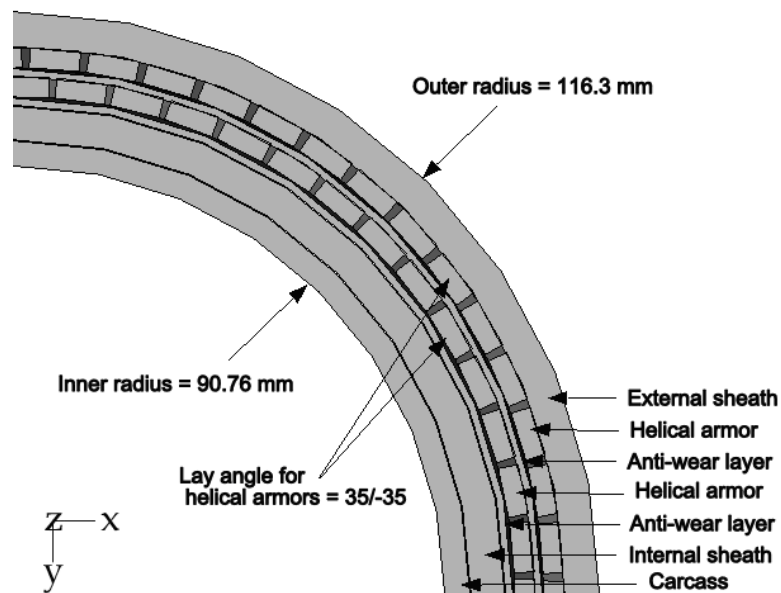

Figure 6.5: Detailed geometry of riser (cross-sectional view).

The pressure step is then followed by a 'bending step', in which a 16 kNm bending moment is cyclically applied to the free end of the pipe. In each loading or unloading part of the cycles the moment is applied linearly with time.
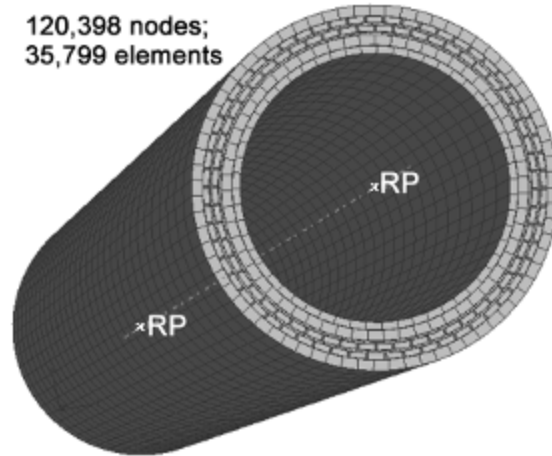
Figure 6.6: Finite-element mesh.

For each case analysed, an average curvature of the riser has been computed at each increment by dividing the rotation of the free end of the riser about the x axis by the length of the riser. In Figure 6.7 the applied bending moment is plotted against the computed average curvature for the four different load cases. It should be noted that the initial pressure load step does not result in any curvature. As expected, results are similar to those in Figure 6.3.

Table 6.1: Load cases – steps and magnitudes.

Load Case	Loads applied to riser			
	Pressure Loading (MPa)	P_ε (kN)	Max. bending moment (kNm)	Min. bending moment (kNm)
1	Internal = 0 External = 0	0	16	-16
2	Internal = 10 External = 7.804	145.6	16	-16
3	Internal = 30 External = 23.41	436.9	16	-16
4	Internal = 50 External = 39.02	728.2	16	-16

Case 1

Pε = 0

(a)

Case 2

Pε = 145.6 kN

(b)

Case 3

Pε = 436.9 kN

(c)
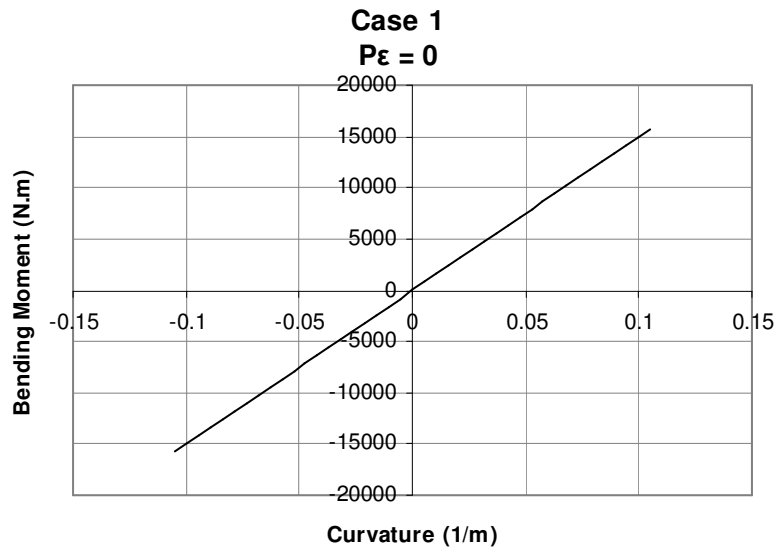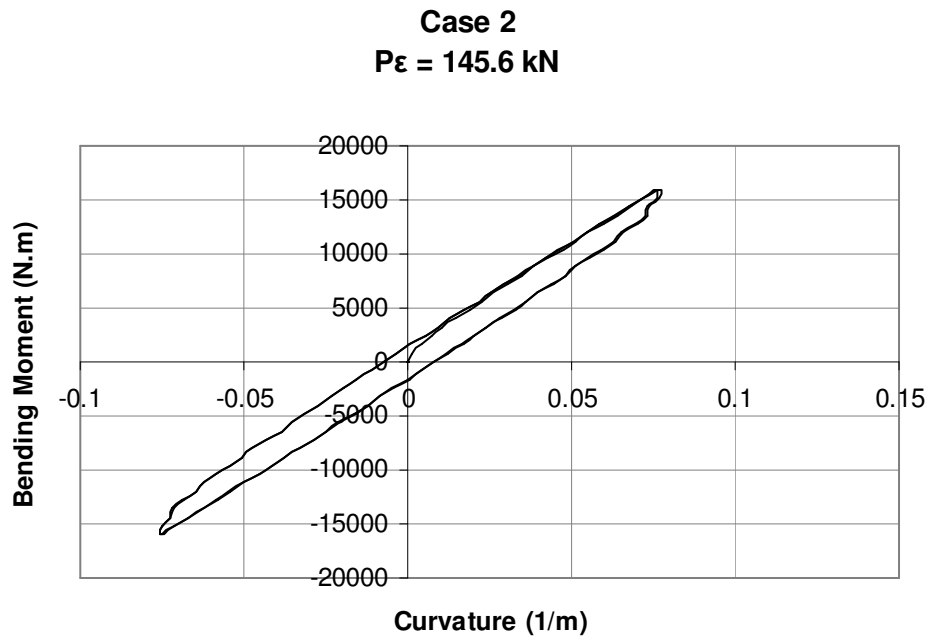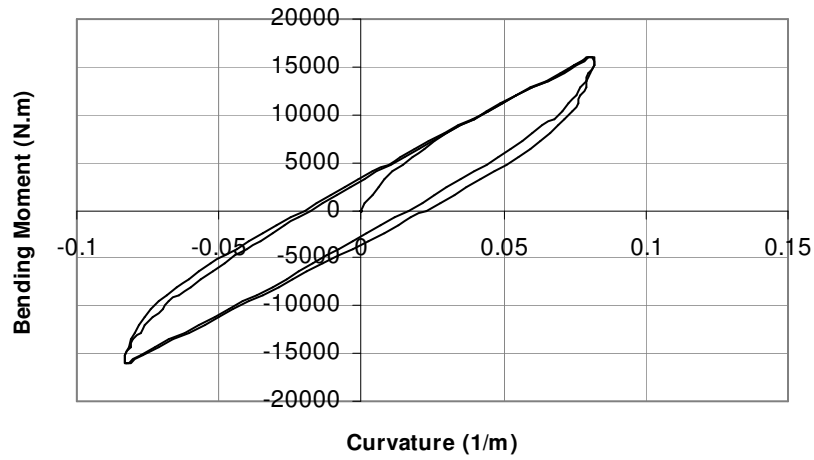
Case 4
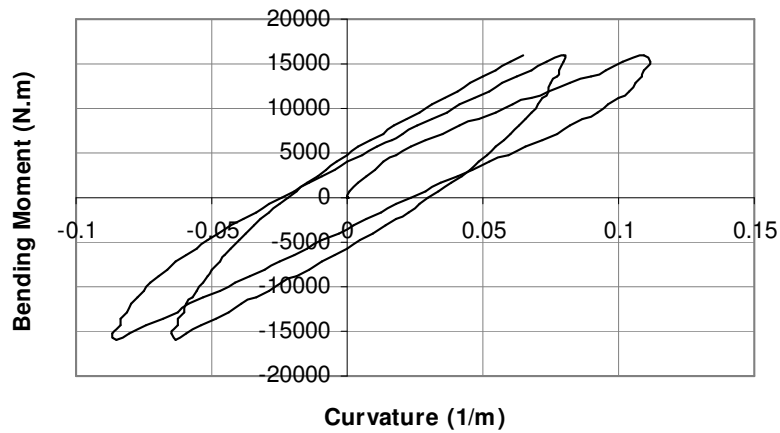
Pε = 728.2 kN

(d)

Figure 6.7: Bending moment-curvature curves for the four different load cases (a) P_ε = 0, (b) P_ε = 145.6 kN, (c) P_ε = 436.9 kN and (d) P_ε = 728.2 kN.

All results of Figure 6.7, except for the case $P_\varepsilon = 0$, illustrate a hysteretic behaviour of the riser subjected to cyclic bending moment. The response tends towards a stabilised cyclic response gradually as the number of cycles increase. The first cycle represents the

installation phase, whereas the stabilised results are more suitable to be used for the calibration procedure, which will be discussed in the next section. Figure 6.7 also shows that the higher the pressure, the more cycles are needed to reach a stabilised hysteresis loop, and the greater the energy dissipated during the hysteresis loop.

6.3.2 Calibration of the constitutive model

Several finite element simulations have been used to calibrate the constitutive model. Each bending moment-curvature result from the numerical simulations was curve fitted using a bilinear curve, using the stabilised cycle. This bilinear curve can give three specific parameters for the constitutive model: the initial no-slip slope, a slip-initiation point, and a full-slip slope. In Figure 6.8 two representative results from the finite element simulations are shown together with the fitted bi-linear curves.

(a)

Pε = 436.9 kN
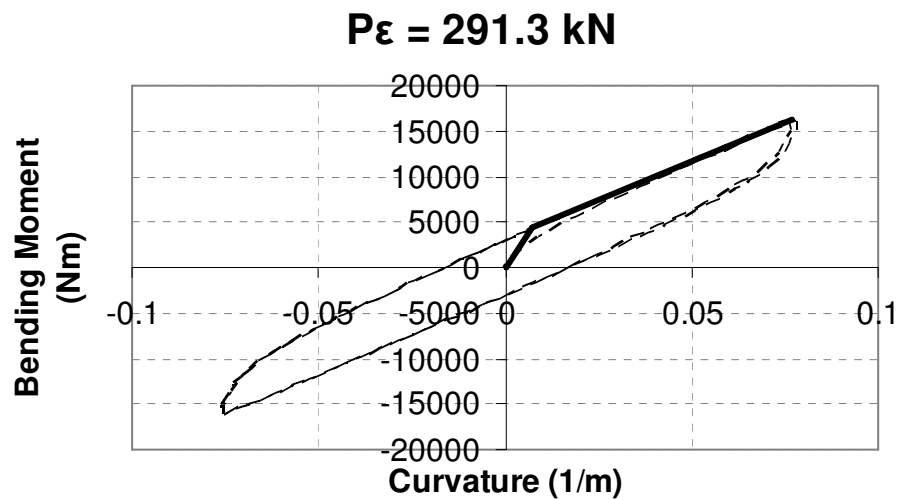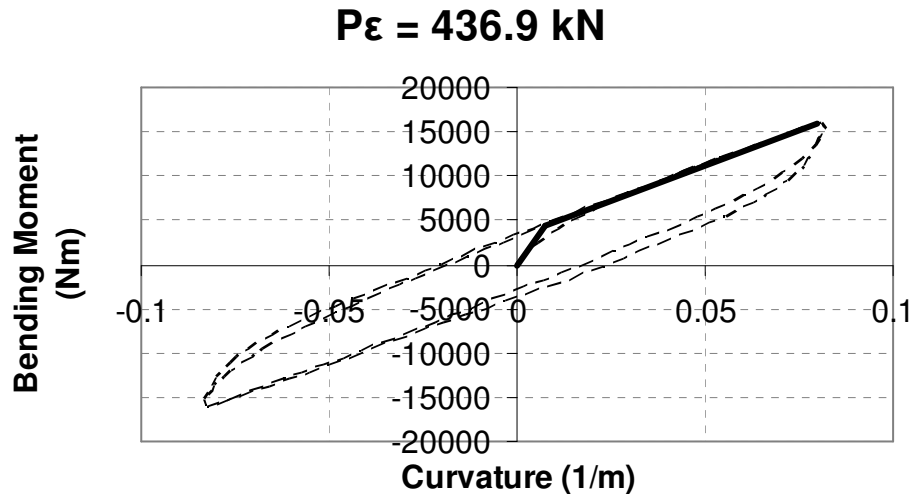
(b)

Figure 6.8: Two representative results from the finite element simulations and
related fitted bilinear curves.

For all cases except those with zero or very small applied pressure, an initial linear response can be identified. Therefore, an initial 'no-slip slope' can be determined and is found to be the same for each of the analysed cases. This validates the hypothesis that an initial linear part of the moment-curvature diagram, in which frictional slip between layers is absent or negligible, does exist. This slope directly provides the flexural stiffness $D_{11} = D_{22}$.

After this initial linear response, a non-linear part of the curve follows, which relatively rapidly tends to join a final full-slip slope. Upon repeated loading and unloading cycles, this final slope changes and stabilizes on a straight line which is that used in the identification procedure. This final full-slip slope is not equal to the hardening parameter h, but it is related to it and therefore its determination allows to estimate h.

The intersection point between the initial slope and the final slope provides a 'slip-initiation' point, which is also a point of the boundary of the no-slip domain, i.e. a point of the zero level set of the slip-onset function. The slip-initiation points identified have been fitted with the quadratic expression of Equation (6.17) and the resulting curve is shown in Figure 6.9.
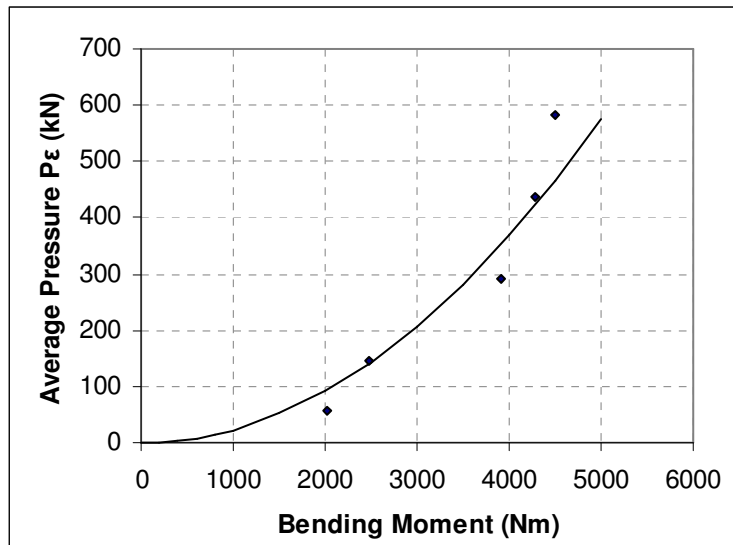
Figure 6.9: Curve-fitting of the slip-initiation points.

Finally, the last parameter of the model to be identified is the stiffness value D_{33}. This has been done by analyzing the pressure steps in the above described analyses for different values of the pressure, and identifying the initial no-slip, nearly linear response. Table 6.2 reports the parameters of the model determined with the proposed procedure:

Table 6.2: Identified parameters.

Stiffness		Slip-onset function		Hardening
D_{11} (kNm^2)	D_{33} (kN)	a	b (N^{-1} m^{-2})	h (Nm^2)
608	26707	0	0.023	$2.5 \cdot 10^5$

6.3.3 Validation of the constitutive model

To demonstrate the validity of the proposed method, the same cyclic analyses performed using the detailed finite-element model in ABAQUS have been reproduced using the simplified proposed constitutive model adopting the parameters of Table 6.2

Case 1
Pε = 0

(a)

Case 2
Pε = 145.6 kN

(b)

Case 3
Pε = 436.9 kN

(c)
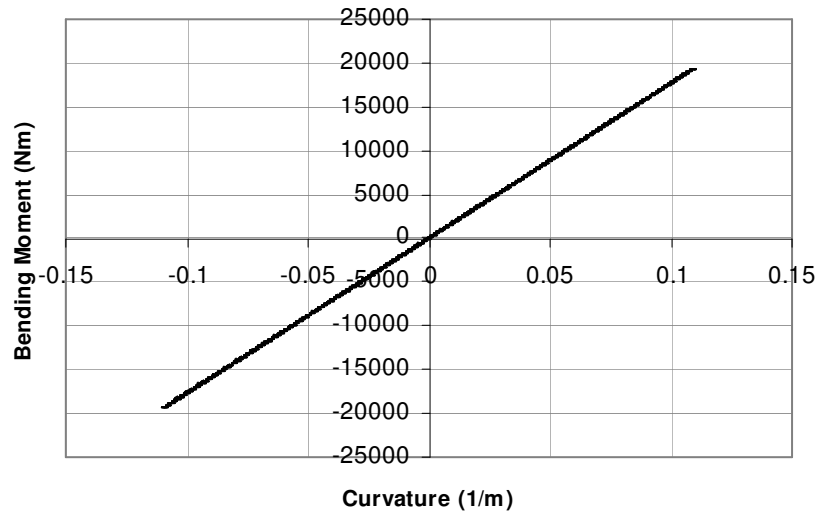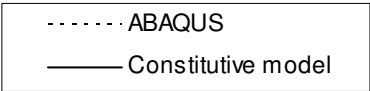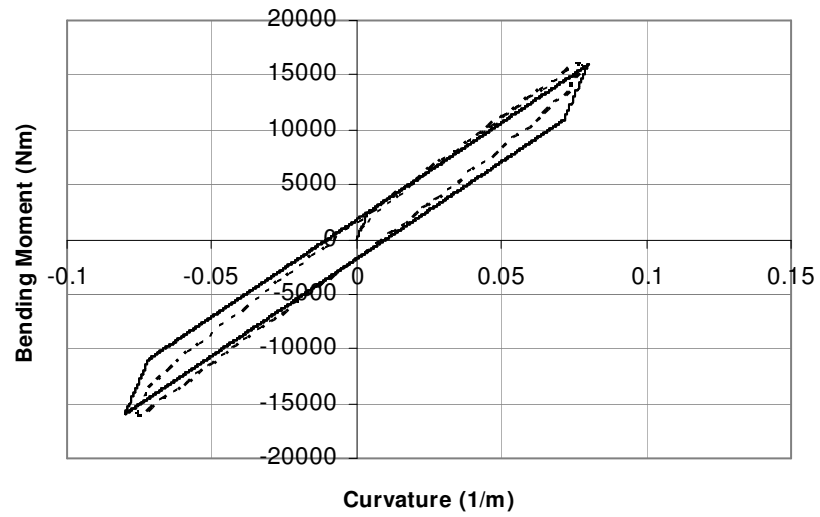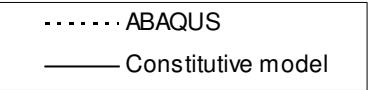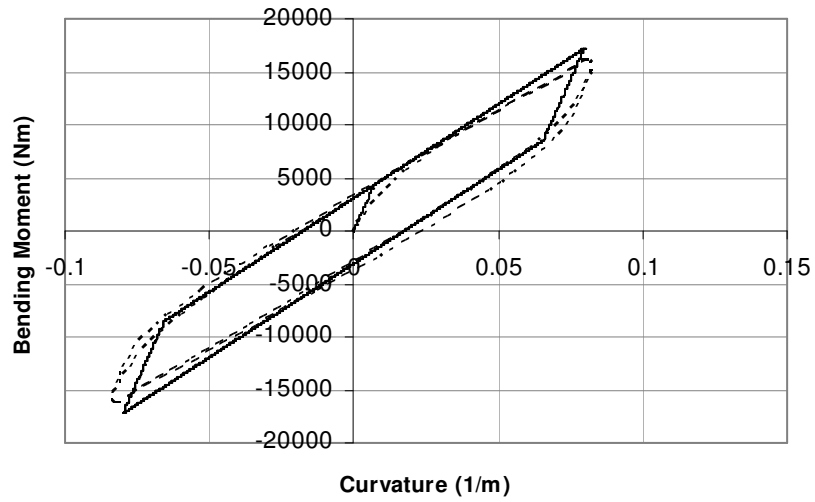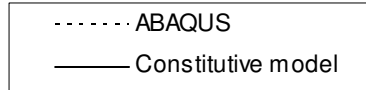
Case 4
Pε = 728.2 kN
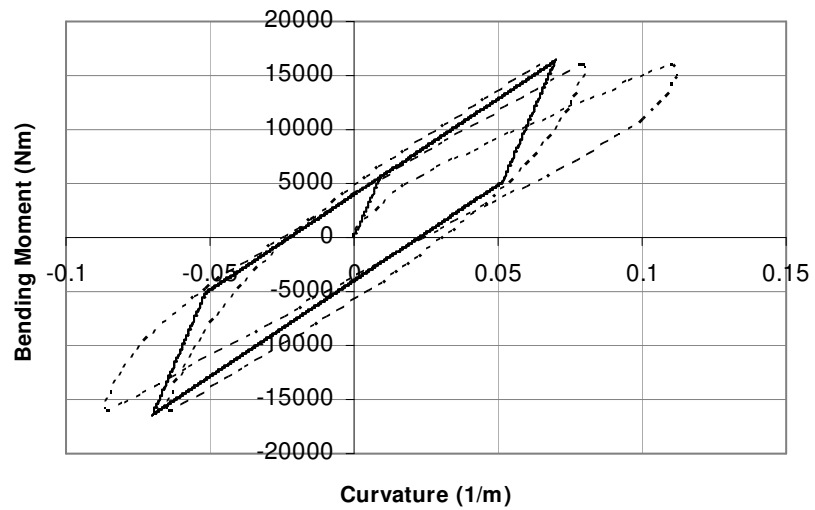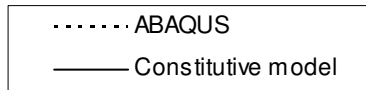
(d)

Figure 6.10: Comparison of the results obtained from the constitutive model (solid line) and from the detailed finite element model (dashed line).

which were identified as described in the previous section, and using the solution scheme described in Section 6.2.3.

Results of this validation are reported in Figure 6.10 for four cases corresponding to four values of the applied pressure load P_ε. For each case a graph is reported in which the moment-curvature curve obtained with the proposed constitutive model is plotted with a solid line and is compared with the dashed-line curve obtained using the detailed finite-element model.

In Case 1 ($P_\varepsilon = 0$), no friction occurs in both cases, which results in no hysteresis, i.e. no energy dissipation. The two curves overlap and cannot really be distinguished. Such perfect agreement is not obtained for the other cases, because the proposed model immediately provides the final stabilised cycle, whereas in the finite-element results one, two and three cycles are required to reach the nearly stabilised response, respectively. The difference between the stabilised response and that in the first one or two cycles increases with increasing values of P_ε, and could be an issue of concern only in the analysis of the installation phase, while in the other cases it can be considered not important for the accuracy of the analysis.

6.4 Specialization to the case of cyclic loading without torsion

In this section, the constitutive law is significantly enhanced by considering the very important case of cyclic axial loading and its coupling effect on the slip-onset function. The number of degrees of freedom of the constitutive model is increased to five by incorporating axial strain, curvatures, radial displacement and the average radial strain ε_r as generalised strains.

The same reasonable assumption made by the authors (Alfano *et al.*, 2008) that the torque M_t is constant throughout the deformation process is retained here to better focus on the factors which have a major influence on the structural response. Hence, its influence on the determination of functions f and g can be incorporated within the coefficients and then ignored. As in Section 6.3, a linear elastic relationship is assumed

between M_t and the conjugated variable ϕ, so that using the hypothesis that M_t is constant allows us to completely ignore this term.

A linear elastic relationship is also assumed between P_u and the conjugate variable u_r. On the other hand, the main influence on the response of the flexible pipe at the onset and during frictional slip is given by the other term P_ε. By including its corresponding work-conjugate generalised strains ε_r as a degree of freedom in the constitutive model, it allows better modelling of the coupling effects between P_ε and N. This improvement to the constitutive model presented in Section 6.3 (Alfano et al., 2008) allows us to consider the coupling terms between the axial and radial strains. As for the coupling effects between the axial strain and the curvature, they are due to the changes in the radial contact stresses between layers caused by changes in the axial force because of Poisson effects, which in turn affects friction. Hence, these effects are embedded into the slip-onset function, and thus are not considered in the stiffness matrix. Instead, no elastic coupling exists between these variables and between radial displacement and the curvature, which results in zero values of the corresponding terms in the stiffness matrix. Finally, symmetry of the cross section results in the same flexural response about the x and y axes, with no elastic coupling between the two curvatures as well as between the curvatures and the axial strain. Hence, the initial stiffness is represented by:

$$
\begin{bmatrix} N \\ M_x \\ M_y \\ P_u \\ P_\varepsilon \end{bmatrix} = \begin{bmatrix} D_{11} & 0 & 0 & D_{41} & D_{51} \\ & D_{22} & 0 & 0 & 0 \\ & & D_{22} & 0 & 0 \\ & sym. & & D_{44} & D_{54} \\ & & & & D_{55} \end{bmatrix} \begin{bmatrix} \varepsilon_z \\ \chi_x \\ \chi_y \\ u_r \\ \varepsilon_r \end{bmatrix}
\tag{6.22}
$$

Note that coupling exists between axial generalised strain and radial strain and displacement terms.

The components of the back-stress vector $\underline{\beta}$ which correspond to the generalised-stress components N, M_x, M_y, P_u and P_ε are denoted by β_z, β_x, β_y, β_r and β_ε, so that the argument of the slip-onset function is given by:

$$\underline{\sigma} - \underline{\beta} = \begin{bmatrix} N - \beta_z \\ M_x - \beta_x \\ M_y - \beta_y \\ P_u - \beta_r \\ P_\varepsilon - \beta_\varepsilon \end{bmatrix} \qquad (6.23)$$

To determine functions f and g and the coefficients of the kinematic hardening matrix, many results from several numerical simulations made with the detailed finite element model have been reviewed and the following expression has been found to be sufficiently valid:

$$f(\underline{\sigma} - \underline{\beta}) = \begin{cases} b(N - \beta_z)^2 + c\left[(M_x - \beta_x)^2 + (M_y - \beta_y)^2\right] - (P_\varepsilon - \beta_\varepsilon) - a, & N - \beta_z > 0 \\ -(N - \beta_z) - a, & N - \beta_z \le 0 \end{cases} \qquad (6.24)$$

where a, b and c are material parameters to be identified, and symmetry of the cross section has been exploited. The slip-onset surface in this case has two surfaces. This is due to the fact that the riser is not assumed to be capable of tolerating axial compression. This indicates that axial force is non-negative.

A suitable expression for the potential g is as follows:

$$g(\underline{\sigma} - \underline{\beta}) = \begin{cases} b(N - \beta_z)^2 + c\left[(M_x - \beta_x)^2 + (M_y - \beta_y)^2\right], & N - \beta_z > 0 \\ -(N - \beta_z), & N - \beta_z \le 0 \end{cases} \qquad (6.25)$$

which results in the following slip rule:

$$\dot{\underline{\varepsilon}}_s = \dot{\lambda}\frac{\partial g}{\partial \underline{\sigma}} = \dot{\lambda}\,\underline{m} \quad \Rightarrow \quad \begin{bmatrix} \dot{\varepsilon}_{sz} \\ \dot{\chi}_{sx} \\ \dot{\chi}_{sy} \\ \dot{u}_{sr} \\ \dot{\varepsilon}_{sr} \end{bmatrix} = \dot{\lambda} \begin{bmatrix} \dfrac{\partial g}{\partial N} \\[4pt] \dfrac{\partial g}{\partial M_x} \\[4pt] \dfrac{\partial g}{\partial M_y} \\[4pt] \dfrac{\partial g}{\partial P_u} \\[4pt] \dfrac{\partial g}{\partial P_\varepsilon} \end{bmatrix}$$

$$= \begin{cases} \dot{\lambda} \begin{bmatrix} 2bN \\ 2cM_x \\ 2cM_y \\ 0 \\ 0 \end{bmatrix}, & (N - \beta_z) > 0 \\[40pt] \dot{\lambda} \begin{bmatrix} -1 \\ 0 \\ 0 \\ 0 \\ 0 \end{bmatrix}, & (N - \beta_z) \le 0 \end{cases}$$

(6.26)

where $\dot{\varepsilon}_{sz}$, $\dot{\chi}_{sx}$, $\dot{\chi}_{sy}$, $\dot{u}_{sr}$ and $\dot{\varepsilon}_{sr}$ denote the full-slip components of the axial tension, the bending curvatures about the *x* and *y* axes, the radial deformation and of the radial strain. Overlapping the generalised stresses and strains spaces, Figure 6.11 describes two cross-sectional views (a,b) as well as a 3D view (c) of the above 3D equation and shows that the difference between functions *f* and *g* results in the full-slip strain rate $\dot{\varepsilon}_s$ being not normal to the slip-onset surface (a,b), i.e. not parallel to the normal $\underline{n}$.

(a)   (b)

(c)
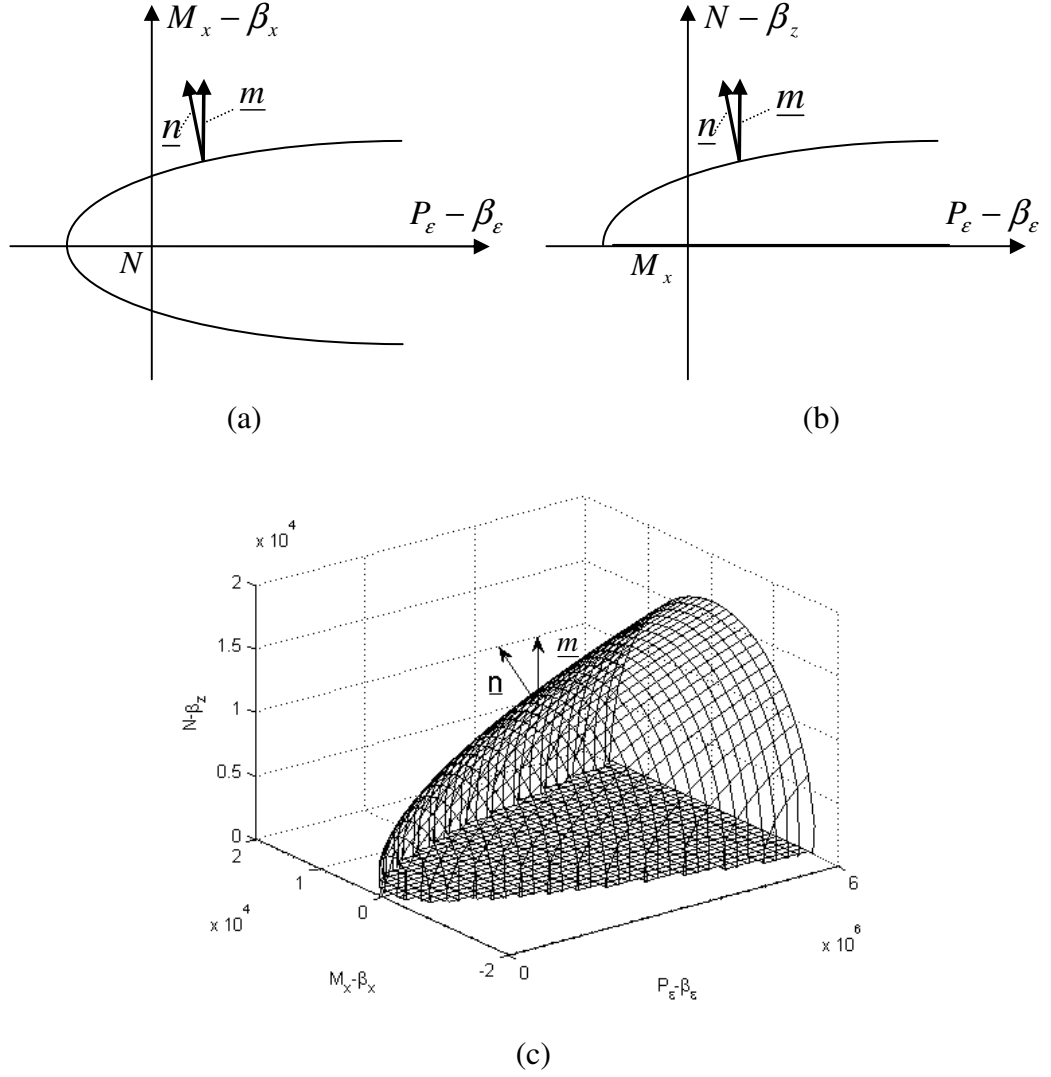
Figure 6.11: Non-associative behaviour of the proposed model.

The following proportional hardening law is used:

$$\underline{\beta} = \hat{H}\,\underline{\varepsilon}_s \quad \Rightarrow \quad \begin{bmatrix} \beta_z \\ \beta_x \\ \beta_y \\ \beta_r \\ \beta_\varepsilon \end{bmatrix} = \begin{bmatrix} H_{11} & 0 & 0 & 0 & 0 \\ & H_{22} & 0 & 0 & 0 \\ & & H_{22} & 0 & 0 \\ & sym. & & 0 & 0 \\ & & & & 0 \end{bmatrix} \begin{bmatrix} \varepsilon_{sz} \\ \chi_{sx} \\ \chi_{sy} \\ u_{sr} \\ \varepsilon_{sr} \end{bmatrix} \tag{6.27}$$

It is worth observing that because of the slip law in Equation (6.26), the radial full-slip strains u_{sr} and ε_{sr} result to be constantly zero, so that β_r and β_ε also remain as zero.

96

6.4.1 Finite element simulation

Several finite element simulations for a typical 1.7 m long unbonded flexible riser, presented in Section 6.3.1, have been conducted using the finite element code ABAQUS to estimate the parameters of the constitutive law for the beam model. The finite element model and all boundary conditions are the same as those presented in Section 6.3.1.

For the identification of the parameters and constructing the constitutive model, six sets of analyses are performed. These are summarised in Table 6.3. The first column shows the number of each sets of analysis.

The second column indicates whether the analysis is performed for several different values of input pressures P_ε, referring to each one as an individual 'load case'. In these analyses (5 and 6) the simulation initiates with an initial 'pressure load step' which accounts for the average pressures P_ε. The pressure step is then followed by the load(s) from column three. The different considered values of P_ε for each axial load case are reported in Table 6.4.

The third column, 'Loadings', shows the type of load which is applied at each analysis. The fourth column determines the additional boundary conditions required for derivation of a target parameter, applied at TRP. The fifth column shows Equation (6.22) specialised to the case once the boundary condition has been applied. The sixth column shows the unknown target parameters which are to be found through each analysis.

In cases 1 to 3, 5 and 6, the cyclic loading response is considered whilst case 4 deals with the monotonic loading response of the riser. The details of the maximum and minimum values of the loads in column 3 of Table 6.3 are reported in Table 6.5.

Table 6.3: Detailed information about individual analyses.

No.	Dependency on P_ε	Loadings[*]	BC at the TRP	Equation to be solved	Target Parameter(s)
1	---	Only P_ε	$\varepsilon_z = 0,$ $u_r = 0$	$D_{55}\varepsilon_r = P_\varepsilon, D_{51}\varepsilon_r = N$	D_{55}, D_{51}
2	---	Only P_ε	Free	$D_{45}u_r = P_\varepsilon - D_{55}\varepsilon_r - D_{15}\varepsilon_z$	D_{45}
3	---	Only P_ε	$\varepsilon_z = 0$	$D_{41}u_r = N - D_{51}\varepsilon_r$	D_{41}
4	No	Only P_u	Free	$D_{44}u_r = P_u - D_{14}\varepsilon_z - D_{54}\varepsilon_r$	D_{44}
5	Yes[**]	N	Free	$D_{11}\varepsilon_z = N - D_{51}\varepsilon_r - D_{41}u_r$	D_{11}, H_{11}, a, b, c
6	Yes	M_x	Free	$D_{22}\chi_x = M_x$	D_{22}, H_{22}, a, b, c

(*) Maximum and minimum values are given in Table 6.5.

(**) Values of P_ε considered are given in Table 6.4.

Table 6.4: Load cases – steps and magnitudes.

Load Case	Loads applied to riser			
	Pressure Loading (MPa)	P_ε (kN)	Max. axial tension (kN)	Min. axial tension (kN)
1	Internal = 0 External = 0	0	100	-100
2	Internal = 10 External = 7.80	145.6	100	-100
3	Internal = 20 External = 15.61	291.3	100	-100
4	Internal = 30 External = 23.412	436.9	100	-100

Table 6.5: Maximum values or semi-amplitudes of the applied loads.

Analysis	1	2	3	4	5	6
Loading	P_ε	P_ε	P_ε	P_u	N	M_x
Units	kN	kN	kN	MN/m	kN	kNm
Minimum	0	0	0	0	0	-16
Maximum	873.9	873.9	873.9	10	100	16
Amplitude	873.9	873.9	873.9	10	100	32

In analysis 1, the average radius of the riser is restricted to move in the radial direction by fixing the inner surface of the outer anti-wear layer, in the radial direction. This is because the inner radius of the outer anti-wear layer coincides with the average radius of the riser excluding the carcass layer. Meanwhile fixing the outer anti-wear layer allows the two adjacent helical armour layers to move freely, so that all layers can be compressed radially. Figure 6.12 shows the applied P_ε against the computed radial strain.

In the second analysis the load is the same as in the first one except the boundary conditions at the TRP, which is not free. Figure 6.13 shows the applied P_ε against the radial displacement.
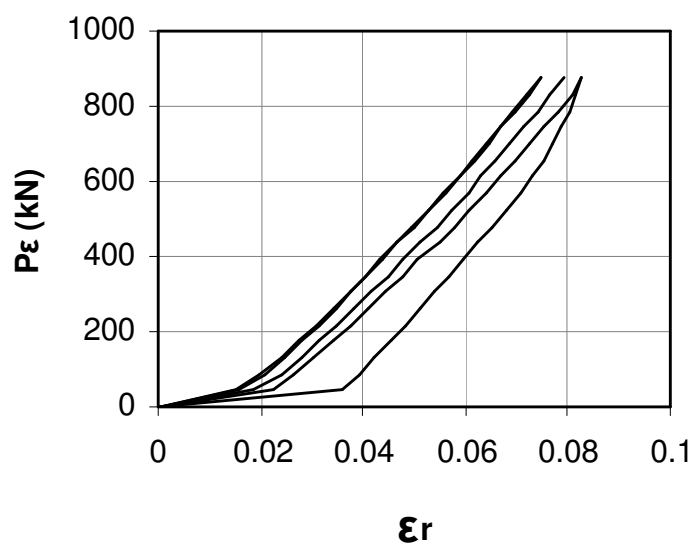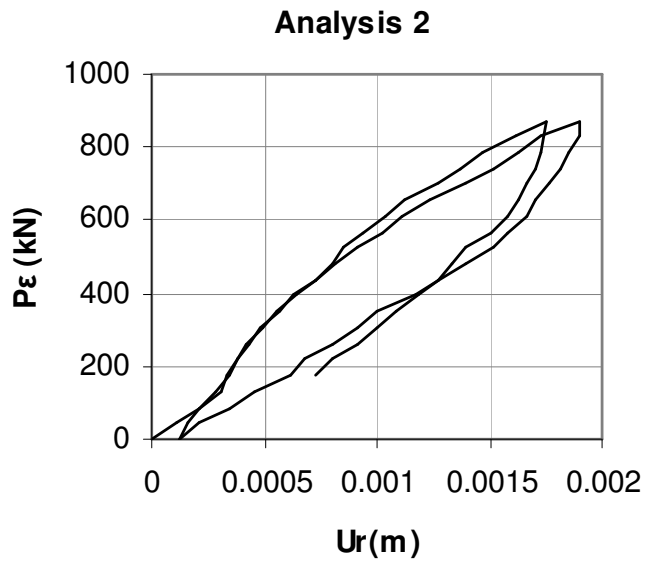

Figure 6.12: Result of analysis 1.

Figure 6.13: Result of analysis 2.

Analysis 3 is again the same as the first two ones except the boundary conditions at the TRP, where displacement is restrained in the axial direction. Figure 6.14 shows the applied P_ε against the computed radial displacement.
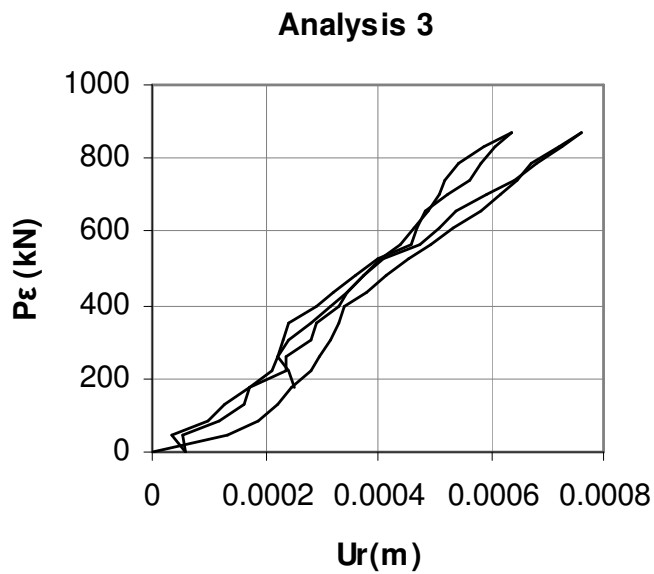
Figure 6.14: Result of analysis 3.
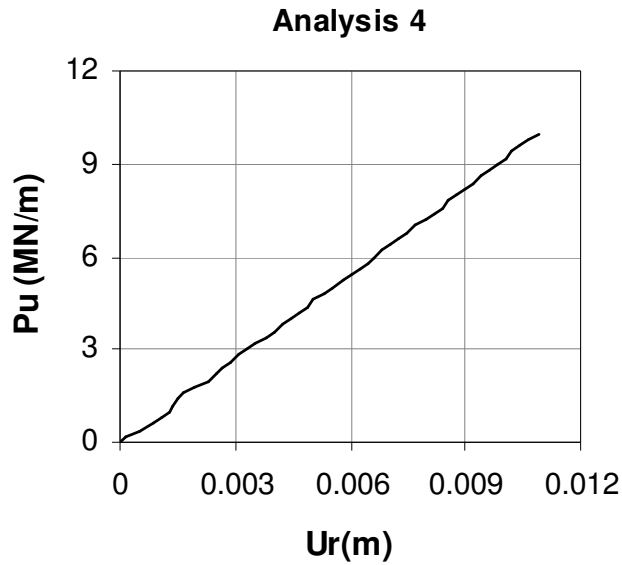
Analysis 4

Figure 6.15: Result of analysis 4.

In the fourth analysis the riser is subject to pure monotonic increase in P_u linearly with time. The TRP is free to move in all directions. Figure 6.15 shows the applied P_u against the computed radial displacement.

The fifth analysis corresponds to a cyclic axial tensile load simulation preceded by an initial 'pressure load step'. The analysis starts with an initial 'pressure load step' which accounts for the internal fluid pressure and the external hydrostatic pressure. Four different input pressures are analysed and referred to as cases 1, 2, 3, and 4, respectively. The values of the applied internal and external pressures are given in Table 6.4. The pressure step is then followed by a 'tensile step', in which a 100 kN axial tension is cyclically applied to the free end of the pipe. In each loading or unloading phase of the cycles the load is applied linearly with time.

In Figure 6.16.a-d the applied axial force is plotted against the computed axial strain for the four different load cases defined in Table 6.4. Notice that the initial pressure load step results in an initial axial strain, radial strain and radial displacement offset which are not shown in the figures.

Analysis 5 - Case 1: Pε = 0

(a)

Analysis 5 - Case 2: Pε = 145.6 kN

(b)

Analysis 5 - Case 3: Pε = 291.3 kN

(c)

Analysis 5 - Case 4: Pε = 436.9 kN

(d)
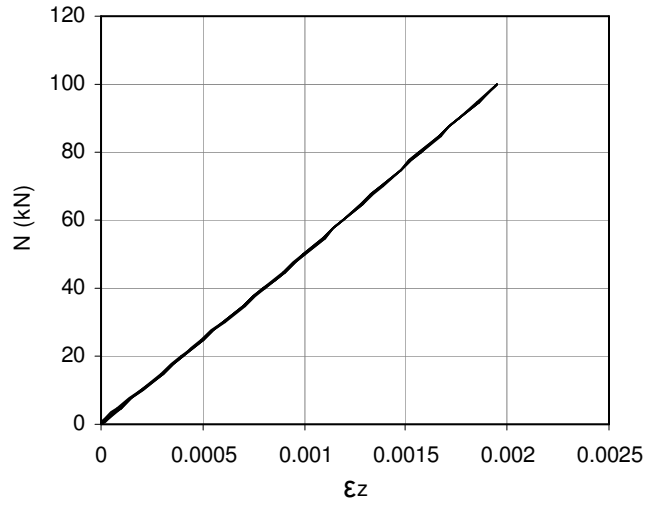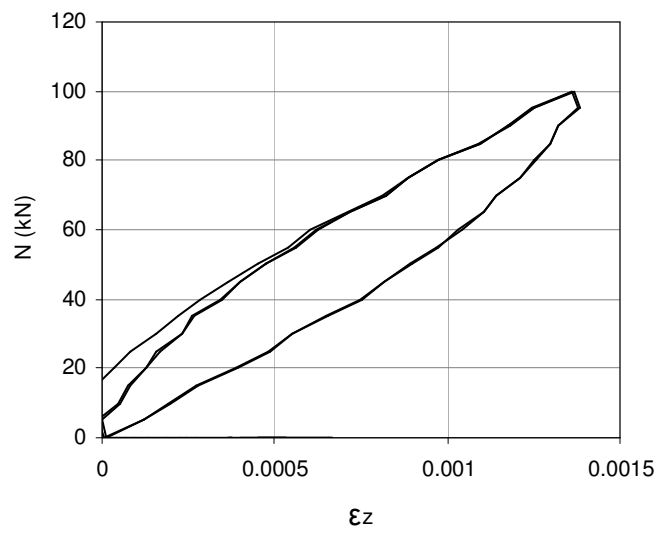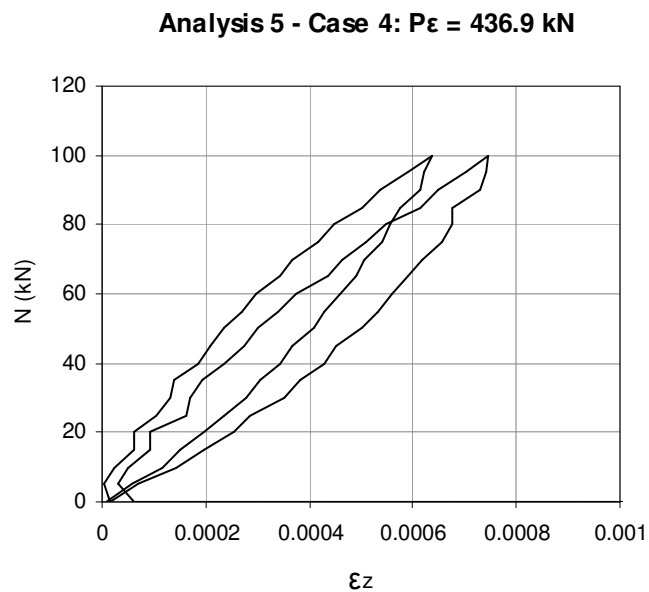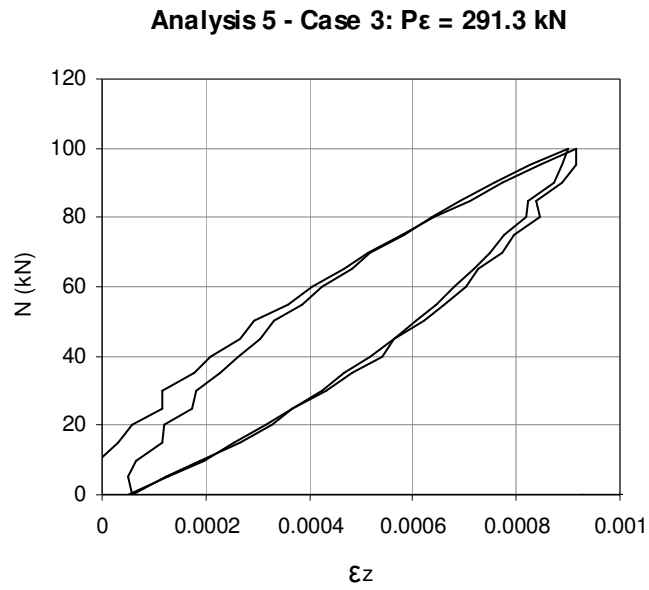
Figure 6.16: Axial force-axial strain curves for the four different load cases of analysis 6 reported in Table 6.4. Cases are 1 (a), 2 (b), 3 (c) and 4 (d).

The sixth analysis case corresponds to a cyclic bending moment simulation preceded by an initial 'pressure load step', which is the same as those presented in Section 6.3.1.

Discussion - Figure 6.12 shows the radial strain for analysis 1. The initial jump corresponds to the first time step where all gaps between layers close. These gaps develop between the adjacent layers of the riser during meshing due to the limited number of elements in the circumferential direction of each layer. As the simulation goes through cyclic internal and external pressure loading, the behaviour becomes more stabilised where a linear curve can be fitted to represent the overall behaviour.

Figure 6.13 shows the radial displacement resulted from case 2. The cyclic response of radial displacement due to cyclic internal and external loading is unlikely due to frictional dissipation between adjacent layers but potentially due to the gaps closure and opening at the initiation of each cycle. Therefore a linear curve fitting assumption for this case is made..

Radial displacements resulting from analysis 3 are shown in Figure 6.14. The magnitudes of these displacements are far less than those for case 2 and can be ignored, but are curve fitted linearly and considered in the constitutive model.

Figure 6.15 shows the radial displacement of analysis 4. This figure illustrates the characteristics of the variable P_u. An increase in this variable makes an inward or outward overall radial movement of all layers and does not create any compression. Furthermore, there is not frictional dissipation, no gap opening and closure between layers. Therefore the response is clearly linear and a linear curve fitting is well suited to this curve.

All results of Figure 6.16, except for the case $P_\varepsilon = 0$, illustrate a hysteretic behaviour of the riser subjected to cyclic axial tension (Analysis 5), the response tending towards a stabilised cyclic response gradually as the number of cycles increases. The first cycle represents the installation phase, whereas the stabilised results are more suitable to be used for the calibration procedure, which will be discussed in the next section. This figure also shows that the higher the pressure, the greater the energy dissipated during the hysteresis loop.

6.4.2 Calibration of the constitutive model

Several finite element simulations, presented in Section 6.4.1, have been used to calibrate the constitutive model. Each result from the numerical simulations was curve fitted either using a linear or bilinear curve, based on the stabilised cycle. The linear curve yields a constant slope (Analysis 1 to 4). The bilinear curve can give three specific parameters for the constitutive model (Analysis 5 and 6): the initial no-slip slope, a slip-initiation point, and a full-slip slope.

In Figures 6.17 to 6.20, five representative results from the finite element simulations, Analyses 1 to 4, are shown together with the fitted linear curves on their stabilised part. All figures, except Figure 6.20, show an initial jump which is due to gap closure at the early stage of each cycle and should be ignored while calculating the parameters.

Figure 6.17: Representative results from the finite element simulations, Analysis 1, and related fitted linear curves.
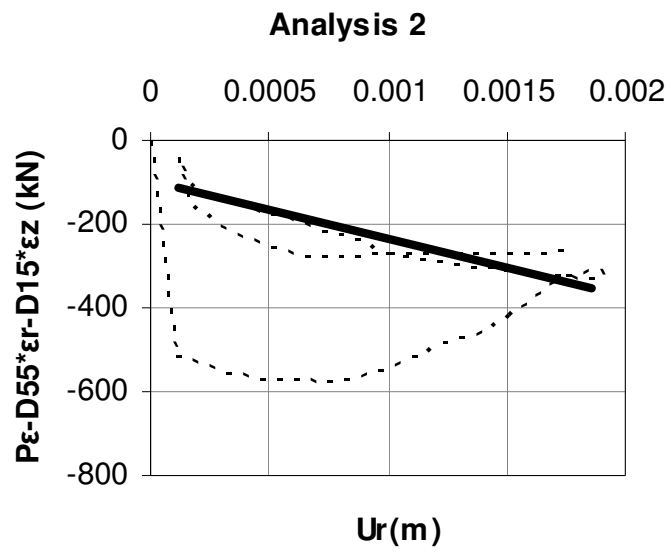
Analysis 2

Figure 6.18: Representative result from the finite element simulations, Analysis 2, and related fitted linear curve.

Analysis 3

Figure 6.19: Representative result from the finite element simulations, Analysis 3, and related fitted linear curve.
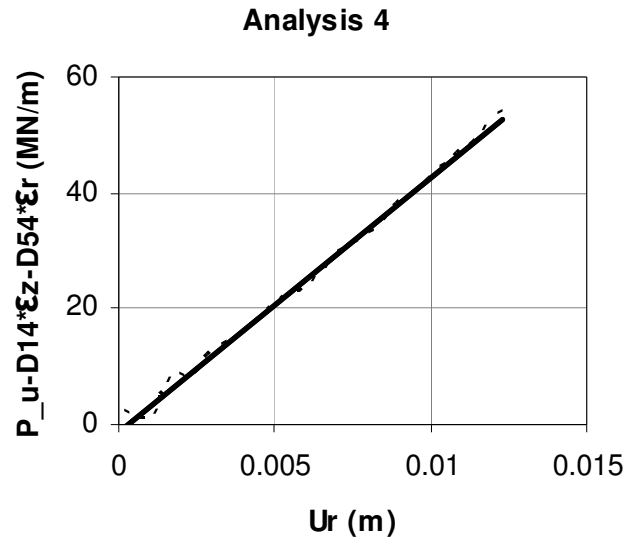
Figure 6.20: Representative result from the finite element simulations, Analysis 4, and related fitted linear curve.

For Analyses 1 to 4 a linear response can be identified. These slopes directly provides the flexural stiffnesses $D_{55}, D_{15} = D_{51}$ and $D_{45} = D_{54}$ by using appropriate equations from the fifth column of Table 6.3. For example D_{55} is the slope of linear curve in Figure 6.17 because $D_{55}\varepsilon_r = P_\varepsilon$.

Figure 6.21 shows two representative results from the finite element simulations, Analysis 5, together with the fitted bilinear curves on their stabilised part. Negative offset of the radial strain is due to the compression as a result of the initial pressure loading step.

For all cases except those with zero or very small applied pressure, an initial linear response can be identified. Therefore, an initial 'no-slip slope' can be determined and is found to be the same for each of the analysed cases. This validates the hypothesis that an initial linear part of the force-displacement diagram, in which frictional slip between layers is absent or negligible, does exist. This slope directly provides the flexural stiffness D_{11}.

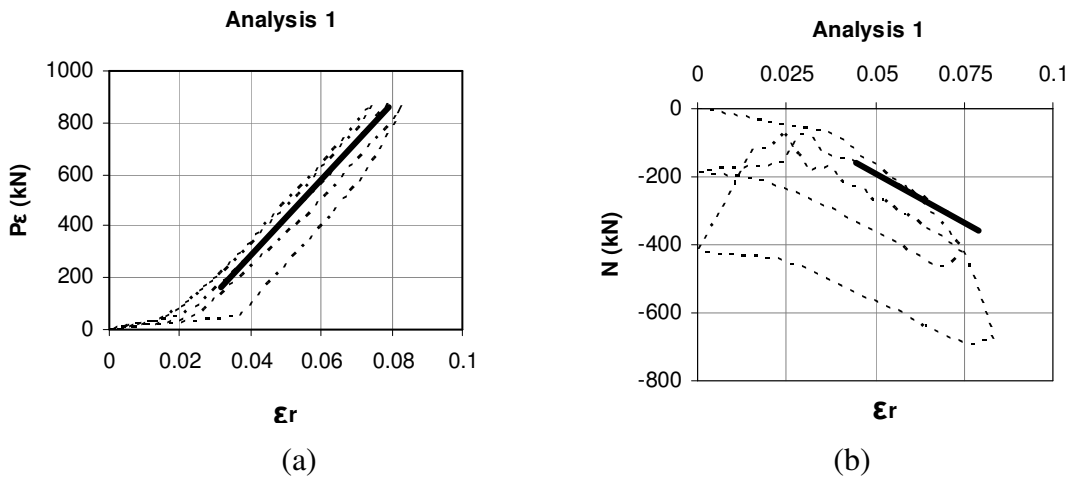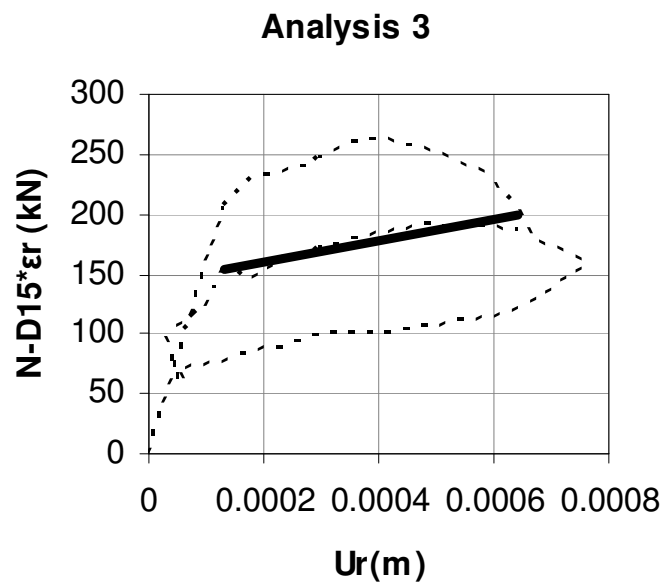**Analysis 5 - Pε = 145.6 kN**

(a)
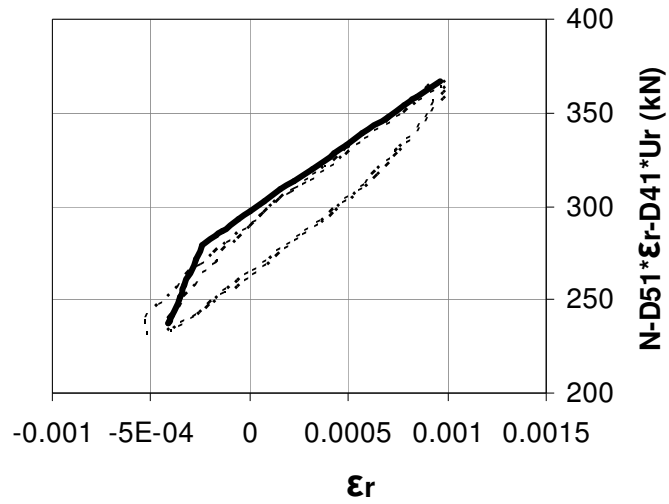
Analysis 5 - Pε=436.9 kN
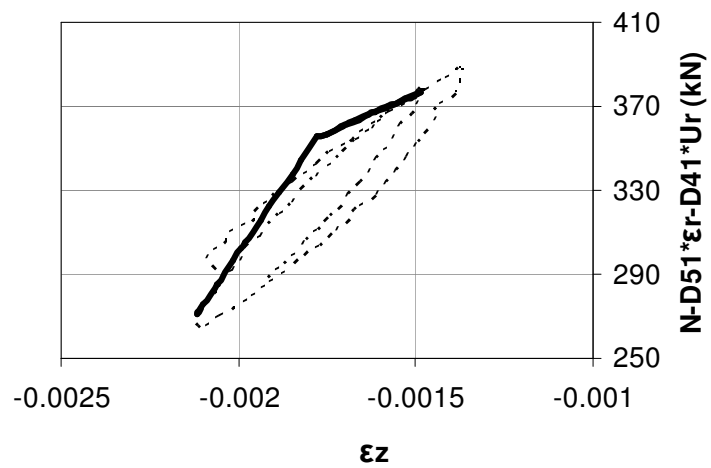
(b)

Figure 6.21: Two representative results from the finite element simulations, Analysis 5, and related fitted bilinear curves.
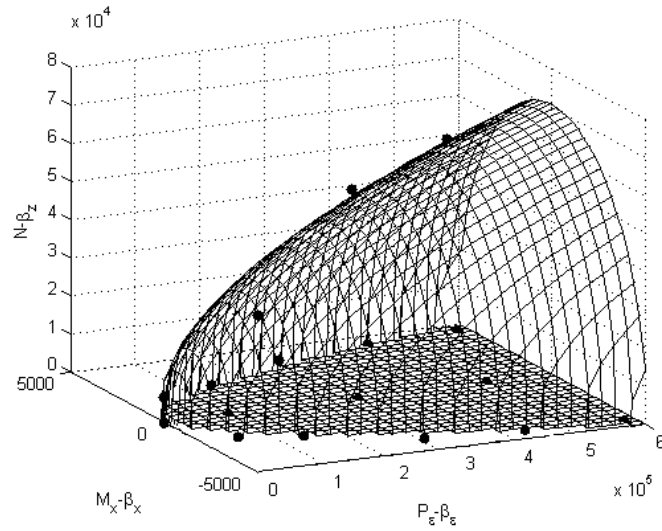
Figure 6.22: Curve-fitting of the slip-initiation points.

After this initial linear response, a non-linear part of the curve follows, which relatively rapidly tends to join a final full-slip slope. Upon repeated loading and unloading cycles, this final slope changes and stabilizes on a straight line which is that used in the identification procedure. This final full-slip slope is not equal to the hardening parameter H_{11}, but it is related to it and therefore its determination allows to estimate H_{11}.

The intersection point between the initial slope and the final slope provides a 'slip-initiation' point, which is also a point of the boundary of the no-slip domain, i.e. a point of the zero level set of the slip-onset function in the $N - P_\varepsilon$ plane.

The slip-initiation points identified have been fitted with the quadratic expression of Equation (6.24) and the resulting surfaces are shown in Figure 6.22. Table 6.6 reports the parameters of the model determined by the proposed procedure.

Table 6.6: Identified parameters.

Stiffness		Slip-onset function		Hardening	
D_{11}(N)	$2.5 \cdot 10^8$	a	0	H_{11} (N)	$7.3 \cdot 10^7$
D_{41}(Nm^{-1})	$1.28 \cdot 10^8$	b (N^{-1})	$1.2 \cdot 10^{-4}$	H_{22} (Nm^2)	$2.5 \cdot 10^5$
D_{51}(N)	$-5.88 \cdot 10^6$	c (N^{-1} m^{-2})	$2.3 \cdot 10^{-2}$		
D_{22} (Nm^2)	$6.08 \cdot 10^5$				
D_{44}(Nm^{-2})	$4.38 \cdot 10^9$				
D_{54} (Nm^{-1})	$-1.36 \cdot 10^8$				
D_{55}(N)	$1.52 \cdot 10^7$				

6.4.3 Validation of the constitutive model

To evaluate the proposed method, the same tensile cyclic analyses performed in Section 6.4.1 using the detailed finite-element model in ABAQUS have been reproduced using the proposed constitutive model adopting the parameters of Table 6.6 and using the solution scheme described in Section 6.2.3.

Results of this verification are reported in Figure 6.23 for four cases corresponding to four values of the applied pressure load P_ε. For each case a graph is reported in which the load-displacement curve obtained with the proposed constitutive model is plotted with a solid line and is compared with the dotted-line curve obtained using the detailed finite-element model. These results exclude the initial pressure loading step.

In case 1 ($P_\varepsilon = 0$), no friction occurs in both cases, which means no energy dissipation. For cases 2,3 and 4, the constitutive model simulates an almost same hysteresis response as the finite element results in terms of overall behaviour, which indicates the amount of energy dissipated due to friction between individual layers.
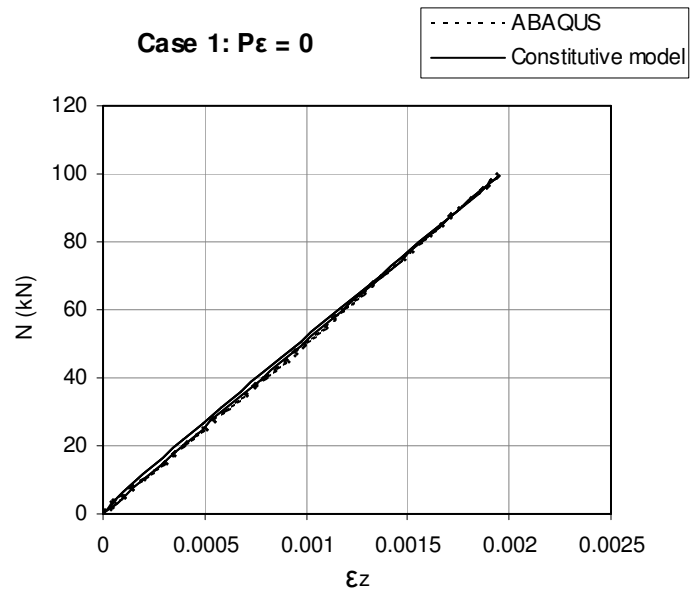
(a)
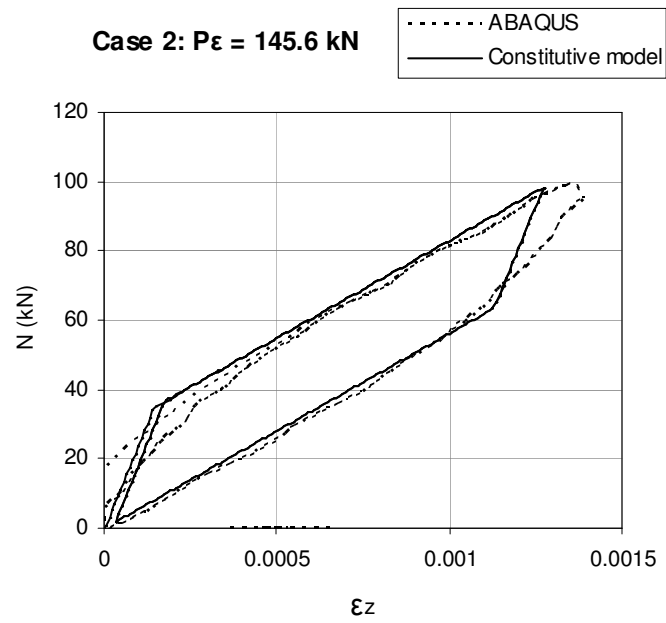
(b)
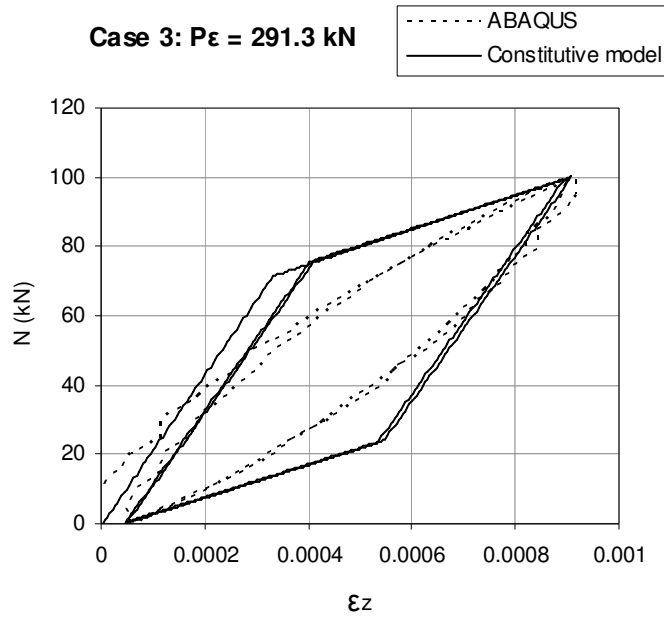
(c)
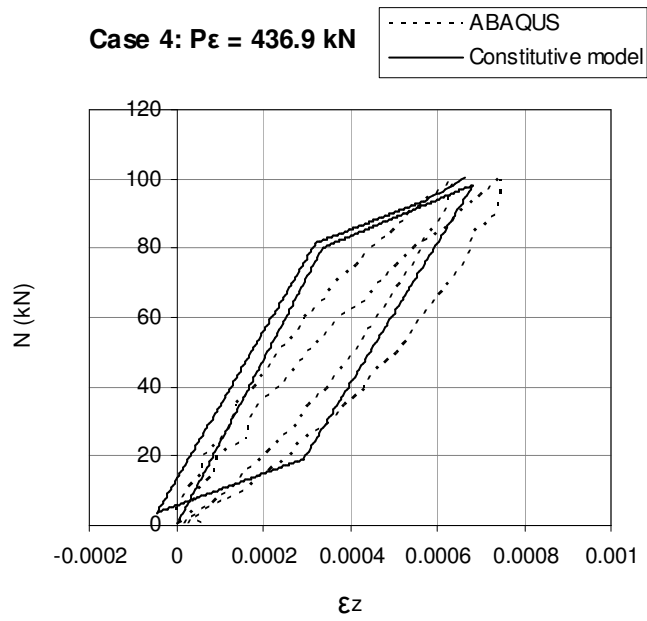
(d)

Figure 6.23: Comparison of the results obtained from the constitutive model (solid line) and from the detailed finite element model (dotted-line).

6.4.4 Consistent tangent operator

The constitutive model, developed in Section 6.4, is now formulated in a consistent tangent operator which can then be implemented into a generalised finite element formulation. Alfano *et al.* (1999) presented a general approach to the evaluation of this operator for associated rate-independent elasto plasticity materials. The procedure is to follow the method developed by Alfano *et al.* (1999) for the case of associated plasticity extending it to the non-associated case of interest here. Re-writing Equations (6.13) when a fully implicit backward-Euler time-integration scheme is adopted yields:

$$
\begin{cases}
\underline{\sigma}_{n+1} = \hat{D}\left(\underline{\varepsilon}_{n+1} - \underline{\varepsilon}_{s,n+1}\right) \\[2mm]
\underline{\varepsilon}_{s,n+1} - \underline{\varepsilon}_{s,n} = \Delta\lambda \left.\dfrac{\partial g}{\partial \underline{\sigma}}\right|_{n+1} \\[3mm]
\underline{\beta}_{n+1} = \hat{H}\,\underline{\varepsilon}_{s,n+1} \\[2mm]
\Delta\lambda \geq 0 \quad f\left(\underline{\sigma}_{n+1} - \underline{\beta}_{n+1}\right) \leq 0 \quad \Delta\lambda\, f\left(\underline{\sigma}_{n+1} - \underline{\beta}_{n+1}\right) = 0
\end{cases}
\tag{6.28}
$$

Differentiating Equation $(6.28)_1$ with respect to $\underline{\varepsilon}_{n+1}$, we get

$$
\frac{\partial \underline{\sigma}_{n+1}}{\partial \underline{\varepsilon}_{n+1}} = \hat{D}\left(\hat{I} - \frac{\partial \underline{\varepsilon}_{s,n+1}}{\partial \underline{\varepsilon}_{n+1}}\right)
\tag{6.29}
$$

From Equation $(6.28)_2$ we get the expression

$$
d\underline{\varepsilon}_{s,n+1} = d\Delta\lambda\,\underline{m} + \Delta\lambda \left.\frac{\partial^2 g}{\partial \underline{\sigma}^2}\right|_{n+1} d\underline{\sigma}_{n+1} + \Delta\lambda \left.\frac{\partial^2 g}{\partial \underline{\sigma}\partial \underline{\beta}}\right|_{n+1} d\underline{\beta}_{n+1}
\tag{6.30}
$$

The assumed definition Equation (6.24) implies that

$$
\frac{\partial^2 g}{\partial \underline{\sigma}\partial \underline{\beta}} = \frac{\partial^2 g}{\partial \underline{\beta}\partial \underline{\sigma}} = \frac{\partial^2 g}{\partial \underline{\beta}^2}
\tag{6.31}
$$

113

Substituting Equation (6.31) into Equation (6.30), and then substituting the result into Equation (6.29) and the derivative of Equation (6.28)₃ provides the following system of equations:

$$
\begin{vmatrix}
\hat{D}^{-1} + \Delta\lambda \dfrac{\partial^2 g}{\partial \underline{\sigma}^2}\bigg|_{n+1} & -\Delta\lambda \dfrac{\partial^2 g}{\partial \underline{\sigma}^2}\bigg|_{n+1} \\[2ex]
-\Delta\lambda \dfrac{\partial^2 g}{\partial \underline{\sigma}^2}\bigg|_{n+1} & \hat{H}^{-1} + \Delta\lambda \dfrac{\partial^2 g}{\partial \underline{\sigma}^2}\bigg|_{n+1}
\end{vmatrix}
\begin{vmatrix} d\underline{\sigma}_{n+1} \\ d\underline{\beta}_{n+1} \end{vmatrix}
=
\begin{vmatrix} d\underline{\varepsilon}_{n+1} - d\Delta\lambda \underline{m} \\ d\Delta\lambda \underline{m} \end{vmatrix}
\tag{6.32}
$$

From which we obtain

$$
\begin{aligned}
d\underline{\sigma}_{n+1} &= \hat{D}d\underline{\varepsilon}_{n+1} - \Delta\lambda \hat{D}\hat{Q}\hat{F}^{-1}\hat{D}d\underline{\varepsilon}_{n+1} + \Delta\lambda d\Delta\lambda \hat{D}\hat{Q}\hat{F}^{-1}(\hat{D}+\hat{H})\underline{m} - d\Delta\lambda \hat{D}\underline{m} \\
d\underline{\beta}_{n+1} &= \Delta\lambda \hat{H}\hat{Q}\hat{F}^{-1}\hat{D}d\underline{\varepsilon}_{n+1} - \Delta\lambda d\Delta\lambda \hat{H}\hat{Q}\hat{F}^{-1}(\hat{D}+\hat{H})\underline{m} + d\Delta\lambda \hat{H}\underline{m}
\end{aligned}
\tag{6.33}
$$

where

$$
\hat{Q} = \frac{\partial^2 g}{\partial \underline{\sigma}^2}\bigg|_{n+1}
\tag{6.34}
$$

The fulfilment of Prager's consistency condition $f = \dot{f} = 0$ implies (Han and Reddy, 1999)

$$
\left(d\underline{\sigma}_{n+1} - d\underline{\beta}_{n+1} \right) \bullet \underline{n} = 0
\tag{6.35}
$$

Substituting Equations (6.33) into Equation (6.35) results in $\Delta\lambda$ as below

$$
\Delta\lambda = \frac{\left[\hat{D} - \Delta\lambda(\hat{D}+\hat{H})\hat{Q}\hat{F}^{-1}\hat{D} \right] d\underline{\varepsilon}_{n+1} \bullet \underline{n}}{\left[(\hat{D}+\hat{H}) - \Delta\lambda(\hat{D}+\hat{H})\hat{Q}\hat{F}^{-1}(\hat{D}+\hat{H}) \right]\underline{m} \bullet \underline{n}}
\tag{6.36}
$$

By substituting Equation (6.36) into Equation (6.28)₁ we obtain

$$
\frac{d\underline{\sigma}}{d\underline{\varepsilon}}\bigg|_{n+1} = (\hat{D} - \lambda\hat{D}\hat{Z}\hat{D}) - \frac{\left[\hat{D} - \lambda\hat{D}\hat{Z}(\hat{D}+\hat{H}) \right]\underline{m} \otimes \left[\hat{D} - \lambda\hat{D}\hat{Z}(\hat{D}+\hat{H}) \right]\underline{n}}{\left[(\hat{D}+\hat{H}) - \lambda(\hat{D}+\hat{H})\hat{Z}(\hat{D}+\hat{H}) \right]\underline{m} \bullet \underline{n}}
\tag{6.37}
$$

114

where

$$\hat{Z} = \hat{Q}\hat{F}^{-1} \tag{6.38}$$

Substituting matrices and performing cross and dot products yields to the final equation which is given in Appendix B. This operator can now be implemented into a generalised finite element beam model to study a large-scale analysis while considering the small-scale frictional slip occurring between the layers in an unbonded flexible riser.

6.5 Discussion

The comparison between the curves provided by the constitutive model and the stabilised cycles obtained using the finite element numerical simulations indicate a reasonable agreement in terms of the overall response. The model accurately captures the minimum and maximum magnitudes of all cases of different input pressures. The initial stiffnesses of all cases compare well with the stabilised initial slopes of the finite element numerical simulations. The hardening stiffnesses of all cases also perfectly capture the all final full-slip slopes of the finite element simulations.

It is worth noting that for all cases the same stiffness and hardening parameters have been used, that these parameters have been determined by interpolating the finite element results with a bilinear curve only assuming a monotonic case, and that very good agreement is reached for cases with significantly different values of the pressure and for the entire stabilised cycles.

The constitutive model is robust enough to capture many practical loadings and has the capability to be easily improved, enhanced and extended. One possible way would be to change its response from linear to non-linear, which then would be able to match finite element simulation or experimental results much more accurately in terms of gradual change of stiffness between no-slip and full-slip criteria.

7 Conclusions and recommendations for future work

7.1 Conclusions
7.1.1 Numerical modelling

In Chapter 3 a three-dimensional finite element model incorporating contact interaction, geometric non-linearity and friction has been developed to accurately simulate the structural response of a six-layer unbonded flexible riser. The model is used to generate load-displacement relationships for various load cases.

Almost all the weaknesses of analytical methods can be overcome using detailed, three-dimensional finite-element (FE) analyses, as is shown in recent work by the authors (Bahtui *et al.*, 2008b). However, the downside of this type of analysis is the high computational cost so that, to make the analysis feasible, the riser model length is restricted to only few meters in the best case scenario for which top-end computational facilities and a large solution time are available.

7.1.2 Analytical modelling

In Chapter 4 an analytical formulation has been derived by combining together three different analytical approaches (Lanteigne 1985; Kraincanic and Kebadze 2001; McNamara and Harte 1989) proposed in the literature. This model includes the slip effects in the three dimensional sense as well as layer separation and bird-caging phenomena. A switch scheme is also incorporated to prevent layer penetration. The analysis considers the main modes of flexible riser loading consisting of tension, torsion, bending moment and internal and external pressure.

7.1.3 Validation and verification of the numerical and the analytical modelling

In Chapter 5 the results from the detailed three-dimensional numerical model, developed in Chapter 3, and analytical models, derived in Chapter 4, are compared in all the load cases considered. It is shown that there is a good correlation between the finite element and the analytical models. Results show that friction has significant damping effect in bending moment analysis. Results from cyclic loading analysis show that friction has potential effect in cyclic tensile and torsional loadings at higher load levels.

Experimental data are not widely available in the literature. There is very limited reference in the literature to any realistic flexible pipe structure with its construction details and material properties, or to any experimental data. Experimental investigation is also too expensive which limits researchers for validating their analytical results.

It has been demonstrated in this work that the detailed three-dimensional finite element model can be used as a virtual testing machine to efficiently conduct parametric studies on the unbonded flexible riser and to predict its behaviour under various loading conditions. Using the numerical approach, physical experimental tests will only be required as 'one-off' checks to validate the virtual model. A numerical model carefully created and validated against test data enables cost-effective parametric investigations, which can in turn lead to improved riser design.

7.1.4 The constitutive model

In Chapter 6 a new method has been proposed for the formulation of constitutive models for flexible risers, suitable for large-scale analyses, and for the identification of the related input parameters. The approach used is multi-scale and entirely numerical. At the small scale, a detailed finite-element model of a riser of small-length has been used to conduct several numerical simulations for different values of the applied loads and internal/external pressure. This model accurately takes into account the detailed

geometry of the riser and the frictional contact between various layers. At the large scale, an Euler-Bernoulli beam model has been developed with the addition of suitable pressure terms in the generalised stresses to account for the internal and external pressures. The constitutive law for the beam model has been derived based on a set of assumptions which are motivated by the analogy between the structural response obtained in the numerical simulations and that of an elasto-plastic model with non-associative type of flow rule, the frictional slipping between the different layers of the riser producing a similar type of response as the frictional slipping of micro-planes in a continuum medium. The parameters of the beam constitutive law are identified by ensuring that the analyses performed at different scales provide as close as possible results for a number of representative cases.

In this proposed model, the non-linear transitional regime between the initial no-slip response and the final full-slip response is replaced with a bilinear response and a sharp elbow at the slip-initiation point. During the transition phase one part of the layers in contact (particularly the armour tendons) slip with respect to each other, and another part of them do not. Although the results of the proposed simplified model can be accurate enough in many cases, it is important to underline that the method can be further refined, as discussed in Section 7.2.2.

The model has been developed specifically for the important cases of cyclic bending loading and cyclic tensile loading of a riser subject to different values of internal and external pressures. In these developments of the method, linear kinematic hardening has been assumed. Satisfactory agreement has been obtained between the overall response provided by the proposed (large-scale) model and that of the detailed (small-scale) finite element simulations. This makes this constitutive model already suitable to study many problems, such as hysteretic damping in vibration analysis.

7.1.5 Validation of the constitutive model

The validations, presented in Sections 6.3.3 and 6.4.3, indicate a reasonable agreement in terms of the overall response of the riser. This demonstrates that the assumptions on

which the constitutive model is based are well justified and that the proposed approach can represent an excellent method of analysis for long flexible risers.

7.1.6 Main contributions to the knowledge

The original contributions of the present work to the knowledge are outlined below:

- The constitutive model, developed in Chapter 6, describes a very detailed behaviour of the unbonded flexible risers in terms of highly non-linear geometric behaviour, the inter-layer contact and stick-slip effects. The beam model supplemented with the proposed constitutive law is suitable for large-scale analysis, unlike the detailed finite element model used to formulate it and to determine its parameters. A typical model which requires several days of computational solution time takes less than a second to be simulated by the constitutive model. The constitutive model, on the other hand, is able to capture all the important aspects of the structural response of the riser.

- Existing commercial packages uses "Composite" riser modelling scheme, while this work presents a fully multi-layer modelling scheme which accurately captures all the geometric non-linearities, due to the helical configuration of the tendons within a helical layer, the material nonlinearities due to the polymeric layers, and non-linearity introduced by layer interaction and the changing contact conditions under load.

- Using the small-scale detailed finite element model, presented in Chapter 3, it is possible to conduct parametric studies on the factors that influence the strength and stiffness of risers. Such studies are difficult to conduct under laboratory test conditions due to the physical size of the risers and also due to the special experimental equipment required, and are therefore usually considered to be too expensive and time consuming. The three-dimensional model, as a virtual experimental rig, offers advantages at each stage of the process. At the design stage, it allows operators to compare various riser designs. Until now,

comparing different designs has been difficult because of the extent to which risers can differ. More accurate modelling also can result in targeted changes to technical specifications during design. This helps to optimize performance and minimize manufacturing cost. During installation, the numerical modelling increases the confidence with which a project can proceed to riser laying. Modelling can also reduce installation costs and time because more precise assessments can be made of installation equipment and procedures.

- The analytical model, presented in Chapter 4, brings the capability to validate finite element model of different types of unbonded flexible risers. The method developed for the analytical model makes it feasible to study different types of risers consisting of various numbers of layers each one having a different type such as helical armour layer, carcass, pressure armour and sheath layer. The model allows separation and compression between individual layers of the riser through the development of the switch algorithm.

7.2 Recommendations for future work

The following suggestions are put forward for future investigations.

7.2.1 The numerical model

The numerical model can be enhanced and improved by

- Reducing the amount of gap between individual layers by
  a. Replacing linear elements by elements of quadratic interpolation
  b. Increasing the number of elements in the circumferential direction.
- Further investigation of the boundary conditions to be applied to the local model to ensure full consistency in the transfer of the related results to the constitutive model for the global flexible riser.

- Development of a robust and efficient automated procedure to identify the input parameters for the riser model which results in an optimal fit of the flexible pipe results.
- To replace the existing carcass layer by a more detailed layer.
- To add more layers to the riser such as interlocked pressure armour layers.

7.2.2 The constitutive model

- The constitutive model can be significantly improved by including non-linear hardening as well as more refined hardening models capable of simulating the stabilization of the response during cyclic loading. This would be through replacing the current mathematical theory by non-linear theory of plasticity. The new non-linear model would better fit finite element or experimental results and thus would be more suited for further cyclic analysis.
- Further improvements can be made by accounting for the presence of the shear force (switching to a Timoshenko beam model) and by incorporating the influence of variable axial force and torque on the non-linear response.
- Clearly, more sophisticated models will also imply more parameters to be identified and therefore call on the development of more refined identification procedures.
- The constitutive model for bending moment-curvature, presented in Chapter 6, can be extended to simulate the hysteresis behaviour in torsional loading by extending the slip onset criterion to a four-dimensional space.
- The sensitivity of the parameters of the constitutive model can be analysed to study their effect on the results from the constitutive model. A suitable domain for each parameter may be derived.

7.2.3 Development of constitutive models for global analysis

- To undertake a global non-linear riser large displacement dynamic analysis to determine the maximum loads for strength and cyclic loads for fatigue damage

of the steel layers by implementing the proposed stick-slip hysteretic constitutive model into the finite element code to analyze the highly non-linear behaviour of long unbonded flexible riser structures.

- To implement the resulting hysteretic constitutive model into a marine riser analysis code to perform vortex induced vibration VIV computational calculations and study its response.

- All existing riser technology packages, which uses the "composite" modelling scheme, can be potentially improved by replacing the stiffness behaviour by the proposed non-linear constitutive model.

Bibliography

ABAQUS (2007). *ABAQUS Theory Manual, ABAQUS version 6.6 Documentation.* Rhode Island: Hibbitt, Karlsson and Sorensen.

API Recommended Practice 17B (2002). *Recommended Practice for Flexible Pipe,* American Petroleum Institute.

API Specification 17J (2002). *Specification for Unbonded Flexible Pipe,* 2nd Ed. American Petroleum Institute.

Alfano G., Bahtui A., Bahai H. (2008). 'Numerical derivation of constitutive models for unbonded flexible risers', Submitted to *International Journal of Mechanical Sciences*.

Alfano G., Rosati L., Valoroso N. (1999). 'A Tangent-secant Approach to Rate-independent elastoplasticity: Formulations and Computational Issues', *Computer Methods in Applied Mechanics and Engineering* **179**: 379-405.

Atadan, A.S., Calisal, S.M., Modi, V.J., and Guo, Y. (1997). 'Analytical and numerical analysis of the dynamics of a marine riser connected to a floating platform', *Ocean Engineering* **24**(2): 111-131.

Bahtui A., Bahai H., Alfano G. (2007). 'Numerical and analytical simulation of unbonded flexible risers subjected to combined modes of loading', *9th US National Congress on Computational Mechanics*, San Francisco, CA July 23-26.

Bahtui A., Bahai H., Alfano G. (2008a). 'A finite element analysis for unbonded flexible risers under axial tension', *Proceedings of OMAE2008 27th International Conference on Offshore Mechanics and Arctic Engineering*, Estoril, Portugal, June 15-20.

Bahtui A., Bahai H., Alfano G. (2008b). 'A finite element analysis for unbonded flexible risers under torsion', *Journal of Offshore Mechanics and Arctic Engineering (OMAE)* **130**(4): 041301 (4 pages).

Bahtui A., Bahai H., Alfano G. (2008c). 'Constitutive modelling of unbonded flexible risers under tension', *8th World Congress on Computational Mechanics (WCCM8 - ECCOMAS 2008)*, Venice, Italy, June 30 – July 5.

Bahtui A., Bahai H., Alfano G. (2008d). 'Numerical and analytical modelling of unbonded flexible risers', *Journal of Offshore Mechanics and Arctic Engineering (OMAE), In Press*.

Bahtui A., Hosseini-Kordkheili S.A., Bahai H., Alfano G. (2008e). 'A multi-scale computational model for unbonded flexible risers', *Under development*.

Bech, A., Skallerud, B. and Sodahl, N. (1992). 'Structural damping in design analysis of flexible risers', *Proceedings of the first European conference on flexible pipes, umbilicals & marine cables, MARINFLEX 92*, London, UK, 1-14.

Brack, M., Troina, L.M.B. and Sousa, J.R.M. (2005). 'Flexible riser resistance combined axial compression, bending, and torsion in ultra-deep water depths', *Proceedings of 24th International Conference on Offshore Mechanics and Arctic Engineering, OMAE05*, June 12-17, Halkidiki, Greece.

Claydon, P., Cook, G., Brown, P.A. and Chandwani, R. (1992). 'A theoretical approach to prediction of service life of unbonded flexible pipes under dynamic loading conditions', *Marine Structures*, **5**, 5 399-429.

Felippa, C. A. and Chung, J. S. (1980). 'Nonlinear static analysis of deep-ocean mining pipe EM DASH 1. Modeling and formulation', *American Society of Mechanical Engineers,* **80**, 48 6pages.

Felippa, C. A. and Chung, J. S. (1981a). 'Nonlinear static analysis of deep-ocean mining pipe EM DASH 1. Modeling and formulation', *Journal of Energy Resources Technology, Transactions of the ASME*, **103**, 1 11-15.

Felippa, C. A. and Chung, J. S. (1981b). 'Nonlinear static analysis of deep-ocean mining pipe EM DASH 2. Numerical studies', *Journal of Energy Resources Technology, Transactions of the ASME*, **103**, 1 16-25.

Feret, J.J. and Bournazei, C.L. (1987). 'Calculation of stresses and slip in structural layers of unbonded flexible pipes', *Journal of Offshore Mechanics and Arctic Engineering*, **109**, 263-269.

Feret, J.J., Bournazei, C.L. and Rigaud, J. (1986). 'Evaluation of flexible pipes' life expectancy under dynamic conditions', *The 18th Annual Offshore Technology Conference, OTC86*, Houston , TX, USA, May 5-8, 83-90.

Garg , Sabodh K. & Svalbonas, Vytas & Gurtman, Gerald A. (1973). *Analysis of structural composite materials*, New York: Marcel Dekker, Chapter 2.

Han, W. and Reddy, B.D. (1999). *Plasticity – Mathematical theory and numerical analysis*, New York: Springer-Verlag, Chapter 3.

Harte, A.M. and McNamara, J.F. (1993). 'Modelling procedures for the stress analysis of flexible pipe cross sections', *Transactions of the ASME*, **115**, 46-51.

Hibbitt, H.D., Becker, E.B. and Taylor, L.M. (1979). 'Nonlinear analysis of some slender pipelines', *Computer Methods in Applied Mechanics and Engineering*, **17-18**, 1 203-25.

Hoffman, D., Ismail, N., Nielsen, R. and Chandwani, R. (1991). 'Design of flexible marine riser in deep and shallow water', *Proceedings 23rd Annual Offshore Technology Conference, OTC91*, Houston, TX, USA, 253-265.

Hyer, Michael W. (1998). *Stress analysis of fiber-reinforced composite materials*, Boston: McGraw-Hill.

Kagoura, T., Ishii, K., Abe, S., Inoue, T., Hayashi, T., Sakamoto, T., Mochizuki, T., and Yamada, T. (2003). 'Development of a flexible pipe for pipe-in-pipe technology', *Furukawa Review* **24**: 69-75.

Kebadze, E. (2000). *Theoretical modelling of unbonded flexible pipe cross-sections*, PhD thesis, London: South Bank University.

Kebadze, E. and Kraincanic, I. (1999). 'Non-linear bending behaviour of offshore flexible pipes', *Proceedings of the 9th International Offshore and Polar Engineering Conference, ISOPE-99*, **2**, 226-233.

Knapp, R.H. (1979). 'Derivation of a new stiffness matrix for helically armoured cables considering tension and torsion', *International Journal for Numerical Methods in Engineering*, **14**, 4 515-529.

Knupp, P.M. (2000). 'Achieving finite element mesh quality via optimization of the jacobian matrix norm and associated quantities', *International Journal for Numerical Methods in Engineering*, **48**, 8 1165-1185.

Kraincanic, I. and Kebadze, E. (2001). 'Slip initiation and progression in helical armouring layers of unbonded flexible pipes and its effect on pipe bending Behaviour', *Journal of Strain Analysis*, **36**, 3 265-275.

Lacarbonara, W. and Pacitti, A. (2008). 'Nonlinear modeling of cables with flexural stiffness', *Mathematical Problems in Engineering* **2008**(370767): 1-21.

Lanteigne, J. (1985). 'Theoretical estimation of the response of helically armoured cables to tension, torsion, and bending', *Transactions of the ASME, Journal of Applied Mechanics*, **52**, 2 423-432.

Lempriere, B.M. (1968). 'Poisson's ratio in orthotropic materials', *AIAA Journal*, **6**, 11 2226-2230.

Leroy, J.-M. and Estrier, P. (2001). 'Calculation of stresses and slips in helical layers of dynamically bent flexible pipes', *Oil & Gas Science and Technology – Rev. IFP*, **56**, 6 545-554.

Machado, Z.L. and Dumay, J.M. (1980). 'Dynamic production riser on Enchova field offshore Brazil', *Offshore Brazil conference, Latin America Oil Show*, Rio de Janeiro.

MATLAB (2006). R2006a, *The MathWorks, Inc*.

McConnell, K.G. and Zemke, W.P. (1982). 'A model to predict the coupled axial torsion properties of ACSR electrical conductors', *Experimental Mechanics*, **22**, 7 237-244.

McIver, D.B. (1995). 'A method of modelling the detailed component and overall structural behaviour of flexible pipe sections', *Engineering Structures*, **17**(4): 254-266.

McNamara, J. F. and Lane, M. (1984). 'Practical modelling for articulated risers and loading columns', *Journal of Energy Resources Technology, Transactions of the ASME*, **106**, 4 444-450.

McNamara, J.F., Harte, A.M. (1989). 'Three dimensional analytical simulation of flexible pipe wall structure', *In Proceedings of the 8th International Conference on Offshore Mechanics and Arctic Engineering*, **1**(8): 477-482.

McNamara, J. F. and Lane, M. (1992). '3D frequency domain analysis of offshore structures', *Proceedings of the 9th Conference on Engineering Mechanics*, College Station, TX, USA, 192-195.

McNamara, J. F., and O'Brien, P. J. and Gilroy, S. G. (1988). 'Nonlinear analysis of flexible risers using hybrid finite elements', *Journal of Offshore Mechanics and Arctic Engineering*, **110**, 3 197-204.

Nielsen, R., Colquhoun, R.S., McCone, A., Witz, J.A. and Chandwani, R. (1990). 'Tools for predicting service life of dynamic flexible risers', *Proc First European Offshore Mechanics Symposium*, Trondheim, Norway, 449-456.

O'Brien, P. J., McNamara, J. F. and Dunne, F. P. E. (1988). 'Three-dimensional nonlinear motions of risers and offshore loading towers', *Journal of Offshore Mechanics and Arctic Engineering*, **110**, 3 232-237.

O'Brien, P. J. and McNamara, J. F. (1988). 'Analysis of flexible riser systems subject to three-dimensional seastate loading', *Proceedings of the international conference on behaviour of offshore structures, BOSS 88*, Trondheim, Norway, 6 1373-1388.

Oliveira, de J.G., Goto, Y. and Okamoto, T. (1985). 'Theoretical and methodological approaches to flexible pipe design and application', *Annual Offshore Technology Conference*, Houston, TX, USA, 6-9 May, 517.

Ong, P.P.A. and Pellegrino, S. (2003). 'Modelling of seabed interaction in frequency domain analysis of mooring cables', *Proceedings of 22nd international conference on offshore mechanics and arctic engineering ASME, OMAE03*, Cancun, Mexico, 1-9.

Out, J.M.M. (1989). 'On the prediction of the endurance strength of flexible pipe', *Offshore Technology Conference*, OTC89, Texas, May 1-4.

Out, J.M.M., Kronemeijer, D.A., van de Loo, P.J. and de Sterke, A. (1995). 'The integrity of flexible pipe: search for an inspection strategy', *Engineering structures*, **17**, 4 305-314.

Out, J.M.M. and Morgen, B.J. von. (1997). 'Slippage of helical reinforcing on a bent cylinder', *Engineering Structures*, **19**, 6 507-515.

Patel, M.H. and Seyed, F.B. (1995). 'Review of flexible riser modelling and analysis techniques', *Engineering structures*, **17**, 4 293-304.

Raoof, M. and Kraincanic, I. (1994). 'Critical examination of various approaches used for analysing helical cables', *Journal of Strain Analysis*, **29**, 1 43-55.

Roger, C. (2000). 'Using ABAQUS to verify riser tension'. *2000 ABAQUS Users' Conference*, 161-170.

Saevik, S. (1993). 'A finite element model for predicting stresses and slip in flexible pipe armouring tendons', *Computers & Structures*, **46**, 2 219-230.

Saevik, S. and Berge, S. (1995). 'Fatigue testing and theoretical studies of two 4 in flexible pipes', *Engineering Structures*, **17**, 4 276-292.

Serta, O.B. and Brack, M. (1990). 'Stress and strain assessment of multi-layer flexible pipes', *Proceedings of the First European Mechanics Symposium, The International Society of Offshore and Polar Engineers*, Trondheim, Norway, August 20-22.

Smith, R., O'Brien, P., O'Sullivan, T. and Weibe, C. (2007). 'Fatigue analysis of unbonded flexible risers with irregular seas and hysteresis', *The 2007 Offshore Technology Conference, OTC07*, Houston, Texas, USA, April 30-May 3.

Tan, Z., Case, M. and Sheldrake, T. (2005). 'Higher order effects on bending of helical armour wire inside an unbonded flexible pipe', *Proceedings of 24th International Conference on Offshore Mechanics and Arctic Engineering, OMAE05*, Halkidiki, Greece, June 12-17.

Tuohy, J., Kalman, M., Chen, B., Williamson, D., Wilhelmsen, A., Berge, S., Sævik, S. and Løtveit, S.A. (1999). 'Qualification of a 15-inch ID flexible riser for export oil and gas service', *3rd European Conference on Flexible Pipes, Umbilicals and Marine Cables - Materials Utilisation for Cyclic and Thermal Loading (MARINFLEX'99)*, ed. J. A. Witz, Bentham Press, London, May.

Willden, R.H.J. and Graham, J.M.R. (2005). 'CFD simulations of the vortex-induced vibrations of model riser pipes', *Proceedings of the 24th International Conference on Offshore Mechanics and Arctic Engineering, OMAE05*, Halkidiki, Greece, **3**, 837-846.

Witz, J.A. (1996). 'A case study in the cross-section analysis of flexible risers', *Marine Structures*, **9**, 885-904.

Witz, J.A. and Tan, Z. (1989). 'An analysis method for the prediction of the long term mechanical degradation of unbonded flexible pipes', *BPP Report*, No. 7419A for Wellstream Corporation, Houston, USA.

Witz, J.A. and Tan, Z. (1992a). 'On the axial-torsional structural behaviour of flexible pipes, umbilicals and marine cables', *Marine Structures*, **5**, 205-227.

Witz, J.A. and Tan, Z. (1992b). 'On the flexural structural behaviour of flexible pipes, umbilicals and marine cables', *Marine Structures*, **5**, 229-249.

Witz, J.A. and Tan, Z. (1995). 'Rotary bending of marine cables and umbilicals', *Engineering Structures*, **17**, 4 267-275.

Yazdchi, M., Crisfield, M.A. (2002a). 'Buoyancy forces and the 2D finite element analysis of flexible offshore pipes and risers', *International Journal for Numerical Methods in Engineering* **54**: 61–88.

Yazdchi, M., Crisfield, M.A. (2002b). 'Nonlinear dynamic behavior of flexible marine pipes and risers', *International Journal for Numerical Methods in Engineering* **54**: 1265–1308.

Zhang, Y., Chen, B., Qiu, L., Hill, T. and Case, M. (2003). 'State of the art analytical tools improve optimization of unbonded flexible pipes for deepwater environments', *The 2003 Offshore Technology Conference*, Houston ,Texas, USA, May 5-8.

Appendix A - Newton-Raphson method

Many algorithms exist for solving nonlinear Equations. The Newton-Raphson method that has been widely used in finite element analysis will be presented in this section.

Assume that $f(x)$ and its derivative $f'(x)$ is defined and continuous on an interval about $x = p$, where $f(p) = 0$. Then there exist a $\delta > 0$ such that the sequence $\{p_k\}_{k=0}^{\infty}$ defined by the iteration

$$p_{k+1} = p_k - \frac{f(p_k)}{f'(p_k)} \ for \ k = 0,1,...$$

will converge to p for any initial approximation $p_0 \in [p - \delta, p + \delta]$. This equation is called the iteration scheme of the Newton-Raphson algorithm.

Appendix B – Consistent tangent operator

$$\frac{d\underline{\sigma}}{d\underline{\varepsilon}}\bigg|_{n+1} =$$

$$\frac{1}{\delta}\begin{bmatrix} \delta\theta_{111} - 4b^2\tau_1^2\Gamma_{111}^2 & -4bc\tau_1\tau_2\Gamma_{111}\Delta_{222} & -4bc\tau_1\tau_3\Gamma_{111}\Delta_{333} & \delta\theta_{411} - 2b\tau_1\Gamma_{111}(2b\tau_1\Gamma_{141} - \Gamma_{541}) & \delta\theta_{511} - 2b\tau_1\Gamma_{111}(2b\tau_1\Gamma_{151} - \Gamma_{551}) \\ -4bc\tau_1\tau_2\Gamma_{111}\Delta_{222} & \delta\Sigma_2 - 4c^2\tau_2^2\Delta_{222}^2 & -4c^2\tau_2\tau_3\Delta_{222}\Delta_{333} & -2c\tau_2\Delta_{222}(2b\tau_1\Gamma_{141} - \Gamma_{541}) & -2c\tau_2\Delta_{222}(2b\tau_1\Gamma_{151} - \Gamma_{551}) \\ -4bc\tau_1\tau_3\Gamma_{111}\Delta_{333} & -4c^2\tau_2\tau_3\Delta_{222}\Delta_{333} & \delta\Sigma_3 - 4c^2\tau_3^2\Delta_{333}^2 & -2c\tau_3\Delta_{333}(2b\tau_1\Gamma_{141} - \Gamma_{541}) & -2c\tau_3\Delta_{333}(2b\tau_1\Gamma_{151} - \Gamma_{551}) \\ \delta\theta_{141} - 4b^2\tau_1^2\Gamma_{111}\Gamma_{141} & -4bc\tau_1\tau_2\Gamma_{141}\Delta_{222} & -4bc\tau_1\tau_3\Delta_{141}\Delta_{333} & \delta\theta_{441} - 2b\tau_1\Gamma_{141}(2b\tau_1\Gamma_{141} - \Gamma_{541}) & \delta\theta_{541} - 2b\tau_1\Gamma_{141}(2b\tau_1\Gamma_{151} - \Gamma_{551}) \\ \delta\theta_{151} - 4b^2\tau_1^2\Gamma_{111}\Gamma_{151} & -4bc\tau_1\tau_2\Gamma_{151}\Delta_{222} & -4bc\tau_1\tau_3\Delta_{151}\Delta_{333} & \delta\theta_{451} - 2b\tau_1\Gamma_{151}(2b\tau_1\Gamma_{141} - \Gamma_{541}) & \delta\theta_{551} - 2b\tau_1\Gamma_{151}(2b\tau_1\Gamma_{151} - \Gamma_{551}) \end{bmatrix}$$

Where

$$\delta = 4b^2\tau_1^2\Pi_{11} + 4c^2\tau_2^2\Omega_{22} + 4c^2\tau_3^2\Omega_{33} - 2b\tau_1\Pi_{15}$$

$$\Pi_{ij} = D_{ij} + H_{ij} - \frac{2b\lambda(D_{ij} + H_{ij})(D_{ji} + H_{ji})}{1 + 2b\lambda(D_{ii} + H_{ii})}, \qquad \Omega_{ij} = D_{ij} + H_{ij} - \frac{2c\lambda(D_{ij} + H_{ij})(D_{ji} + H_{ji})}{1 + 2c\lambda(D_{ii} + H_{ii})}$$

$$\Gamma_{ijk} = D_{ij} - \frac{2b\lambda D_{kj}(D_{jk} + H_{jk})}{1 + 2b\lambda(D_{kk} + H_{kk})}, \qquad \Delta_{ijk} = D_{ij} - \frac{2c\lambda D_{kj}(D_{jk} + H_{jk})}{1 + 2c\lambda(D_{kk} + H_{kk})}$$

$$\theta_{ijk} = D_{ij} - \frac{2b\lambda D_{kj}D_{ik}}{1 + 2b\lambda(D_{kk} + H_{kk})}, \qquad \Sigma_i = D_{ii} - \frac{2c\lambda D_{ii}^2}{1 + 2c\lambda(D_{ii} + D_{ii})}$$